Justus-Liebig-Universität Gießen
II. Physikalisches Institut
Heinrich-Buff-Ring 16
35392 Gießen

Master Thesis

STUDY OF IMPROVED K^0_S DETECTION FOR THE BELLE II DETECTOR

Studie eines Verbesserten K^0_S Nachweises für den Belle II Detektor

by

Leonard Koch*

September 27, 2015

Supervision: Professor Dr. Wolfgang Kühn
PD Dr. Sören Lange AR

*leonard.koch@physik.uni-giessen.de

Selbstständigkeitserklärung

Hiermit versichere ich, die vorgelegte Thesis selbstständig und ohne unerlaubte fremde Hilfe und nur mit den Hilfen angefertigt zu haben, die ich in der Thesis angegeben habe. Alle Textstellen, die wörtlich oder sinngemäß aus veröffentlichten Schriften entnommen sind, und alle Angaben die auf mündlichen Auskünften beruhen, sind als solche kenntlich gemacht. Bei den von mir durchgeführten und in der Thesis erwähnten Untersuchungen habe ich die Grundsätze guter wissenschaftlicher Praxis, wie sie in der ‚Satzung der Justus-Liebig-Universität zur Sicherung guter wissenschaftlicher Praxis' niedergelegt sind, eingehalten. Gemäß § 25 Abs. 6 der Allgemeinen Bestimmungen für modularisierte Studiengänge dulde ich eine Überprüfung der Thesis mittels Anti-Plagiatssoftware.

Datum	Unterschrift

Summary

In the near future, the Belle II experiment at the SuperKEKB accelerator at KEK in Tsukuba, Japan, will start operation at a luminosity a factor 40 higher than its predecessor experiment, Belle. The physics program includes the search for physics beyond the Standard Model of particle physics by the investigation of CP violating processes and rare B meson decays. Many important decay channels involve K_S^0 mesons.

The detector features two layers of silicon pixel cells closest to the interaction point surrounded by four layers of double sided silicon strip detectors. Due to the high backgoround level, the expected occupancy of the Pixel Detector reaches up to 3 % requiring an online data reduction system: Using the four layers of strip detectors and the surrounding detectors, the online reconstructed tracks of charged particles are extrapolated to the pixelated layers, where Regions of Interest (ROIs) are defined around the intercepts. Only the pixel data inside these ROIs are stored. Thus particles creating an insufficient number of hits in the outer detectors are not reconstructed and subsequntly no regions of interest are created, resulting in the loss of the related hits in the Pixel Detector. The particles creating a sufficient number of hits in all six layers, but not in the outer four, are lost as well.

In this work, an online tracking algorithm is developed and evaluated focusing on the reconstruction of charged pions from displaced vertices, the characteristic decay topology of K_S^0 mesons. All six layers are used, in order to prevent the pixel data of the above mentioned particles to be lost. The algorithm is based on the fast Hough transform applied to the hits mapped onto the conformal plane. The amount of background is reduced by a two stage neural network filtering system.

Applied to data from a simulation of 10 000 typical Belle II events, the algorithm is adjusted to a fake rate of 90 % being considered as tolerable, resulting in a

pion reconstruction efficiency of 81.4 %. An alternative setup has a fake rate of 50 % and an efficiency of 63.6 %. The gained K^0_S reconstruction efficiencies by the additional employment of the algorithm developed in this work are 5.0 % and 1.4 %, respectively, compared to the performance of the existing track finders.

The efficiency is slightly worse for the decays $B^0 \to K^{0*}(\to K^0_S\pi^0)\gamma$ and $B^0 \to \phi K^0_S$, as carried out by an evaluation of 5000 simulated decays of each channel. However, the efficiency gain of both setups is still $\gtrsim 1$ %.

Deutsche Zusammenfassung

In naher Zukunft wird das Belle II Experiment am SuperKEKB Beschleuniger am KEK in Tsukuba, Japan, mit einer Luminosität starten, die einen Faktor 40 höher ist, als die des Vorgängerexperiments, Belle. Das Physik Programm enthält die Suche nach Physik jenseits des Standardmodells der Teilchenphysik, indem CP verletzende Prozesse und seltene B Meson Zerfälle untersucht werden. Viele wichtige Zerfallskanäle enthalten K^0_S Mesonen.

Der Detektor besitzt zwei Lagen aus Silizium Pixel-Zellen in nächster Nähe zum Wecheslwirkunspunkt, die selbst von vier Lagen aus doppelseitigen Silizium Streifen Detektoren umgeben sind. Durch den hohen Untergrund reicht die erwartete Okupanz des Pixel Detektors bis zu 3 %, was eine Echtzeit Datenreduktion benötigt: Mit dem vierlagigen Streifen Detektor und den äußeren Detektoren werden in Echtzeit die Teilchenspuren rekonstruiert, welche dann zu den Pixel Lagen extrapoliert werden, wo um die Schnittpunkte herum sogenannte Regionen von Interesse definiert werden. Nur die Pixel Daten innerhalb dieser Regionen werden gespeichert. Demzufolge werden Teilchen, die eine ungenügende Anzahl von Treffern in den äußeren Detektoren erzielen, nicht rekonstuiert, woraufhin keine Regionen von Interesse erzeugt werden und die Pixel Daten verloren gehen. Die Teilchenspuren, die zwar genügend Treffer in allen sechs Lagen zusammen erzielen, nicht jedoch in den äußeren vier, gehen ebenfalls verloren.

In dieser Arbeit wird ein Echtzeit Spurfindungsalgorithmus entwickelt und evaluiert, der auf die Rekonstruktion von geladenen Pionen von sekundären Vertices, der charakteristischen Zerfallstopologie von K^0_S Mesonen, spezialisiert ist. Es werden alle sechs Lagen benutzt, um zu verhindern, dass Pixel Daten der oben genannten Teilchen verloren gehen. Der Algorithmus basiert auf der schnellen Hough Transformation, die auf die Teilchentreffer angewendet wird, nachdem diese auf

die konforme Ebene transformiert wurden. Der Untergrund wird durch ein zweistufiges Filtersystem bestehend aus neuronalen Netzen unterdrückt.

Angewendet auf Simulationsdaten von 10 000 typischen Belle II Ereignissen wird der Algorithmus so eingestellt, dass die Rate der Untergrund Spuren 90 % ausmacht, was als akzeptabel angesehen wird. Die Effizienz der Pion rekonstruction liegt bei 81.4 %. Eine alternative Einstellung hat eine Untergrundrate von 50 % und eine Effizienz von 63.6 %. Die gewonnene Effizienz der K_S^0 Rekonstruktion durch die zusätzliche Benutzung des in dieser Arbeit entwickelten Algorithmus' liegt bei 5.0 % bzw. 1.4 % im Vergleich zu den bereits existenten Spurfindungs-Algorithmen.

Die Effizienz ist geringfügig schlechter, wenn die Zerfälle $B^0 \to K^{0*}(\to K_S^0\pi^0)\gamma$ und $B^0 \to \phi K_S^0$ betrachtet werden, wie es durch die Auswertung von jeweils 5000 simulierten Zerfällen gezeigt wird. Nichtsdestotrotz ist der Effizienzgewinn der beiden Einstellungen immer noch $\gtrsim 1$ %.

CONTENTS

List of Figures xiii

List of Tables xiv

1 *Introduction* 1

2 *Physics Background* 3
- 2.1 *The Standard Model of Particle Physics* . . . 3
  - 2.1.1 *CPT Theorem* . . . 4
  - 2.1.2 *Feynman Diagrams and the Running Coupling Constants* . . . 5
  - 2.1.3 *Quantum Chromodynamics and Quarks* . . . 6
  - 2.1.4 *Quantum Electrodynamics and Charged Leptons* . . . 8
  - 2.1.5 *The Weak Interaction and Neutrinos* . . . 8
  - 2.1.6 *The Electroweak Unification* . . . 9
  - 2.1.7 *Limits of the Standard Model* . . . 10
- 2.2 *Searching for Pysics Beyond the Standard Model - B Physics* 11
  - 2.2.1 *Highly Suppressed Decays* . . . 12
  - 2.2.2 *CP Violation* . . . 13
  - 2.2.3 *Charmonium* . . . 17

3 *The Belle II Experiment* 21
- 3.1 *The SuperKEKB Accelerator* . . . 21
- 3.2 *The Belle II Detector* . . . 23
  - 3.2.1 *The Beampipe* . . . 23
  - 3.2.2 *The Pixel Vertex Detector* . . . 24
  - 3.2.3 *The Silicon Vertex Detector* . . . 27
  - 3.2.4 *The Central Drift Chamber* . . . 28
  - 3.2.5 *Particle Identification* . . . 29
  - 3.2.6 *The Electromagnetic Calorimeter* . . . 30
  - 3.2.7 *The Superconducting Solenoid* . . . 31
  - 3.2.8 *The K_L^0 and μ Detector* . . . 31
  - 3.2.9 *Background Sources* . . . 32
  - 3.2.10 *The Level 1 Trigger* . . . 34

3.2.11 Data Acquisition and Online Data Reduction of the PXD . . . 35
3.2.12 Software . . . 36

4 Track Reconstruction 39
4.1 Interaction of Charged Particles with Matter . . . 39
4.1.1 Ionization . . . 39
4.1.2 Multiple Scattering . . . 41
4.2 Track Parameterization . . . 42
4.3 Track Finding . . . 43
4.3.1 Global Method: Hough Transform . . . 43
4.3.2 Local Method: Cellular Automaton . . . 47
4.4 Track Fitting . . . 47
4.5 A Note on Ghost Hits and Clusters . . . 47
4.6 Artificial Neural Networks . . . 48
4.6.1 The Neuron . . . 49
4.6.2 The Multi Layer Perceptron . . . 50
4.6.3 Preprocessing . . . 52
4.6.4 Hopfield Networks . . . 54
4.7 Tracking at Belle II . . . 54
4.7.1 Track Finding . . . 54
4.7.2 Track Fitting . . . 55

5 Six Layer Tracking 57
5.1 The Concept . . . 57
5.2 Simulation . . . 58
5.3 Performance Estimation . . . 60
5.4 The Six Layer Algorithm . . . 65
5.4.1 Hough Transform . . . 65
5.4.2 Reconstruction of the Z Component . . . 67
5.4.3 Background Reduction . . . 70
5.4.4 Implementation . . . 73
5.5 Optimization . . . 74
5.6 Evaluation . . . 78
5.6.1 Other Decays . . . 82
5.6.2 Further Developments . . . 82

6 Conclusion 85

A Performance of the MLPs 87
A.1 First Stage Filters – Single Hit Filter . . . 87

A.2 Second Stage Filters – Double Hit Filter 94

Bibliography ***101***

LIST OF FIGURES

2.1 Feynman Diagrams for e^-e^- scattering 6
2.2 Cross section of $e^+e^- \to$ hadrons in the bottomonium mass region 13
2.3 Feynman Diagrams for the $b \to s\bar{s}s$ transition 14
2.4 The Unitarity Triangle 15
2.5 Box diagrams describing B meson oscillation 16
2.6 Feynman diagrams for the decay $B^0 \to J/\psi K^0$ and $\overline{B}^0 \to J/\psi \overline{K}^0$ 16
2.7 Charmonium spectrum 19

3.1 Schematic View of the Belle II detector 24
3.2 CAD drawing of the PXD 25
3.3 CAD rendering of the SVD 28
3.4 Data acquisition and reduction of the PXD 37

4.1 Stopping power and the deflection angle rms of a charged pion in Silicon 40
4.2 Parameters of a helix 43
4.3 Principle of the Hough transform 44
4.4 Principle of the fast Hough transform 46
4.5 Ghost hits 49
4.6 The sigmoid function $\sigma(x) = 1/(1+e^{-x})$ 49
4.7 Structure of a Multi Layer Perceptron 51

5.1 Tracks in the $x-z$ cross section of the VXD 58
5.2 Distrubution of the decay vertices of K^0_S mesons from a simulation of 10 000 $\Upsilon(4S)$ decays 59
5.3 Transverse momentum of charged pions from a MC simulation of 10 000 $\Upsilon(4S)$ decays 63
5.4 Momentum spectrum of K^0_S mesons from a MC simulation of 10 000 $\Upsilon(4S)$ decays 64
5.5 Data flow of the six layer algorithm 66
5.6 Track candidates in the VXD – $x-y$ cross section 68

5.7 Projection of helices onto the $x-z$ plane 70
5.8 Efficiency of the six layer algorithm versus transverse momentum 77
5.9 Pion reconstruction efficiency gain by the six layer algorithm versus transverse momentum 80
5.10 Gain of the reconstuction efficiency of K_S^0 mesons by the six layer algorithm versus momentum 81

A.1 Output distribution of the first stage filters for background and $\pi^\pm$ hits 88
A.2 Background rejection versus $\pi^\pm$ hit efficiency of the first stage filters 91
A.3 Output distribution of the second stage filters for background and $\pi^\pm$ hit-reference hit combinations 95
A.4 Background rejection versus $\pi^\pm$ hit efficiency of the second stage filters 98

LIST OF TABLES

2.1 The twelve elementary fermions 4
2.2 The fundamental bosons 5

3.1 Machine parameters of the SuperKEKB accelerator 22
3.2 Dimensions and properties of the PXD 26
3.3 Specifiactions of the SVD layers 28
3.4 Properties of the three sensor types of the SVD 29

5.1 Track categories 60
5.2 Pion tracks of a MC simulation with 10 000 $\Upsilon(4S)$ decays . 61
5.3 Numbers of K_S^0 mesons from a simulation of 10 000 $\Upsilon(4S)$ decays 62
5.4 Number of hits per event in the VXD 71
5.5 Number of combinations of a hit with the reference hit per event in the VXD 72
5.6 Parameters of the two working points of the six layer tracking algorithm 76

5.7 Performance of the six layer algorithm in comparison with the existing track finders 79
5.8 Performance of the six layer algorithm for $B^0 \to K^{0*}(\to K^0_S\pi^0)\gamma$ 83
5.9 Performance of the six layer algorithm for $B^0 \to \phi K^0_S$ . . . 84

Chapter 1

INTRODUCTION

No direct experimental observation contradicts the predictions of the Standard Model of particles physics making it one of the most successfull scientific theories. However, the Standard Model is not a complete description of particle physics, because it cannot explain e.g. the matter/anti-matter asymmetry in the universe.

Already in the 1960's, Sakharov pointed out, that this imbalance requires among others CP violation [1], which reflects the change of physics observables under the symmetry operations of space inversion and exchange of particles with anti-particles. Although CP violation is incorporated into the Standard Model, its investigation offers many opportunities to search for physics beyond the Standard Model.

One possibiliy to measure the properties of CP violation is to investigate the decay of $B\overline{B}$ meson pairs at e^+e^- colliders. The Belle collaboration conducted such an experiment from 1999 to 2010 [2]. In 2018, its upgrade, the Belle II experiment, will start operation [3]. It features a new DEPFET Pixel Vertex Detector only 1.4 cm remote from the interaction point for the improvement of the vertex determination, which is crucial for the measurement of CP violation. The upgraded accelerator SuperKEKB will increase the luminosity by a factor of 40 compared to its predecessor holding the current world record. This will enable Belle II to collect 40×10^9 $B\overline{B}$ pairs. However, the detector (in particular the inner detectors) will be exposed to a factor of ≈ 10 increased background level.

As a result, the Pixel Vertex Detector will feature a data output rate of $\gtrsim 20\,\mathrm{GB/s}$ being more than ten times the data rate of all other subdetectors combined and mostly constisting of background [4]. In order to store only relevant physics data, an online reduction system selects only pixel data inside regions of interest. The regions of interest are determined by the extrapolation of online reconstructed particle tracks from the outer detectors into the Pixel Vertex Detector. This bears the risk of losing the pixel data from particles, that create an insufficient number of hits in the outer layers for tracking.

As evaluated in [5], the detection of charged pions from K^0_S decays is affected by this issue. Having a lifetime of 2.68 cm/c [6], K^0_S mesons can travel a certain distance, before they decay. Usually they are reconstructed via the decay into $\pi^+\pi^-$ pairs originating from a secondary vertex. This topology enables the tracks not to be found by the track finders, that are used to determine the regions of interest.

Since the experimental observation of CP violation [7], the K^0_S meson has played a major role in the measurements of CP violation. For example the "golden" decay $B^0 \to J/\psi K^0_S$ [8] and the decay $B^0 \to \phi K^0_S$ involve this meson. It is also important for other measurements, that are sensitive to physics beyond the Standard Model, for example in the decays $B^0 \to K^{0*}(\to K^0_S\pi^0)\gamma$ and $B \to K^*(\to K^0_S\pi)\ell^+\ell^-$.

In this work, an online track finding algorithm using the hits from the Pixel Vertex Detector and its surrounding Silicon Vertex Detector is developed and evaluated focusing on the identification of charged particle tracks from secondary vertices.

The next chapter provides an overview of the Standard Model of particle physics and physics involving B meson decays. The components of the Belle II detector together with the online data reduction system are described in Chapter 3. Chapter 4 presents an introduction to track reconstruction methods with special emphasis on the Hough transform and the Multi Layer Perceptron as an option to reduce the amount of background hits. The algorithm developed in this work is explained and its performance is evaluated in Chapter 5. Chapter 6 concludes this work.

Chapter 2

PHYSICS BACKGROUND

2.1 The Standard Model of Particle Physics

Modern physics is able to describe all observed forces in nature by four fundamental interactions: The electrogmagnetic, the weak, and the strong interaction, as well as gravitation. While the latter is represented by general relativity [9], the first three interactions are combined in the Standard Model of Particle Physics (SM).

The SM is a relativistic Quantum Field Theory (QFT), i.e. particles are represented by field operators. The equations of motion are obtained by applying the Euler-Lagrange formalism to a Lagrangian density. Furthermore, one requires the SM to be invariant under certain local gauge transformations, thus the SM is also a gauge field theory. The symmetry group of the SM Lagrangian can be written as [10]

$$G = SU(3)_C \otimes SU(2)_L \otimes U(1)_Y \quad . \tag{2.1}$$

In the SM, there are two types of elementary particles. The building blocks of ordinary matter are the (elementary) fermions (see Table 2.1). They have half integer spin ($1/2\hbar$). The forces between the fermions are transmitted by the gauge bosons, that have a spin of $1\hbar$ (see Table 2.2). The fermions can be divided into quarks and leptons. Each of them are arranged in three generations. Every quark generation contains an "up-type" quark with an electric charge of $+2/3\,e$ and a "down-type" quark with $-1/3\,e$. A lepton generation (also: family) consists of a lepton with an electric charge of $-1\,e$ and an uncharged lepton. Any gauge boson can be assigned to one of the three interactions. They couple only to particles, that carry the charge corresponding to the interaction. The strong interaction is mediated by eight different gluons. The gluons (g) couple to color, the charge of the strong interaction, which is carried by quarks. The weak interaction couples to the weak isospin, that is carried by all left-handed fermions. Its gauge bosons are the Z^0 and the electrically charged $W^{\pm}$ bosons. The electromagnetic interaction is trans-

Table 2.1: The twelve elementary fermions with its charges, according to [10, 11]. C stands for color, Q is the electric charge, and $T_{3,L}$ is the third component of the weak isospin of the left-handed component of the fermion. Right-handed fermions have a weak isospin of 0. $Y_{L/R}$ is the weak hypercharge of the left/right-handed component of the fermion. The d, s, and b quarks are not eigenstates of the weak isospin operator, so the shown values are valid for the mixed d′, s′, and b′ quarks (see Section 2.1.5).

	Generation			Charge				
	I	II	III	C	Q	$T_{3,L}$	Y_L	Y_R
Quarks	u	c	t	r,g,b	$+2/3\,e$	$-1/2$	$1/3$	$+4/3$
	d	s	b	r,g,b	$-1/3\,e$	$+1/2$	$1/3$	$-2/3$
Leptons	e^-	μ^-	τ^-		$-1\,e$	$-1/2$	-1	-2
	ν_e	ν_μ	ν_τ			$+1/2$	-1	

mitted by the photon (γ), which couples to the electric charge. Additionally, there is one scalar (spin $= 0$) boson, the Higgs boson (H^0). It is the manifestation of a non-zero vacuum expectation value of the Higgs field, due to electroweak symmetry breaking. In this process, the coupling of the Higgs field to the elementary particles generate their mass [10].

Every particle has an antiparticle. By replacing a particle by its antiparticle, every charge changes its sign, while other quantites like mass and spin stay the same. For example, the positron is the antiparticle of the electron and thus has the opposite charge ($e^- \leftrightarrow e^+$). Another example is the anti-up quark ($u \leftrightarrow \overline{u}$). The charge is now $-2/3\,e$, but it also carries an anti-color.

2.1.1 CPT *Theorem*

There are many transformations, that can be applied to a physical system. Translations and rotations in space-time are well known. A different kind of transformations are the discrete transformations. They do not depend on a paramter like the distance a system is shifted by a translation. The fundamental discrete transformations are described by the $\hat{C}$, $\hat{P}$, and $\hat{T}$ operators [12].

$\hat{C}$ is the charge conjugation operator. It replaces every particle by its anti-particle. Some particles like the photon are their own anti-particles, so they are eigenstates of the $\hat{C}$ operator. The eigenvalue

Table 2.2: The fundamental bosons, according to [6]. J is the spin in units of $\hbar$, P is the parity, and C is the charge conjugation (see Section 2.1.1). The weak gauge bosons are neither an eigenstate of the parity nor of the charge conjugation operator, so no P and C can be assigned. This holds truth for the charge conjugation of the gluon g. The SM Higgs boson has $PC = ++$, which is experimentally yet undetermined. The non-zero masses correspond to experimental measurements. Although the SM masses of the gluon and the photon are zero, a gluon mass of a few MeV/c^2 cannot be excluded by experiment. For the photon an upper limit of 1×10^{-18} eV/c^2 can be stated.

Boson	Interaction	J^{PC}	Takes Part in	Mass [GeV/c^2]
g	strong	1^{-}	strong	0
γ	em	1^{--}		0
$W^{\pm}$	weak	1	em, weak	80.385 ± 0.015
Z^0	weak	1	weak	91.1876 ± 0.0021
H^0		0		125.7 ± 0.4

is then denoted by C and can be $+1$ or -1, often abreviated as $+$ or $-$. The parity operator $\hat{P}$ changes the sign of the x, y, and z coordinate. The eigenvalues P under the $\hat{P}$ transformation are again $+$, and $-$. It is worth noting, that the helicity of a particle changes sign under $\hat{P}$. So a left-handed particle will become right-handed. The sign change of the time coordinate is obtained by applying the time reversal operator $\hat{T}$.

Every locally gauge invariant QFT (and so the SM) is invariant under the subsequently application of all three $\hat{C}$, $\hat{P}$, and $\hat{T}$ operators in arbitrary order. This invariance is called "CPT Theorem". Observing CPT violation would immediatly imply physics beyond the SM in a very fundamental way. It would mean, that already the ansatz of a gauge invariant QFT is wrong. So far, no such violations have been observed.

2.1.2 *Feynman Diagrams and the Running Coupling Constants*

Various calculations in a QFT require the knowledge of the (interacting) propagator of the particles. Due to the non-linearity of an

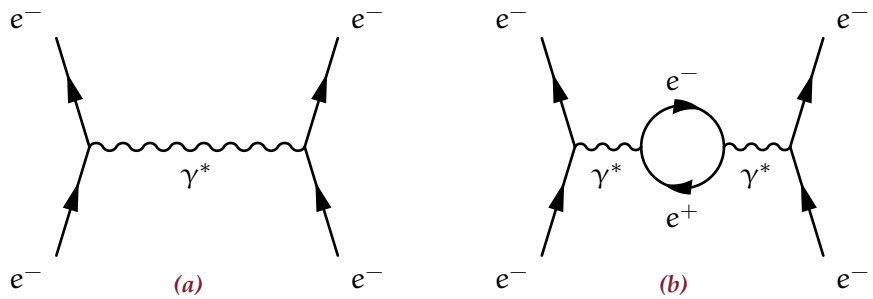

Figure 2.1: Feynman Diagrams for e^-e^- scattering, according to [10]. ***(a)*** Lowest order diagram (tree level), photon exchange. ***(b)*** Higher order loop diagram. This diagrams represents the lowest order vacuum polarization.

interacting Lagrangian, analytical solutions for the propagators are not available. Nevertheless, it is often possible to expand the propagator into a power series in terms of the coupling constant. For a small coupling constant this perturbative expansion converges to the true propagator. Since the higher order corrections contribute little to the result, one can negelect the terms above a chosen order and obtain an approximation with the desired accuracy.

A visual representation of the terms in the expansion are the Feynman Diagrams (see Figure 2.1). For every QFT a set of Feynman Rules prescribe how to translate such a diagram into a mathematical expression of the propagator. Each line in the diagram stands for the free propagator (for which an analytical solution exists) of a particle and the vertices, where the lines meet, represent the coupling of the particles. Every vertex introduces the coupling constant as a factor. Therefore, the number of vertices reflects the order of the correction term. Every closed loop in a diagram causes an infinite integral (see Figure 2.1(b)). However, these infinities can be renormalized, such that the mathematical result stays finite and physical. This renormalization leads also to a renormalization of the coupling constant, which now depends on the momentum transfer. It is no longer a constant, but a "running coupling constant" [10, 13].

2.1.3 *Quantum Chromodynamics and Quarks*

The strong interaction is parameterized by Quantum Chromodynamics (QCD) [6, 10]. It is a QFT based on the non-abelian $SU(3)$

color symmetry. There are three colors: red, green, and blue (r, g, and b). The anti-colors are anti-red, anti-green, and anti-blue ($\overline{r}$, $\overline{g}$, and $\overline{b}$). The six quark flavors are the up, down, strange, charm, bottom (also: beauty), and top (also: truth) quarks (u, d, s, c, b, and t).

The fact that QCD is a non-abelian gauge field theory gives rise to the self-interaction of the gluons. While coupling to colored particles, the gluons itself carry color. To be more precise, a gluon carries simulataniously a color and a different anti-color. This is also the reason, why there are eight gluons. According to $3 \otimes \overline{3} = 8 \oplus 1$, the color triplet couples with the anti-color triplet to a colored octett and a colorless singlet. The singlet is not able to change the color of a particle, hence it does not exist in nature [10].

In nature, there are no free quarks. They are only observed bound into compound states, the hadrons. Hadrons are color singlets, i.e. they are colorless. This is realized by the rule, that the combination of r, g, and b equals "white" $\equiv$ color-neutral, as well as a combination of a color with the same anti-color. The class of hadrons is further divided into baryons and mesons. Baryons are composed of three quarks. An internal quantum number of hadrons is the baryon number. It is $+1$ for baryons and -1 for anti-baryons. In all processes of the SM the baryon number is conserved. Mesons contain a quark and an anti-quark and thus have a baryon number of 0. Although the requirement for being color-neutral allows a wide spectrum of possible hadrons, only baryons with three quarks and mesons with a quark and an anti-quark have been observed. The most prominent examples are the proton ($|uud\rangle$) and the neutron ($|udd\rangle$), which are the constituents of nuclei. Also the observed mesons contain only a quark and an antiquark. Very recently the LHCb collaboration published an article, in wich they claim to observe a pentaquark state ($|qqqq\overline{q}\rangle$, where q stands for any quark flavor) [14]. A few years ago, many mesons were discovered, that seem not to fit into the pattern of conventional $|q\overline{q}\rangle$ states. To explain these states, models like tetraquarks or meson molecules are under consideration, more in Section 2.2.3.

The fact that the quarks are bound into colorless objects is called "confinement". At very high momentum transfers, the quarks are moving almost freely. This is called the "asymptotic freedom" of QCD. The running coupling constant is well suited to describe both of these phenomena. On the one hand, the self interaction of the

gluons result in a very large coupling constant at small momentum transfers (large distances, confinement). On the other hand, it vanishes at large momentum transfers (small distances, asymptotic freedom). However, the large coupling constant at small distances does not allow a perturbative treatment of the theory, since the expansion of the propagator no longer converges (c.f. Section 2.1.2). Therefore, it is very difficult to make reliable predictions in the non-perturbative regime of QCD and the true nature of confinement is still not understood [10].

2.1.4 *Quantum Electrodynamics and Charged Leptons*

The electromagnetic interaction is described by Quantum Electrodynamics (QED) having a $U(1)$ symmetry [10, 13]. The gauge boson of QED is the massless photon (γ) coupling to the electric charge. Thus, all quarks and charged leptons (e^-, μ^-, and τ^-) as well as the charged (but very unstable, see Section 2.1.5) $W^\pm$ bosons are interacting via QED.

In contrast to QCD, the electromagnetic coupling constant decreases as the momentum transfer gets smaller. However, the coupling is sufficient low at all momentum transfers to solve the equations of QED perturbatively. So far, no contradiction between the theoretical framework of QED and experimental measurements have been found, making QED the most precisely tested scientific theory.

2.1.5 *The Weak Interaction and Neutrinos*

The weak interaction affecting all fermions has the non-abelian gauge symmetry group $SU(2)$. Therefore, it is the only way, that the neutrinos (ν_e, ν_μ, and ν_τ) interact (exept for gravitation). It is mediated by the massive gauge bosons Z^0 and $W^\pm$, that also couple to themselves. The fact that they are massive makes the weak interaction very short-ranged.

The neutral current (mediated by the Z^0) is very similar to the electromagnetic interaction with a photon, but the charged current interactions (involving $W^\pm$) are able to change the flavor of a particle. It can turn a muon into a muon-neutrino. This takes into account the law of lepton family number conservation. Every lepton of a family f gets the additive lepton family number of $L_f = +1$ and the anti-leptons of a family get $L_f = -1$, such that in all SM

reactions all three L_e, L_μ, and L_τ are conserved. But also quarks can change their flavor via charged current interactions. Accordingly a b quark can change into a c quark. Due to the charge of the $W^\pm$ boson the charge of the quark needs to change, too. The $W^\pm$ couples to the up-type flavors with the same strength , but the coupling to the down-type flavors is non-universal. However, they couple to the d', s', and b' states with the same strenght as to the up-type flavors. These states are obtained by a rotation in flavor space:

$$\begin{pmatrix} |d'\rangle \\ |s'\rangle \\ |b'\rangle \end{pmatrix} = \begin{pmatrix} V_{ud} & V_{us} & V_{ub} \\ V_{cd} & V_{cs} & V_{cb} \\ V_{td} & V_{ts} & V_{tb} \end{pmatrix} \begin{pmatrix} |d\rangle \\ |s\rangle \\ |b\rangle \end{pmatrix} \quad . \tag{2.2}$$

The SM requires this mixing matrix, the Cabibbo-Kobayashi-Maskawa (CKM) matrix, to be unitary, leaving only four physical degrees of freedom [15]. It can be parameterized by three angles and one imaginary phase.

The charged current is maximally parity and charge conjugation violating: Only left handed fermions and right-handed anti-fermions couple to the $W^\pm$ bosons. It was long believed, that physics is invariant under the combination of these operations. However, the weak interaction violates CP invariance. This is described by the non-zero phase of the CKM matrix [10].

It is very difficult to measure the masses of the neutrinos. Thus, only upper limits exist ($< 2\,\mathrm{eV}$ for $\overline{\nu}_e$) [6]. The hypothesis of massless neutrinos is disproven by the observation of neutrino oscillation. This requires their masses to be distinct from each other. Consequently at least two neutrinos must have a non-vanishing mass.

In addition, it is still not clear, wether the neutrino is a Dirac fermion (like all other fermions) or a Majorana fermion. Particles of the latter kind are their own anti-particles [10].

2.1.6 *The Electroweak Unification*

It is possible to describe the electromagnetic and the weak interaction in a single theory of the electroweak interaction having a $SU(2) \otimes U(1)$ symmetry [10, 12]. Therefore the concept of the weak isospin T and the weak hypercharge Y is introduced (see Table 2.1). All left-handed fermions are arranged in isospin 1/2 doublets according to the lepton families and quark generations. A weak

isospin of zero is asigned to the right-handed fermions, they build singlets. The weak hypercharge fulfills the relation

$$Q = \frac{1}{2}Y + T_3 \quad , \tag{2.3}$$

with Q being the electric charge in units of e and T_3 the third component of the weak isospin. The gauge bosons are then grouped into an isotriplet W^k, $k = 1, 2, 3$ and a singlet B^0. The physical bosons are obtained by the following transformations, ϑ_W being the "Weinberg angle":

$$|W^+\rangle = \frac{1}{\sqrt{2}}\left(|W^1\rangle - i|W^2\rangle\right) \quad , \tag{2.4}$$

$$|W^-\rangle = \frac{1}{\sqrt{2}}\left(|W^1\rangle + i|W^2\rangle\right) \quad , \text{ and} \tag{2.5}$$

$$\begin{pmatrix} |Z^0\rangle \\ |\gamma\rangle \end{pmatrix} = \begin{pmatrix} \cos\vartheta_W & -\sin\vartheta_W \\ \sin\vartheta_W & \cos\vartheta_W \end{pmatrix} \begin{pmatrix} |W^3\rangle \\ |B^0\rangle \end{pmatrix} \quad . \tag{2.6}$$

One problem of the weak interaction is the fact, that the $W^\pm$ and Z^0 bosons are massive. To be locally gauge invariant, a theory needs to have massless gauge bosons. This can be fixed by introducing the scalar Higgs field. This Higgs field couples to the massless bosons giving them mass by spontanious symmetry breaking. The photon stays massless during this process. The mass terms of the fermions in the SM Lagrangian can also be expressed as a coupling of the fermions to the Higgs field. Accordingly, the coupling strengths are proportional to their masses. A non-zero vacuum expectation value of the Higgs field leads to a massive Higgs boson [10].

2.1.7 *Limits of the Standard Model*

The SM is a very powerfull theory describing the whole field of particle physics. There are no contradictions to experimental observations. However, it is clear, that the SM cannot explain everything:

- The SM does not contain gravitation.
- There is a matter/anti-matter asymmetry in the universe. Assuming the Big-Bang Theory, there was an equal amount of matter and anti-matter created at the beginning of the universe. In order to explain the asymmetry, there need to be

baryon number violating processes, which are not included in the SM [1].

- From the rotation velocity of galaxies, the effect of gravitational lensing, and the accelerating expansion of the universe it is known, that only 5 % of the total amount of energy/mass in the universe is made from visible matter (i.e. the particles included in the SM). So the SM described only 5 % of the universe [11].

Additionally, the SM is not "elegant" in terms of having at least 18 parameters, that cannot be predicted by theory, but need to be determined by experiment [10]. It might be possible, that the $SU(3)$, $SU(2)$, and the $U(1)$ symmetry are part of a more general gauge symmetry. The simplest such symmetry group is $SU(5)$.

When extrapolating the three running coupling constants of the SM to very high momentum transfers, they almost meet at an energy scale of $\approx 10^{15}$ GeV [12]. The theory of Supersymmetry (SUSY) changes the couplings such, that they will meet exactly. So one could think of only one unifying interaction at very high energies with a spontaniously broken symmetry at lower energies. Therefore, every fundamental particle gets a supersymmetric particle with a spin differing by $1/2\hbar$. The masses of these particles needs to be very high, since no such particles have been found so far.

There are also attempts to combine the SM with gravitation. The most famous is the string theory, where all particles are described as excitations of very small (in the order of the Planck length $\approx 10^{-35}$ m) strings [11]. This only works, if the space-time has at least ten dimensions. In addition, string theory predicts magnetic monopoles. In experimental searches there is no evidence for extra dimensaions as well as for magnetic monopoles.

2.2 *Searching for Pysics Beyond the Standard Model – B Physics*

There are two frontiers in high-energy physics being steadily pushed forward in order to search for physics beyond the SM. The first one is the energy frontier. By increasing the center of mass energy, new particles might get produced, that can be detected via its decay products. In this way, the Higgs boson was detected by Atlas and CMS

at the LHC, the two main experiments working at the energy frontier [16, 17].

A different working point is the precision frontier. Here the experiments accumulate very large statistics, in order to search for physics beyond the SM by making high precision tests of the SM predictions and the investigation of very rare processes. B physics, i.e. physics involving B meson decays, are settled at the precision frontier, because B mesons can be produced in huge amounts at the B factories. The two e^+e^- colliding B factories were KEKB at KEK in Japan and PEP-II at SLAC in the US providing the experiments Belle and BaBar [3, 18]. They were running at a center of mass energy of 10.58 GeV according to the mass of the $\Upsilon(4S)$ resonance (c.f. Figure 2.2). This is the first bottomonium state above the open bottom threshold. Hence, it dominantly decays into a $B\overline{B}$ pair. Although the LHC is definetly an energy frontier pp collider, it also produces a lot of B mesons that are detected at LHCb, a hadronic B factory. The future SuperKEKB will be a next generation e^+e^- Super B factory, at which Belle II will be operating [3, 19].

2.2.1 *Highly Suppressed Decays*

The huge amount of B mesons produced at the B factories allows the investigation of highly suppressed and therefore very rare decays. A famous example are the flavor changing neutral currents (FCNCs). In the SM there is no gauge boson mediating such processes. They can only occur via higher order diagrams, which makes them rare, but enables physics beyond the SM to enter at the same level (c.f. Figure 2.3). Thus, the exploration of FCNCs is well suited for testing the SM and constraining new physics scenarios. The theoretical predictions for most observables in these processes are affected by large uncertainties inherited from non-perturbative QCD. Accordingly, one often investigates CP asymmetries in these decays (c.f. next Section), because here the uncertainties mostly cancel.

Measuring the decay $B^0 \to \phi K^0_S$, which is based on the transition $b \to s\bar{s}s$ (c.f. Figure 2.3), gives acces to the UT angle β (c.f. next section). Extensions of the SM allow the measured angle in this decay to differ from the value obtained by the tree dominated decay $B^0 \to J/\psi K^0_S$ [21]. Another FCNC is the $b \to s\gamma$ transition, which is additionally supressed by means of helicity. As a consequence, this process is sensitive to right-handed currents [22, 23]. A promising

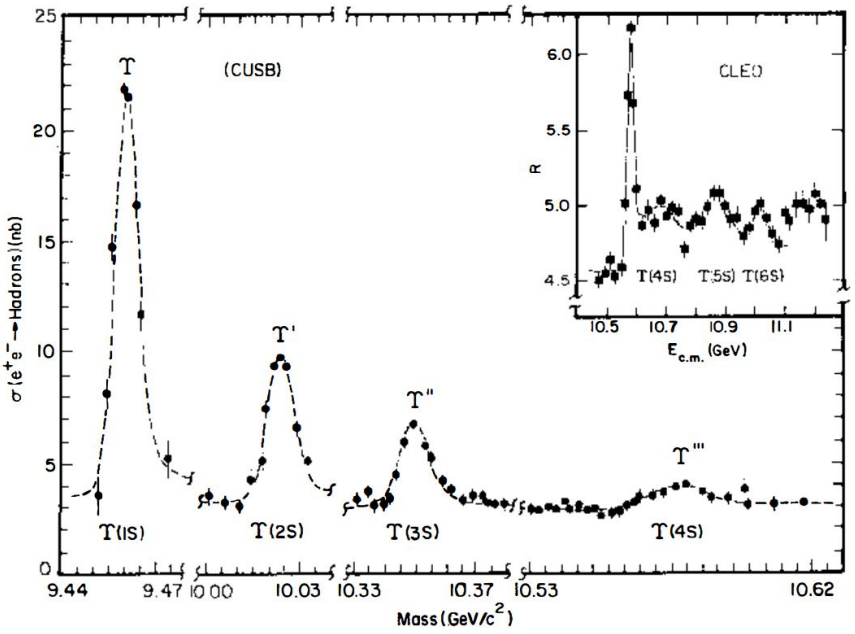

Figure 2.2: Cross section of $e^+e^- \to$ hadrons in the bottomonium mass region, taken from [20]. The $\Upsilon(4S)$ is the first resonance above the open bottom threshold.

channel is $B^0 \to K^0_S\pi^0\gamma$. Other rare but sensitive decays are $B^+ \to \tau^+\nu_\tau$ [24], $B \to K\pi$ [25], $B \to K^{(*)}\ell^+\ell^-$ [26, 27], $B_{(S)} \to \ell^+\ell^-$ [28], and many more. So far, the statistics of the past B factories is not sufficient to make significant statements, which makes LHCb and Belle II unique experiments at the precision frontier.

2.2.2 CP *Violation*

The main motivation for the construction of the B factories is the measurement of CP violation [2, 3, 18, 30]. There are three types of CP violation:

1. The probability, that an initial state i decays into the final state f is inequal to the probability of the CP conjugate process: $\Gamma(i \to f) \neq \Gamma\left(\bar{i} \to \bar{f}\right)$ is called "CP violation in decay".

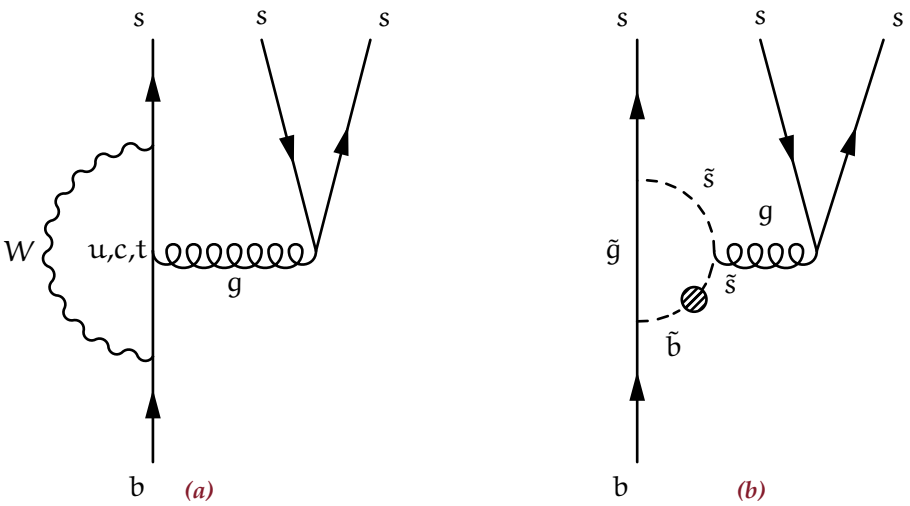

Figure 2.3: Feynman Diagrams for the $b \to s\bar{s}s$ transition, according to [3, 29]. ***(a)*** The SM contribution. ***(b)*** The SUSY gluino-down squark contribution. The dot represents a mass insertion.

2. For a neutral mesons M^0 that can oscillate into their antiparticle (c.f. Figure 2.5), one can observe the "CP violation in mixing": $\Gamma\left(M^0 \to \overline{M}^0\right) \neq \Gamma\left(\overline{M}^0 \to M^0\right)$.

3. For neutral mesons that have a common final state with its antiparticle, the first two kinds of CP violation can interfere (c.f. Figure 2.6), which gives "CP violation in interference". While CP vioaltion in decay and CP violation in mixing are considered to be small effects, a constructive interference of them can result in asymmetries, that are easier to measure.

Since CP violation is described by the imaginary phase of the CKM matrix (Equation (2.2)), investigation of CP violation is performed by measuring the elements of the CKM matrix and the relations among them. From the unitarity of the CKM matrix it follows, that $VV^\dagger = V^\dagger V = \mathbb{1}$, giving 12 equations, that relate the elements to each other:

$$\sum_{i=u,c,t} V_{ij} V_{ik}^* = \sum_{i=d,s,b} V_{ji} V_{ki}^* = \delta_{jk} \quad . \tag{2.7}$$

Taking $j = d$ and $k = b$, it reads

$$V_{ud} V_{ub}^* + V_{cd} V_{cb}^* + V_{td} V_{db}^* = 0 \quad , \tag{2.8}$$

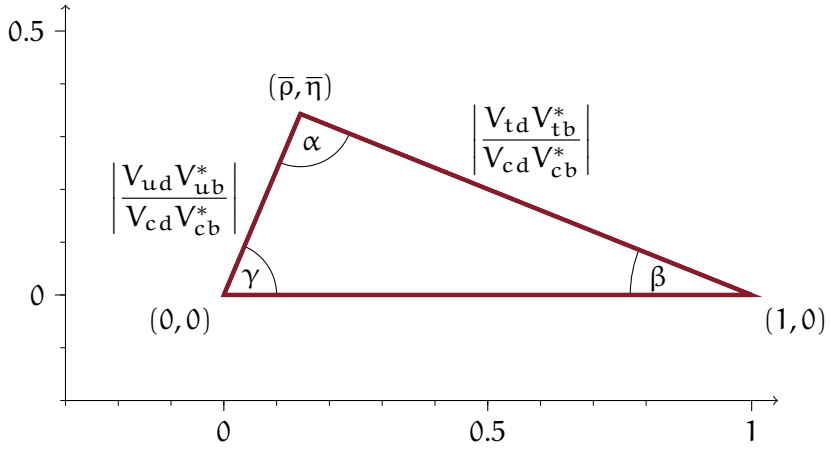

Figure 2.4: The Unitarity Triangle. $\overline{\rho}$ and $\overline{\eta}$ are Wolfenstein parameters, a different parameterization of the CKM matrix [31]. It holds $\overline{\rho}+i\overline{\eta} = -V_{ud}V_{ub}^*/V_{cd}V_{cb}^*$, according to [32].

which can be represented by a triangle in the complex plane. By dividing this equation by the second summand, one obtaines a normalized triangle, which is refered to as the Unitarity Triangle (UT), c.f. Figure 2.4. The area of the triangle is a measure for the strength of CP violation. In the absence of CP violation it would be zero. Measuring the angles and sides of the UT is a powerfull tool for testing the SM [6].

A lot of these quantities can be determined from measuring time-dependent asymmetries in B decays, that arise from the CP violation in interference. The angle β can be determined very well from the analysis of $B^0 \to J/\psi K_S^0$ and $B^0 \to J/\psi K_L^0$, c.f. Figure 2.6 [8]. The investigation of the decays $B^0 \to \pi^+\pi^-$ and $B^0 \to \rho^+\rho^-$ provide access to α [33]. The angle γ can be measured in the decays $B \to D^{(*)}K$ [34].

In order to detect an asymmetry between the B^0 and the $\overline{B}^0$ meson decay, the knowledge of the flavor of the decaying meson is required. In a decay into a final state being common to both, this is a non-trivial task. Nontheless, the flavor can be tagged indirectly. When the B mesons are produced as a coherent pair, the flavor of one meson is opposite to the flavor of the other (two independent B mesons could oscillate independently and this relation no longer holds), that can be tagged by the decay products of the meson. The

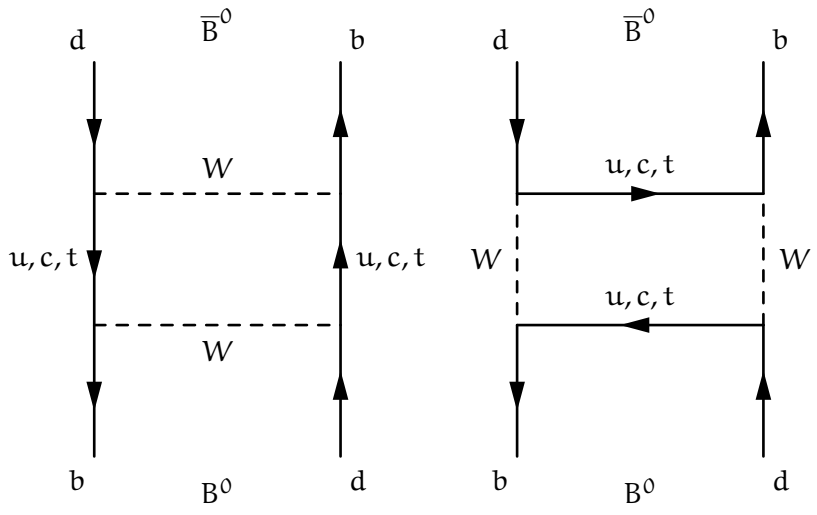

Figure 2.5: Box diagrams describing B meson oscillation via double W exchange.

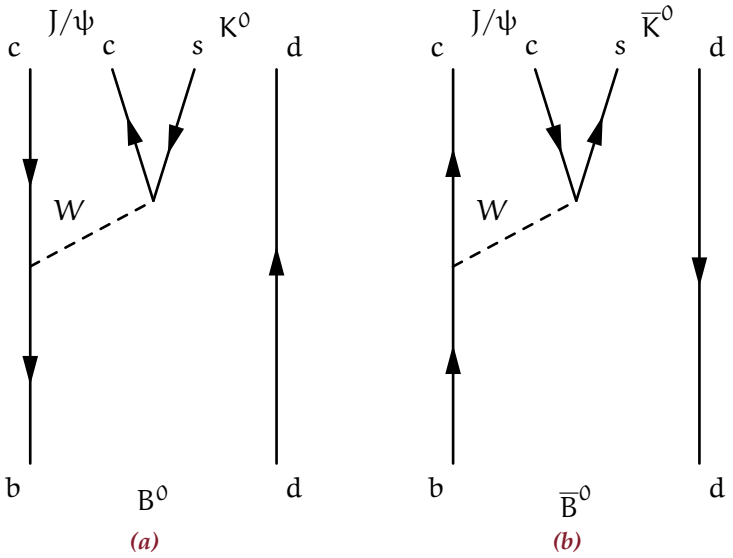

Figure 2.6: Feynman diagrams for the decay $B^0 \to J/\psi K^0$ *(a)* and $\overline{B}^0 \to J/\psi \overline{K}^0$ *(b)*. The kaons are either observed as a K^0_S or K^0_L meson. Due to the B meson oscillation (c.f. Figure 2.5), these two channels can interfere.

e^+e^- B factories adjust the center of mass energy to the $\Upsilon(4S)$ resonance (c.f. Figure 2.2), which dominantly decays into coherent $B\overline{B}$ pairs. LHCb can also select $B\overline{B}$ pairs, that are coherent. The flavor tagging needs a high efficiency particle identification, that is provided by the detectors.

The time differences, that need to be detected are in the order of $\approx 5\,\mathrm{ps}$, which is feasable to be measured directly. Therefore, the rest frame of the center of mass is boosted with respect to the laboratory frame. This is achieved by the asymmetric beam energies of the e^+e^- colliders. The LHCb detector is placed in the forward direction of the symmetric pp collision, where the high rapidity naturally gives a boost to the $B\overline{B}$ system. Compared to its mass of $5.28\,\mathrm{GeV}/c^2$, the B^0 meson as rather low momentum of $\approx 330\,\mathrm{MeV}/c$ in the $\Upsilon(4S)$ rest frame, that moves along the z axis. Consequently, the decay time difference of the B mesons can be determined via $\Delta t = \Delta z/\beta\gamma c$, where Δz is the difference of the z components of the decay vertices. With an appropriate boost, the required resolution of the z vertex reconstruction is in the order of $\approx 100\,\mu\mathrm{m}$, which can be achieved by modern pixelated or striped silicon detectors.

2.2.3 *Charmonium*

Due to the mass hirachy of the quarks and the almost diagonal structure of the CKM matrix, the b quark in the B meson dominantly decays into a c quark by the emission of a virtual $W^\pm$ boson, which then creates a quark and an antiquark (with different flavor). Often, one of these new quarks is a $\overline{c}$ quark, so the resulting $c\overline{c}$ pair can be bound into a hadron, which is called charmonium.

Charmonia are mesons composed of a charm and an anti-charm quark in the mass region of $3-4.5\,\mathrm{GeV}/c^2$. A perturbative treatment of QCD in this regime is not possible, to predict the masses of these states, so one has to rely on Lattic QCD calculations, effective field theories and non-relitivstic models [35–37].

The latter approach assumes, that the charm quarks ($m \approx 1.3\,\mathrm{GeV}/c^2$) are moving slowly inside the meson, so that non-relativistic quantum mechanics can be applied. Therefore, a semi-empirical potential

$$V^{(c\overline{c})}(r) = -\frac{4}{3}\frac{\alpha_s}{r} + br \quad , \tag{2.9}$$

that is refered to as the Cornell Potential, is derived [37]. It consists of a Coulomb term with the coupling α_s and a confinement term propotional to r with b called "string constant". Additional terms can be added, taking into account the spin-spin, spin-orbit, and tensor forces [38]. In total, this potential has four parameters (including the charm quark mass), that need to be determined from experimental observations. Using eleven known charmonium masses as input, Reference [38] solves the non-relativistic Schrödinger equation and predicts the masses of yet not observed charminium states. Figure 2.7 shows the predicted and the observed states. One can see, that the calculated and the observed masses below the open charm threshold agree with very high accuracy.

While not all predicted states have yet been found, unpredicted states are observed (c.f. Figure 2.7). They are referd to as exotic charmonium states, since they do not fit into the pattern of conventional charmonium. For example the $X(3872)$, which was first discovered in the decay $B^{\pm} \to X(3872)K^{\pm}$ [44], lies above the open charm threshold, but has a very small width ($\Gamma < 1.2\,\text{MeV}$ [6]), which is rather untypical for conventional charmonia. Other states have been observed, that are charged, which automatically discards the pure $c\bar{c}$ hypothesis [45–47]. The charged states are named Z_C with its mass in parentheses. There have also neutral states been found with a mass very close to a charged state. They are assumed to form an isospin multiplet, hence they are also called Z_C. All exotic vector states are refered to as Y states and the other exotics are called X. The PDG has a different naming scheme, calling them all X.

If they are no conventional $c\bar{c}$ states, they need to be something else. In order to form a narrow charged state in the charmonia mass region, the Z states need to contain at least four constituent quarks. There are models, describing the XYZ states as compact tetraquarks [48], losely bound meson molecules [49], or hybrids being made from a quark anti-quark pair and an excited gluon [50]. Other models try to describe them as hadro-charmonium, a $c\bar{c}$ meson surrounded by a cloud of light mesons [51], and some say, these states are no real resonances but perturbative rescattering effects at thresholds [52]. The true nature of these states is very unclear and studying them will help to understand non-perturbative QCD und confinement.

In the bottom sector, there is the spectrum of bottomonium states. They can be described as well by a Cornell Potential and

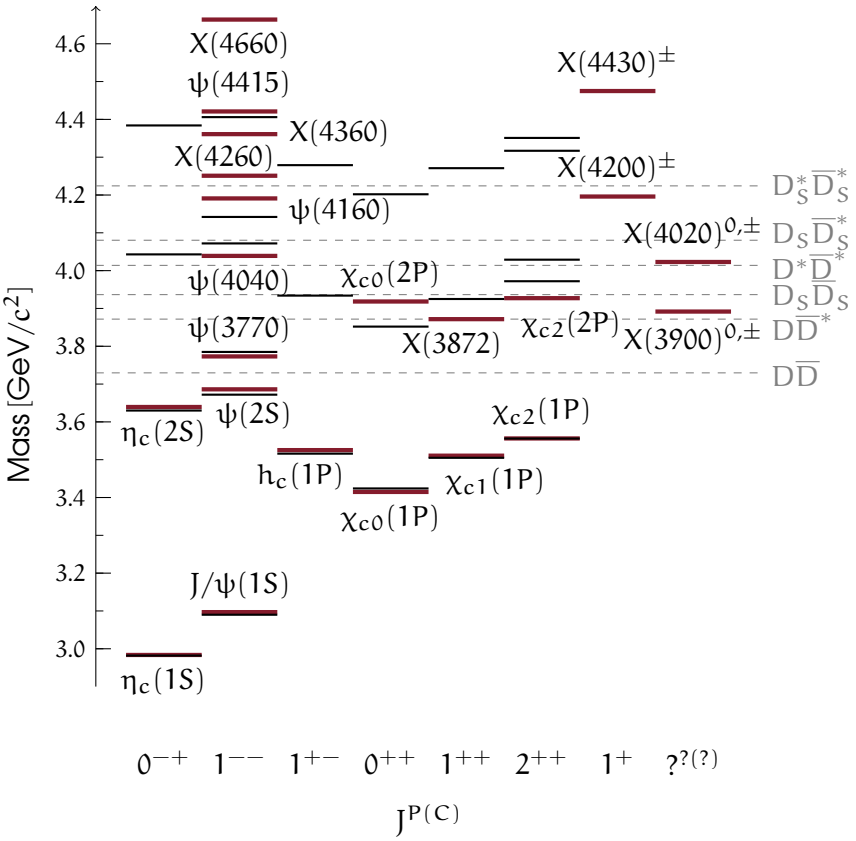

Figure 2.7: Charmonium spectrum ordered by the quantum numbers J^{PC}. The black lines represent theoretical predictions [38] and the red lines together with the names of the states stand for the experimental observations. Additionally, the most important thresholds for open charm decays are shown. Exotic states are named X with its mass in MeV/c^2 according to the PDG naming convention [6]. The masses of the predictions are taken from [38], while the experimental values are taken from [6, 39–43].

exotic states are also observed [53, 54]. At the e^+e^- B factories, the B mesons are dominantly produced in the decay of the bottomonium state $\Upsilon(4S)$, so either by varying the center-of-mass energy or via the decay of $\Upsilon(4S)$ to other bottomonium states bottomonium spectroscopy can be done at the B factories. Toponium does not exist, because the very heavy top quark decays, before it can form a bound $t\bar{t}$ state.

Chapter 3

THE BELLE II EXPERIMENT

The future Belle II experiment [3] is the upgrade of the Belle experiment [2] and will start data taking in 2018. Belle operated from 1999 until 2010 at the asynchronous e^+e^- collider KEKB at KEK (High Energy Accelerator Research Organization) in Tsukuba, $\approx$ 60 km north of Tokyo, Japan. With $\sqrt{s} = 10.58\,\text{GeV}$ it ran at the $\Upsilon(4S)$ resonance, which decays dominantly into a pair of B-mesons, hence it is called a B-factory. Belle also recorded data at the $\Upsilon(1S)$, $\Upsilon(2S)$, $\Upsilon(3S)$, and $\Upsilon(5S)$ with an overall integrated luminosity of $1\,\text{ab}^{-1}$. Together with its companion experiment Barbar at SLAC [18] in Stanford, US, Belle measured for the first time CP-violation outside the Kaon system and determined the angles of the unitarity triangle with high precision [55]. This experimental confirmation of the CKM-mechanism led to the awarding of the Nobel Prize to M. Kobayashi and T. Maskawa in 2008 [56]. Additionally, Belle discovered and confirmed the discovery by other experiments of exotic quarkonium-like states (e.g. the $X(3872)$, and the $Z_C(3900)^{\pm}$), that do not fit into the pattern of conventional quarkonium and therefore probe non-perturbative QCD [44, 46, 47]. Due to its high statistics ($\sim 800 \times 10^6$ $B\overline{B}$ pairs), Belle was also able to investigate highly suppressed FCNC processes [57, 58].

The next generation e^+e^- collider SuperKEKB will have a factor of 40 higher instantantious luminosity than its predecessor KEKB and will run longer in order to increase the integrated luminosity by a factor of 50.

3.1 The SuperKEKB Accelerator

The SuperKEKB accelerator is the upgrade of the KEKB accelerator at KEK, so it is installed in the same tunnel [3, 19]. It has two rings with a circumference of each 3016 m: The High-Energy-Ring (HER) containing the electrons and the Low-Energy-Ring (LER) for the positrons. Both rings store 2500 bunches.

KEKB had a peak luminosity of $2 \times 10^{34}\,\text{cm}^{-2}\text{s}^{-1}$ being still the world record of a collider. SuperKEKB aims for a luminosity of

Table 3.1: Machine parameters of the SuperKEKB accelerator, according to [3, 59]. The values of the beta function and the beam size are valid for the IP.

	LER (e^+)	HER (e^-)	
Beam energy	4.000	7.007	GeV
Energy spread	8.14×10^{-4}	6.49×10^{-4}	
Circumference	3016.315		m
Crossing angle	83		mrad
Horizontal emittance	3.2	4.6	nm
Vertical emittance	8.64	12.9	pm
Horizontal beta function	32	25	mm
Vertical beta function	0.27	0.30	mm
Horizontal beam size	10.2	7.75	µm
Vertical beam size	59	59	nm
Beam current	3.6	2.6	A
Bunch current	1.44	1.04	mA
Number of bunches	2500		
Bunch length	6.0	5.0	mm
Luminosity	8×10^{35}		$\mathrm{cm}^{-2}\mathrm{s}^{-1}$

$8 \times 10^{35}\,\mathrm{cm}^{-2}\mathrm{s}^{-1}$, a factor of 40 higher. Therefore, the beam current is doubled and an additional factor of 20 is gained by employing the so-called "Nano-Beam" scheme.

In the Nano-Beam scheme the longitudinal overlap of the colliding bunches is minimized in order to reduce the vertical beta-function at the ineraction point (IP). A larger crossing angle helps to achieve this, which is also beneficial for having separate focusing quadrupole magnets for the two beams and placing them closer to the IP. This results in limiting the detector background by synchrotron radiation and allowing a larger dynamic aperture for a longer beam lifetime, which is of major concern since intra-beam scattering loweres it by a factor of 15 – 20 compared to KEKB. It is clear, that a low emittance is mandatory.

The energy of the HER is changed from 8.0 GeV to 7.0 GeV, while the energy of the LER is increased from 3.5 GeV to 4.0 GeV. Hence, the Lorentz-boost $\beta\gamma$ of the center-of-mass system is reduced, but its energy $\sqrt{s} = 10.58\,\mathrm{GeV}$ stays the same. Although a larger $\beta\gamma$ is desirable for physics analysis, the higher LER energy helps to reduce

the emittance growth and to extend the beam lifetime by lowering the probability of intra-beam scattering. A feature of the lower HER energy is a reduced emittance.

The parameters of the SuperKEKB accelerator are shown in Table 3.1.

3.2 The Belle II Detector

The Belle II detector follows the basic design of the Belle detector. While keeping some of the components from Belle, a lot of its parts need to be exchanged for coping with the higher rates. The trigger rate will be higher, but also the occupancy caused by background will increase. This requires faster electronics and detectors with shorter dead times. Compared to Belle, a new detector for a better vertex resolution is introduced, the pixelated PXD (see Section 3.2.2).

The detector has a typical onion-skin layout (see Figure 3.1) and covers the polar angle between 17° and 150°. From the inside towards the outside it consists of a vertex detector followed by a drift chamber for charged particle tracking, detectors for particle identification, and an electromagnetic calorimeter. These components are inside a superconducting solenoid coil, its iron yoke is instrumented as an absorber for the K_L and μ detector. These subdetectors are described below. A more detailed description can be found in the Belle II technical design report [3].

3.2.1 The Beampipe

The central part of the IP chamber is a 22 cm long double-walled beryllium tube [3]. Beryllium has an atomic number of 4, so the probability of multiple scattering in the beampipe is mitigated. The inner pipe has an inner radius of 10.0 mm, a thickness of 0.6mm, and has got a 10 µm thick gold plating on the inside. The outer radius of the outer pipe is 12.0 mm and it has a thickness of 0.4 mm, such that there is a gap for coolant of 1.0 mm between the two layers.

Because the beryllium beampipe does not get hit directly by synchrotron radiation, the major heat source is the image current of the beam and is expected to be 81 W. A dehydrated liquid parafin like $C_{10}H_{22}$ is the chosen coolant, since beryllium is reactive eliminating water as a candidate. In order to keep the temparature below 10 °C, a cooling liquid speed of 10 m/s is sufficient [3].

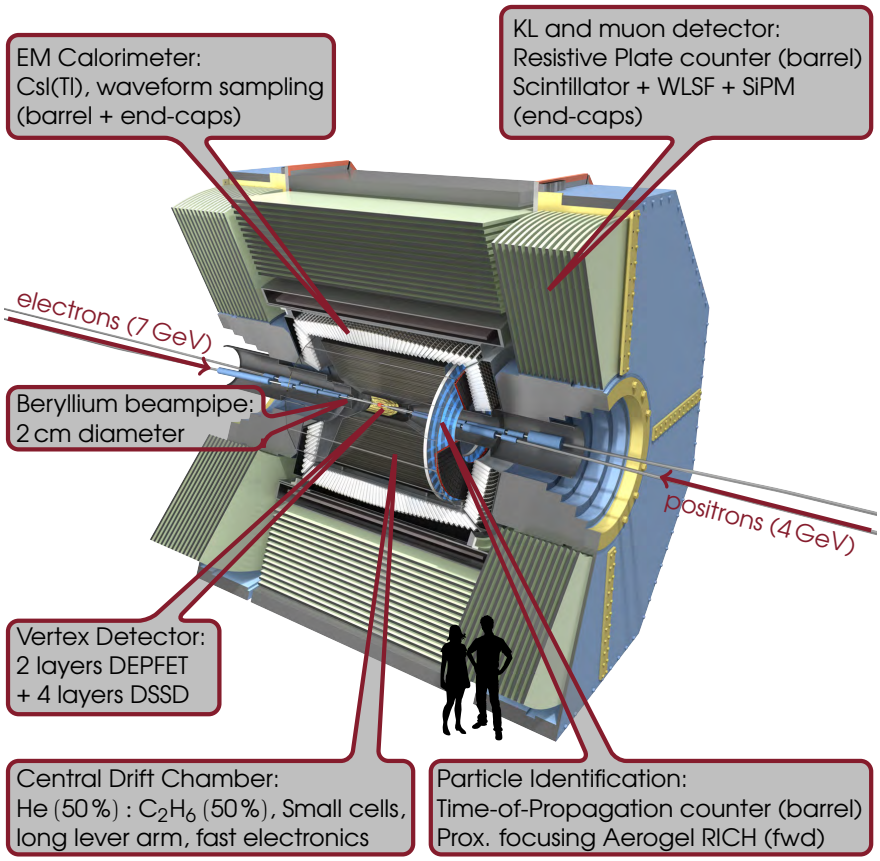

Figure 3.1: Schematic view of the Belle II detector, according to [60, 61]).

3.2.2 *The Pixel Vertex Detector*

The purpose of the innermost detector, the Pixel Vertex Detector (PXD), is the position determination of the B meson decay vertices [3, 62]. Therefore, it consists of two Layers of pixelated silicon sensors placed very close to the interaction point at radii of 14 mm and 22 mm. The high luminosity comes with a high level of beam induced background (c.f. 3.2.9) causing severely high hit rates, especially in the detectors in the vicinity of the beam pipe. In order to cope with these high rates, a layout of pixels rather than stripes is chosen.

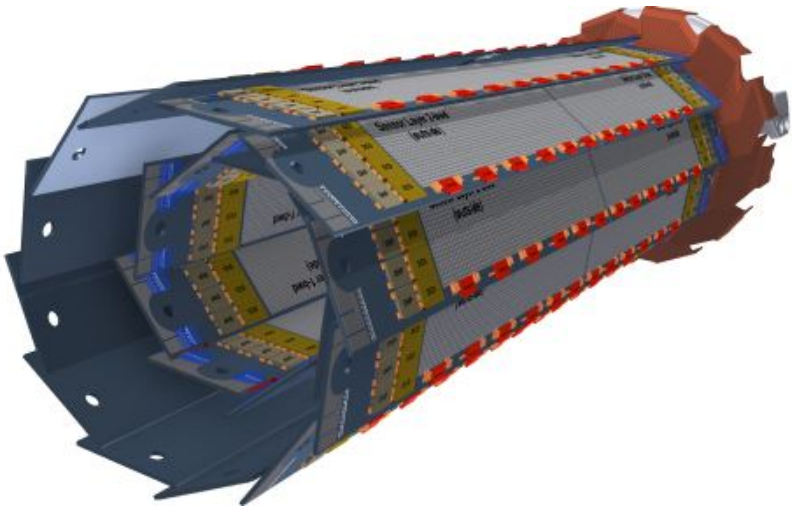

Figure 3.2: CAD drawing of the PXD. The light-grey surface is the sensor. The SWITCHERs are colored red and the DCDs are marked yellow. The grey parts next to the DCDs are the DHPs. Taken from [63].

Both PXD layers are subdivided into planar ladders and every ladder consists of two modules (also called half-ladders), each hosting one sensor. Each module is made of 400 µm thick silicon which is thinned down to 75 µm in the sensitive area. In total, there are $\approx 7.7 \times 10^6$ pixels. The dimensions of the PXD can be found in Table 3.2 and a CAD drawing is shown in Figure 3.2.

The physics program of Belle II requires the reconstruction of low momentum ($\approx 50\,\mathrm{MeV/c}$) charged particles. As one one can see in Figure 4.1, multiple scattering becomes an issue at these momenta. In consequence, a very little material budget is desirable. That is why the pixels are based on the DEPFET (DEPleted Field Effect Transistor) technology. It has an internal amplification, so that it can be made very thin (75 µm). Additionally a DEPFET sensor consumes little power, which makes air cooling sufficient for the detector acceptance volume. The readout electronics, which need active cooling, can be placed outside the acceptance [64, 65].

Table 3.2: Dimensions and properties of the PXD.

Layer	L1	L2
Radius [mm]	14	22
Ladders	8	12
Modules	16	24
Thickness (Module) [μm]	400	
Thickness (Sensor)[μm]	75	
Length (Sensor) [mm]	45	61.7
Width (Sensor) [mm]	12.5	
Sensitive Area $[cm^2]$	90	185
Pixels	3.072×10^6	4.608×10^6
Pixel per Sensor	250×768	
Pixel Size $[\mu m^2]$	55×50 60×50	70×50 85×50

DEPFET Technology

A DEPFET sensor [66, 67] consists of a silicon substrate with an integrated p-channel MOSFET. A p^+ contact at the back side caters for a fully depletion of the silicon bulk, when set to a sufficiently negative potential. An n doped area underneath the FET creates a minimum of the potential, which is called the "internal gate". Charged particles traversing the bulk create electron-hole pairs. The holes move towards the back contact, while the electrons are collected at the internal gate. In order to read out the pixel, the FET is switched on. By doing so, the amount of charge at the internal gate controlls the drain current. Thus, measuring the current provides information about the stored charge. The charge can be removed by setting a neighboring n^+ contact ("clear") to a positive voltage. The DEPFET principle offers two major advantages. Firstly, the internal amplification makes it possible to have very thin sensors. Secondly, a very high signal-to-noise ratio can be achieved, beacause the internal gate has a very small capacitance [66, 67].

Operation of a PXD Sensor

A PXD sensor is read out row-by-row ("rolling shutter mode"). Only the FETs of four neighboring rows are switched on at a time. It needs 20 μs until a whole sesnsor is read out. The drain currents

of the pixels flow via the drain lines to the end of the sensor. The current is digitized by four Drain Current Digitizers (DCDs) before the four The Data Handling Processors (DHPs) perform the zero-suppression and serialization for sending the data off module. The DCD and the DHP are ASICs, which are placed on the module, but outside the detector acceptance. The activation and clearing of the pixel rows is done by the SWITCHER ASIC located at the side of the sensor inside the acceptance [62].

3.2.3 *The Silicon Vertex Detector*

At radii $\gtrsim 4\,\text{cm}$ the expected hit rate is sufficient low to have a reasonable occupancy by instrumenting the VXD with strips [3]. The Silicon Vertex Detector (SVD) is a double-sided silicon strip detector (DSSD) complementing the PXD at radii between 38 mm and 135 mm (see Figure 3.3). It has four layers, from which the forward parts of the three outer layers are slanted towards the beam axis in order to minimize the material budget [68, 69]. See Table 3.3 for the properties of the SVD layers. All sensors have a thickness of $\approx 300\,\mu\text{m}$ [68].

The strips on the p-side are aligned to the z-axis, whereas the n-side strips run along the $r-\phi$ direction. The layers are divided into ladders, similar to the PXD. All ladders are assembled from three types of DSSDs. The innermost layer contains "slim" sensors, while the three outer layers are made from "large" sensors and "trapezoidal" sensors in the slanted parts. Table 3.4 lists the properties of the DSSD types. The SVD has in total 223 744 strips distributed over a sensitive area of $1.13\,\text{m}^2$.

The strips are read out by the 128-channel APV25 chip, which was originally developed for the CMS Tracker [70]. It has a shaping time of $\approx 50\,\text{ns}$, which is desirable for the background reduction, but makes it more sensitive to noise. Therefore, the chip has to be as close to the sensor as possible. The readout chips for the sensors at the forward and backward edge are placed outside the detector acceptance and the chips for the sensors in the center region are glued onto the ladder structure via the "Origami chip-on-sensor" concept [71]. Cooling of the chips is provided by a CO_2 cooling line on top of the ladder. For keeping the probability of multiple scattering at a minimum, the APV25 is thinned down to $100\,\mu\text{m}$. The material budget per layer is $\leqslant 0.73\,\%\,X_0$.

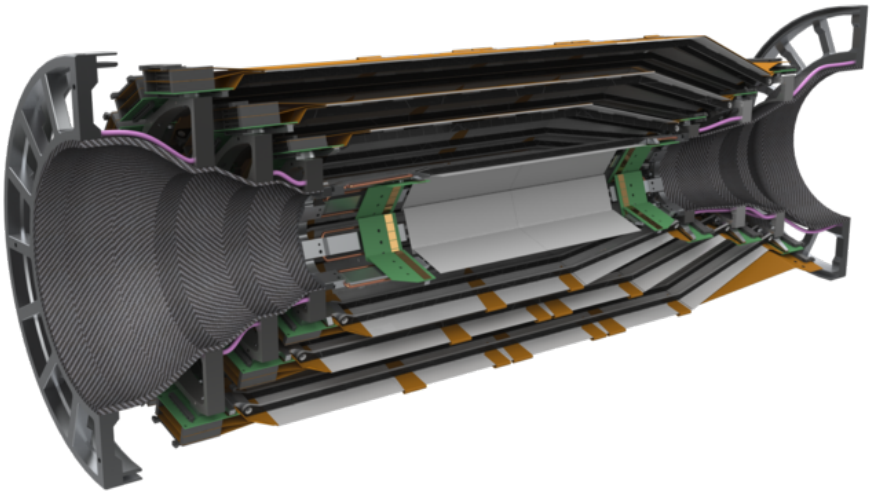

Figure 3.3: CAD rendering of the SVD. Taken from [72]

Table 3.3: Specifiactions of the SVD layers. For consistency with the PXD numbering scheme, the layers of the SVD are numbered from 3 to 6 [68, 69].

Layer	Radius [mm]	Ladders	Sensors/Ladder	Slant Angle
L3	38	7	2	168 °
L4	80	10	2	11.8 °
L5	104	12	4	17.2 °
L6	135	16	5	21.1 °

The data of the APV25 is sent off detector, where it is further processed, including a hit-time finding. This is performed by a lookup table implemented in an FPGA. Using three sample points around the pulse maximum, it deliveres a time window of ≈ 20 ns [3].

3.2.4 The Central Drift Chamber

The main tracking device of Belle II is the Central Drift Chamber (CDC), occupying a volume between the radii of 16 cm to 113 cm [3]. The track reconstruction allows precise momentum determination and also supplies a trigger signal. Additionally, the CDC provides a dE/dx measurement for particle identification.

Table 3.4: Properties of the three sensor types of the SVD [68, 69].

Sensor	Number of Strips		Strip Pitch [µm]		Size $[\mathrm{mm}^2]$
	p-side	n-side	p-side	n-side	
Slim	768	768	160	50	122.8×38.4
Large	512	768	240	75	122.8×57.6
Trapezoidal	512	768	240	$50 - 75$	122.8×57.6 -38.4

The 14 336 sense wires and 42 240 field wires are arranged in nine superlayers, each being formed by six layers of square drift cells, containing one sense wire (only the innermost superlayer has eight layers). The innermost sense wire is at a position of $r = 16.8\,\mathrm{cm}$ and the outermost sense wire is placed at $r = 111.14\,\mathrm{cm}$. The sense wires are made from gold plated tungsten with a diameter of 30 µm, while the aluminium field wires have diameter of 126 µm. Each superlayer is either an axial layer ("A"), which has wires parallel to the z-axis, or a stereo layer, its wires are slightly skewed with respect to the z-axis. The stereo layers have either a positive or a negative tilt angle, making them a "U" or a "V" layer. The combination of axial and stereo layers allows a 3D track reconstruction. The order of the superlayers (from the inside to the outside) is AUAVAUAVA. The gas is the same as in the Belle CDC, a 50 : 50 mixture of He and C_2H_6 [3].

3.2.5 *Particle Identification*

Particle identification (PID) detectors of Belle II are the Time-of-Propagation counter in the barrel part and the proximity-focusing Aerogel Ring-Imaging Cherenkov detector in the forward endcap. The main purpose of these detectors is the separation of charged pions from charged Kaons, while introducing little material in front of the Electromagnetic Calorimeter [3].

Time of Propagation Counter

In the barrel part, the Time-of-Propagation counter (TOP) is used for the identification of charged particles [73]. It consists of 16 $275 \times 44.3 \times 2\,\mathrm{cm}^3$ quartz bars between the CDC and the Electromagnetic Calorimeter. The quartz serves as a radiatior for the cre-

ation of Cherenkov photons, which are then internally reflected to the end of the bar, where they are detected by micro-channel plate (MCP) Photomultipliers (PMTs) [74]. The time of arrival and the x and y coordinate are measured. Pions and kaons produce different patterns in this 3-dimensional space. Thus, liklihoods for the pion- and the kaon-hypothesis can be calculated, from which the decision for one particle specie is made [3, 73].

The cromaticity of the Cherenkov photons reduces the separability of pions and kaons due to the smearing of the arrival time. In order to correct for this effect, the forward end of the quartz bar has a focusing mirror. This has also the advantage, that the PMTs are only at the backward end of the bar, saving the space in the forward direction, that would be needed for the cables [3].

Aerogel Ring Imaging Cherenkov detector

The proximity-focusing Aerogel Ring-Imaging Cherenkov detector (ARICH) is used in the forward endcap to perform the identification of charged particles [3, 75]. It consists of two 2 cm thick layers of silica-aerogel as radiator [76]. After a gap of 20 cm for the expansion of the photon rings, an array of Hybrid Avalanche Photo-Detectors (HAPDs) detects the Cherenkov photons [77].

The refractive indices of the two aerogel layers are 1.055 and 1.065. This leads to a larger opening angle of the light cone from the second layer overlapping with the first cone at the HAPD. This (proximity) focusing effect reduces the blurring of the Cherenkov rings, and thus improve the resolution and discrimination power of different particle hypotheses.

The HAPD is an Avalanche Photo-Detector with a photocathode at a potential of $\approx -8\,\mathrm{kV}$ 2 cm in front of it. The front-end readout is done by an ASIC followed by an FPGA. The ASIC contains a preamplification stage, a shaper, and a comparator [3].

3.2.6 The Electromagnetic Calorimeter

The task of the Eletromagnetic Calorimeter (ECL) is the high efficiency detection of photons with high resolution in energy and position. Furthermore, the ECL is needed for the identification of electrons and is used in combination with the KLM (Section 3.2.8) for the detection of K_L^0 mesons. Additionally, it is used as a luminosity

monitor and source of the trigger. While reusing the CsI(Tl) crystals and photodiodes of Belle, the Belle II ECL electronics is new [3].

The barrel section is 3 meters long and has an inner radius of 1.25 m. It is formed by 6624 crystals pointing to the interaction point. The endcaps are placed at $z = 1.96\,\text{m}$ and $z = -1.02\,\text{m}$, consisting of 2112 crystals. The crystals have an averaged cross section of $6 \times 6\,\text{cm}^2$ and a length of 30 cm corresponding to 16, 1 radiation lengths. Two $10 \times 20\,\text{mm}^2$ photodiodes are glued to the back of each crystal for the collection of the scintillation light [3].

The higher background at Belle II imposes two major issues on the data acquisition. The first one is called "pile up noise". It is caused by a low-energy photon background, its fluctuation causes an increase of the noise level. The second problem is caused by a high-energy photon background, which creates background clusters. To be able to cope with these issues, the shaping time is shortened to 0.5 µs (A second shaper for generating triggers has an integration time of 0.2 µm) and the signals undergo a waveform analysis. For that reason, a flash ADC samples the signal at a rate of 2 MHz. When receiving a trigger, 16 sample points are fit to a signal function, determining the event time and the pulse height. After an energy dependent cut on the event time, the rate of fake photons can be reduced by a factor of 7 while losing only 7 % of the true photons above 20 MeV. However, an energy threshold of 30 MeV is required to reduce the fake rate caused by pile up noise [3].

3.2.7 The Superconducting Solenoid

Momentum determination of charge particles is only possible by reconstructing their flight path inside a magnetic field. Therefore, the superconducting solenoid, which is reused from Belle, provides a homogenius magnetic field of 1.5 T parallel to the z-axis. It encloses the ECL and its iron yoke is used as absorber material of the K_L^0 and µ Detector. The superconducting coil made of NbTi/Cu is inside a cryostat ranging from $r = 1.7\,\text{m}$ to $r = 2.0\,\text{m}$ at a temperature of 4.2 K [78]. It has a nominal current of 4400 A and stores an energy of 35 MJ.

3.2.8 The K_L^0 and µ Detector

The K_L^0 and µ detector (KLM) is the outermost subdetector of Belle II [3]. It is located outside the superconducting solenoid and

consists of alternating layers of 4.7 cm thick iron plates and active detector elements (4.4 cm). The iron plates serve as an absorber for hadrons (especially K_L^0 mesons), as well as the flux return of the solenoid. Muons travel along almost straight paths through the KLM, leaving signals in the active detector elements, whereas K_L^0 mesons, that create hadronic showers in the ECL or the KLM, are detected by the signal in the ECL or KLM with no associated charged track in the CDC.

In the octagonal shaped barrel part, the detection is performed by the glass-electrode resistive plate chambers (RPC) from the Belle detector. There are 15 superlayers of RPCs and 14 layers of iron plates. A superlayer consists of two RPCs separated by a thin insulator and pick up strips attached to each side. The RPC electrodes are made from 2.4 mm thick float glass separated by 2 mm gaps filled with a gas mixture of 62 % HFC-134a, 30 % argon, and 8 % butane-silver [3].

Due to the long dead time of RPCs caused by the reformation of the electric field after a discharge, RPCs are no option for the high background environment of the KLM endcaps of Belle II. The main background source are low-energy neutrons ($10 - 100$ keV), originating from the beam line outside the detector. Instead of RPCs, scintillating polystyrene strips (cross section $7 \times 40\,\text{mm}^2$) will be used in the 14 detector layers of the endacp. The number of iron plates in the endcap is also 14. The scintillation light is collected in wavelength-shifting fibers (WLSF), which lead to Silicon Photomultipliers (SiPM) at the end of the strips. The SiPM signal is amplified off detector and sampled with 1 GHz. Similar to the ECL, the waveform is fit by a signal funtion to obtain the event time and the pulse height. A timing relosultion of ≈ 1 ns can be achieved [79].

3.2.9 *Background Sources*

The high luminosity will result in a high rate of $B\overline{B}$ and other hadron production events as well as $\mu^+\mu^-$ and $\tau^+\tau^-$ events, but of course it causes also a high background level. Due to the independent final focus quadrupoles for the two beams it can be avoided, that the sensitive area of the detector is hit by synchrotron radiation. In the following, the background sources, that have to be considered, are presented [3].

Beam-Gas Scattering

Having an average pressure of $\approx 10^{-7}$ p [80], there is still some residual gas in the vacuum system scattering with the beam via emission of bremsstrahlung and coulomb scattering. The electrons and positrons then leave their orbit and hit the beam pipe and magnets, producing showers, that can reach the detector and generate background hits [3].

Touschek Effect

The Touschek effect is the scattering of a beam particle with another particle from the same bunch [81]. Again, the scattered particles create showers in the wall of the vacuum chamber and the magnets. Since it is proportional to E^{-3}, only the Touschek contribution from the LER is significant [3].

Radiative Bhabha Scattering

Radiative Bhabha scattering ($e^+e^- \rightarrow e^+e^-\gamma$) happens at the interaction point, where the particles collide. There are two ways, in which this process contributes to the overall background pollution. The first one is the production of free neutrons by the giant photonuclear resonance mechanism caused by the absorption of the photon by the iron in the magnets. The neutron radiation is mainly an issue for the endcap KLM. The second source of background is the over-bending of the slowed down beam particles in the magnets. Similar to the beam-gas scattering and the Touschek scattering, showers are created in the beam pipe and the magnets, that can hit the detector [3].

Two photon QED

Second order QED precesses involving the exchange of two photons can also happen in e^+e^- collisions. The main reaction is the electron-positron pair production ($e^+e^- \rightarrow e^+e^-e^+e^-$). Very low momentum e^+e^- pairs are produced and hit the innermost detector layers. Creating a hit rate being approximately proportinal to $1/r^2$, this is by far the main background source for the PXD and the SVD [3].

3.2.10 The Level 1 Trigger

The trigger of Belle II is ordered in two levels. The first one is the Level 1 trigger, which selects events based on fast and coarse decisions [3]. This reduces the rate of the data, that is analyzed by the High Level Trigger, which performs an online reconstruction for a physics based even selection, c.f. next section.

The Level 1 trigger is divided into several sub-triggers. The most important triggers are the three CDC triggers and the ECL trigger. The CDC 2D trigger uses only the axial wires and performs a track finding and track fitting in the $r-\phi$ plane. The CDC 3D trigger uses the found 2D tracks and uses the stereo hits for an $r-z$ fit in order to obtain the 3D information [3]. Additionally, there is a z-vertex trigger. It determines the z coordinate of the vertex by feeding the parameters of the found 2D track together with the stereo hits into an artificial neural network [82]. Hence, the CDC triggers provide information about the track parameters like charge, momentum, vertex, and multiplicity.

The ECL trigger is supposed to run in two complementary configurations. The first is an overall energy trigger, which is asserted, when a certain threshold of total energy is exceeded. The second trigger is issued, when a certain number of isolated clusters are counted.

The KLM sub-trigger extends the CDC triggers by the identification of muon tracks. A precise timing is attained by the PID detectors in the barrel (TOP) as well as in the forward part (ARICH).

The sub-triggers are sent to the Global Decision Logic (GDL), which makes the final decision, wether a trigger should be generated. It operates in a sequence of four steps [3]:

1. The latencies of the sub-triggers are adapted to each other.
2. The main trigger decision is made in the second step:
   - The physics triggers require a certain track multiplicity, a total energy deposition in the ECL, or a certain number of ECL clusters.
   - The calibration triggers search for a Bhabha, $\gamma\gamma$, or a μ pair signature. Additionally, a delayed Bhabha trigger mimics a random trigger scaled with the luminosity.

- There are also veto triggers for two photon QED events and for the beam injection. During injection, the beam is unstable and produces an increased background level.

3. Due to the high cross section of the calibration events, rate of the calibration triggers are prescaled, i.e. only one of N triggers are accepted, when N is the prescaling factor.

4. The timing of the trigger is determined by using the timing information from the PID detectors and the ECL.

At the target luminosity of $8 \times 10^{35}\,\mathrm{cm}^{-2}\mathrm{s}^{-1}$ the expected trigger rate is on average 30 kHz.

3.2.11 *Data Acquisition and Online Data Reduction of the PXD*

Due to the high background in the PXD, which corresponds to an occupancy of up to 3 %, and an average trigger rate of 30 kHz the PXD has an expected output data rate of $\gtrsim 20$ GB/s. This is more than ten times the rate of all other subdetectors combined and makes an online data reduction necessary [4].

The PXD Readout

In Section 3.2.2 the PXD with its on-module ASICS is described. Each half-ladder is connected to an FPGA board called Data Handling Engine (DHE). Upon a trigger receipt, the DHEs read out the DHPs. The fact, that the outer layer has a lower occupancy than the inner layer, motivates a load balancing. Therefore, two DHEs from the inner layer and three DHEs from the outer layer send their data to a Data Handling Concentrator (DHC), which then combines the data, clusterizes the hits and sends it on four links to the Online Selection Nodes (ONSEN). The combination of DHE and DHC is called DEPFET Handling Hub (DHH). In total, there are eight DHHs with 40 input and 32 output links [5, 83].

The ONSEN System

The ONSEN performs data reduction, by sending only pixel data inside Regions of Interests (ROIs) to the Event Builder 2. The ROIs are geometric regions on the PXD sensor area in a rectangular shape.

They are determined by two independent mechanisms. One is the Data Acquisition Tracking Concentrator Online Node (DATCON), running on an FPGA based platform almost identical to the ONSEN hardware. It performs online tracking only with SVD data and extrapolates the tracks to the PXD. The intersections of with the sensors are then the center of an ROI. The other ROI source is the High Level Trigger (HLT). It receives data from all subdetectors except the PXD, collected by the Event Builder 1 and runs on a multicore PC farm in order to perform online full reconstruction for an event selection. The found tracks during this process are also used for the determination of the ROIs [3, 84].

The ONSEN is comprised of 33 xTCA-based FPGA Processor (xFP) cards hosting a Xilinx Virtex-5 FX70T FPGA. The xFP cards are carried by an AdvancedTCA carrier board in groups of four. Each carrier board is equipped with a Virtex-4 FX60 FPGA and is placed inside an AdvancedTCA shelf, where they communicate via the backplane. One xFP card acts as the Merger Node. It combines the ROI information. Afterwards, it distributes the merged ROIs to the 32 Selector Nodes. The Selector Nodes receive the PXD data from the DHCs and select only the pixel inside the ROIs. Due to the latency of the HLT of up to 5 s (DATCON: 10 µs), the Selector Nodes need to buffer the PXD, until the receipt of the HLT ROIs. The reduced PXD data is then sent to the Event Builder 2 [4, 83].

The overall reduction factor of the PXD data is ≈ 30. A factor of 10 is achieved by a 10 % coverage of the PXD sensors by ROIs, while an additional factor of 3 is acquired by the HLT event selection [4]. The whole process of the PXD data acquisition and reduction is illustrated in Figure 3.4.

3.2.12 *Software*

The software of Belle II is integrated into the Belle II Analysis Framework (BASF2) [85]. It is an object oriented framwork based on C++. The framework comprises a whole variety of modules, that fulfill individual tasks. There are modules, that read or write data from or to a file. Other modules generate physics events or run a full detector simulation. The tracking algorithms are implemented as BASF2 modules. The modules can be chained to a sequence, which is processed on event basis. Therefore, the so-called “steering files”, scripts written in Python, build the interface to the modules. In a

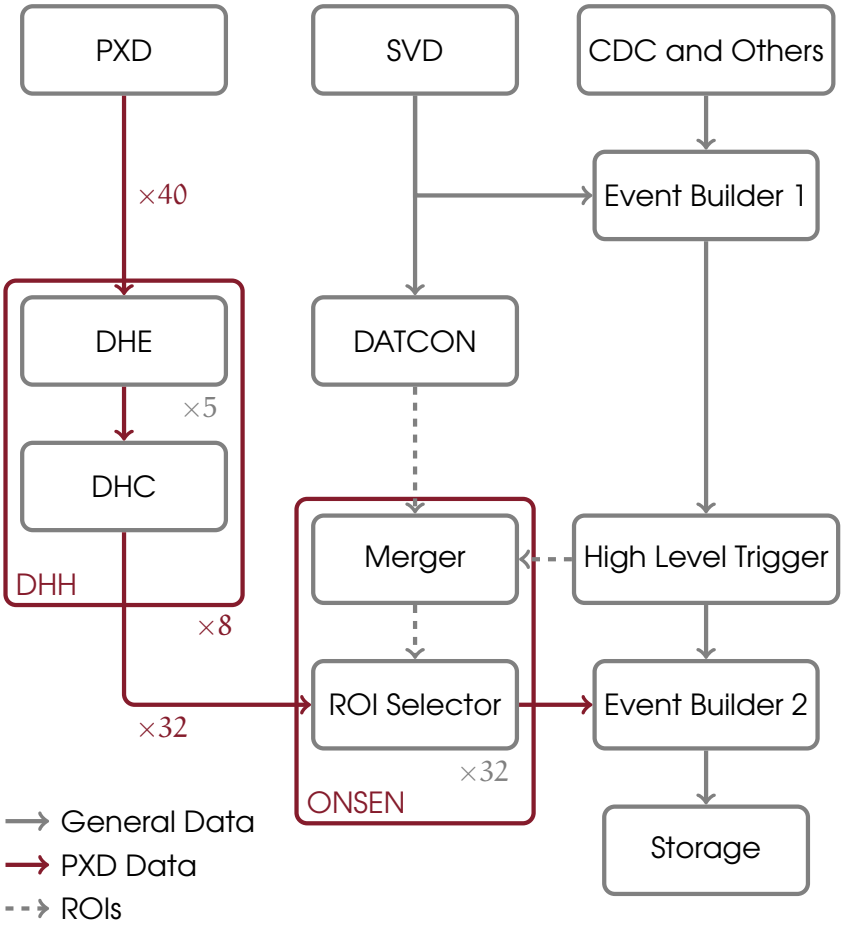

Figure 3.4: Illustration of the data acquisition and reduction of the PXD. The arrows represent data paths. The HLT sends not only the ROIs to the Merger Node, but also a trigger decision. According to [4, 83].

steering file, the user instantiates the modules, passes parameters to them and add them to a "path". This path is the above mentioned sequence, which is then finally executed in the steering file. While processing a path, the modules have access to the "DataStore". The DataStore is based on ROOT [86] and is used for the transfer of data between the modules. For example one module uses CDC hits as input and produces track candidates, which are then written to the DataStore. The next module uses the track candidates for a track fit and writes the fit tracks to the DataStore.

The framework is not only used for offline data processing, but also online for monitoring and the HLT [85].

Chapter 4

TRACK RECONSTRUCTION

4.1 Interaction of Charged Particles with Matter

RECONSTRUCTING a charged particle track requires a detection device, in which the particles interact and produce signals, that can be read out electronically.

4.1.1 Ionization

When charged particles traverse matter, they mainly interact with the electrons in the atomic shell, leaving the atoms ionized. The maximum energy transfer by a particle with mass M in a single collision is given by [6]

$$W_{max} = \frac{2m_e c^2 \beta^2 \gamma^2}{1 + 2\gamma m_e/M + (m_e/M)^2} \quad , \tag{4.1}$$

where m_e is the electron mass, $\beta = v/c$ the velocity of the incident particle in units of c, the speed of light. $\gamma = 1/\sqrt{1-\beta^2}$ is the usual Lorentz factor. The mean energy loss per travelled distance (also called stopping power) of a charged particle is described by the famous "Bethe equation" in the region of $0.1 \lesssim \beta\gamma \lesssim 1000$ [6, 88]:

$$\left\langle -\frac{dE}{dx} \right\rangle = K z^2 \frac{Z}{A} \frac{1}{\beta^2} \left[\frac{1}{2} \ln \frac{2m_e c^2 \beta^2 \gamma^2 W_{max}}{I^2} - \beta^2 - \frac{\delta(\beta\gamma)}{2} \right] \quad . \tag{4.2}$$

Z and A are the atomic number and the atomic mass of the absorber, while z is the charge of the particle in units of e. I is the mean excitation energy of the absorber and $K = 0.307075\,\mathrm{MeV\,mol^{-1}\,cm^2}$ is a constant. The last term in (4.2), $\delta(\beta\gamma)/2$, represents the density effect, a correction at high energies taking into account the polarization of the medium. The Bethe equation is not valid for electrons and positrons.

It needs to be considered, that only the mean value of the stopping power is described by (4.2). Collisions with very high-energy

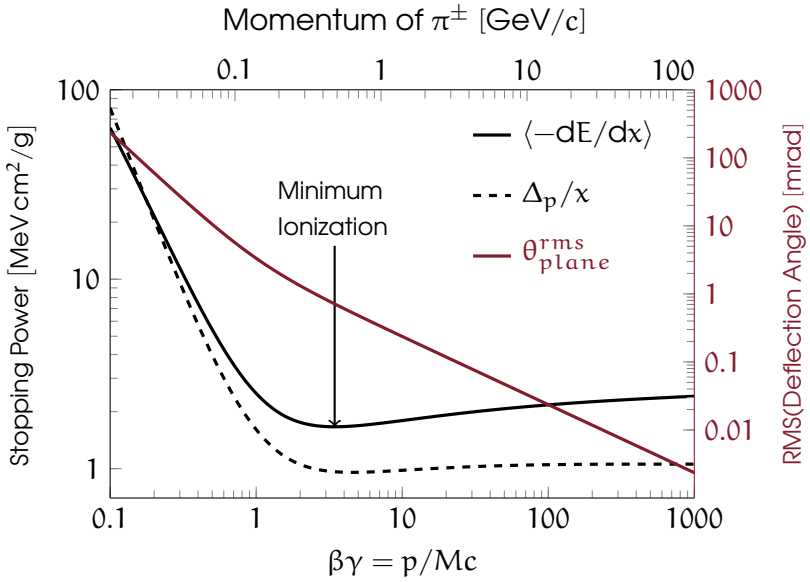

Figure 4.1: Stopping power and the deflection angle rms of a charged pion in 100 µm silicon. The top axis shows the values of the pion momentum, while the bottom axis represents $\beta\gamma$. The most probable energy loss is up to a factor 2 smaller than the mean energy loss. The fact, that Δ_p/x (dashed black) exceeds $\langle -dE/dx \rangle$ (solid black) for small $\beta\gamma$, is due to the finite value of x, by which Δ_p is divided, in contrast to the infinitesimal value of dx. The scale of the red curve describing the deflection angle rms is plotted on the right side. Only for small momenta it is signficant. The values are calculated according to Equation (4.2) and (4.3) and using the parameterization for $\delta(\beta\gamma)$ from [87].

depositions are rare, but they increase the mean value dramatically, such that about 10 % of the collisions lead to an energy deposition higher than the mean. Therefore, a much better suited quantity for describing single-particle energy depositions is the most probable energy loss. For an absorber of thickness x in $\mathrm{g\,cm^{-2}}$, it can be expressed by [6, 89]

$$\Delta_p = \xi \left[\ln \frac{2m_e c^2 \beta^2 \gamma^2}{I} + \ln \frac{\xi}{I} + j - \beta^2 - \delta(\beta\gamma) \right] \quad , \tag{4.3}$$

where $\xi = (K/2)(Z/A)(x/\beta^2)\,\mathrm{MeV}$ is the Landau parameter an $j = 0.2$.

In Figure 4.1 the $\langle -dE/dx \rangle$ as well as the most probable energy loss divided by x is plotted against $\beta\gamma$ for a charged pion in 100 µm silicon. One can see, that both are having a minimum around $\beta\gamma \simeq 3$. For larger $\beta\gamma$ the stopping power is increasing very slowly and reaching a plateau, whereas for smaller $\beta\gamma$ the stopping power is increasing very fast.

4.1.2 *Multiple Scattering*

While passing through matter, a charged particle does not only lose energy, but also gets deflected by multiple Coulomb scattering from nuclei. Hadronic projectiles also undergo scattering induced by the strong interaction. Many subsequent small-angle deflections result in a Gaussian distributed net scattering angle due to the central limit theorem with a mean of zero [90]. Less frequent large-angle deflections lead to non-Gaussian tails in the distribution. Excluding the tails, the standard deviation of the planar projected deflection angle can be written as [91, 92]

$$\theta_0 = \theta_{\mathrm{plane}}^{\mathrm{rms}} = \frac{13.6\,\mathrm{MeV}}{\beta p c}\, z \sqrt{x/X_0} \left[1 + 0.038 \ln(x/X_0) \right] \quad . \tag{4.4}$$

The thickness of the material is x, while p (β, z) is the momentum (velocity in units of c, charge in units of e) of the incident particle. The radiation length X_0 is a material constant describing the mean length, after which the energy of a high-energy electron is reduced by bremsstrahlung to $1/e$ of its initial energy. The behavior of θ_0 in dependence of $\beta\gamma = p/Mc$ is shown in Figure 4.1.

4.2 Track Parameterization

Charged particles in a homogenious magnetic field travel along a helix shaped trajectory. The helix axis is fixed to be aligned with the orientation of the magnetic field. A helix with its axis being parallel to the z axis can be described by 5 parameters. The helix has a radius R and its center is at the position (x_0, y_0). The pitch is $2\pi h$ and the helix has a z-offset of z_0. A position on the helix can now be expressed by

$$\mathbf{r}(t) = \begin{pmatrix} x(t) \\ y(t) \\ z(t) \end{pmatrix} = \begin{pmatrix} x_0 + R\cos t \\ y_0 + R\sin t \\ z_0 + h\,t \end{pmatrix} \quad , \tag{4.5}$$

where t is a dimensionless parameter, c.f. Figure 4.2(a). When a coordinate $(\tilde{x}, \tilde{y}, \tilde{z})$ is known to lie on the helix, the parameterization from Equation (4.5) can be rewritten to

$$\mathbf{r}(t) = \begin{pmatrix} x(t) \\ y(t) \\ z(t) \end{pmatrix} = \begin{pmatrix} \tilde{x} \\ \tilde{y} \\ \tilde{z} \end{pmatrix} + \begin{pmatrix} R(\cos\vartheta - \cos(t+\vartheta)) \\ R(\sin\vartheta - \sin(t+\vartheta)) \\ h\,t \end{pmatrix} \quad , \tag{4.6}$$

where ϑ is defined according to Figure 4.2(b). In this parameterization $t = 0$ corresponds to $\vec{r} = (\tilde{x}, \tilde{y}, \tilde{z})$.

The task of track reconstruction is to identify hits in the detector, which belong to a common particle and to parameterize its track. Due to multiple scattering (c.f. Section 4.1.2) the trajectory is not a perfect helix, especially for low momentum particles. In order to account for that, much more sophisticated models exist and the helix can only be used as an approximation.

The reconstruction of tracks is usually divided into two parts. The first step is the track finding. Here, the hits forming a track are identified and a first estimation of the track parameters is performed. The second step is the fitting of the track, where the found tracks are fit to extract the track parameters and to obtain a covariance matrix of the parameters and a quality estimation of the fit. During this process, hits may be removed from the track, or even hits, that have not yet been assigned to the track, are added to the track [93].

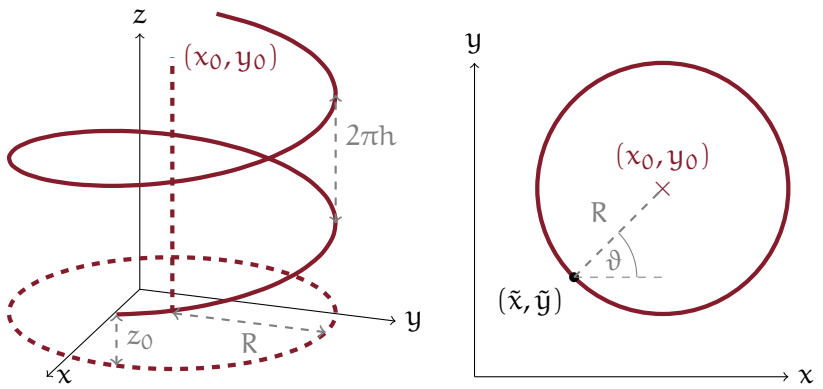

(a) *(b)*

Figure 4.2: Parameters of a helix. *(a)* Illustration of the parameters used in (4.5). *(b)* Projection of a helix onto the $x - y$ plane and definition of the angle ϑ used in Equation (4.6).

4.3 Track Finding

In order to identify a helix shaped track, the particle must have created at least three hits. The different track finding techniques can in general be divided into two different classes. The first contains global methods. These take all available hits at once and try to find track patterns. In contrast to this, there is the second group, the local methods. They start with a hit as a seed, combining it with a neighboring hit, in order to construct a track by subsequently adding suitable hits [93].

4.3.1 Global Method: Hough Transform

The Hough transform is used for feature extraction, when a set of points (hits) in space is given. Although it was first designed to identify charged tracks on bubble chamber pictures [94], nowadays it is often used in computer vision and image processing, too. It is based on the transition from the real space to a parameter space. To demonstrate the principle of the Hough transform, the search for straight lines is explained in the following. In the reference frame (x', y'), a commonly known parameterization is $y' = m\,x' + b$ with m being the slope and b the y' intercept. This lacks the possibility to

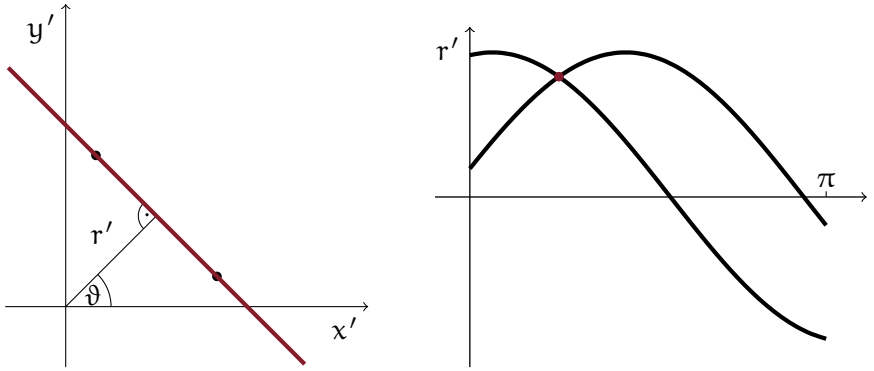

(a) *(b)*

Figure 4.3: Principle of the Hough transform. ***(a)*** Two points in real space with the straight line going through both of them. The parameterization is the normal form using r' and ϑ. ***(b)*** Each point is represented by a sinusoid in parameter space. The meeting point of the curves parameterizes the common straight line of the points in real space.

describe a straight line parallel to the y' axis. Thus, a better suited parameterization is the normal form [95], defined by

$$r' = x' \cos\vartheta + y' \sin\vartheta \quad , \tag{4.7}$$

where ϑ is the angle between the x' axis and the normal of the straight line and r' is the smallest distance of the line from the origin, as shown in Figure 4.3(a). Restricting the domain of the angle to $[0, \pi)$, and with $r' \in \mathbb{R}$, every line in the $x' - y'$ plane is represented by a unique point in the $r' - \vartheta$ parameter space. A single point in real space is then described by all possible lines through this point, and hence a sinusoid curve in parameter space, described by Equation (4.7). More than one point in real space corresponds to several curves in parameter space. The intercept point of the sinusoids parameterizes the line connecting the points, c.f. Figure 4.3. Accordingly, finding straight lines is achieved by finding the intercection of multiple curves in parameter space. The classical ansatz is to discretize the parameter space, i.e. to describe it by a 2D histogram. Every line crossing a bin increments the bins content. Thus,

the identification of the pattern is achieved by finding a peak in a histogram. Usually the points are not perfectly aligned. Thus, the sinusoids in $r' - \vartheta$ space do not meet exactly at one point. This makes it necessary to tune the binning to a compromise between too coarse (multiple peaks are seen as a single peak) and a too fine (not perfectly aligned points does not get recognized). An improved peak finding also takes the neighboring bins into account. This allows a finer binning and therefore a higher resolution.

The bin-by-bin checking, wether a curve is contained in the bin, takes a lot of time and requires a lot of memory. Many bins hold a count of zero, which results even in unused memory. A faster and resource saving ansatz is the fast Hough transform [96]. Here, a divide and conquer approach is applied. The parameter space is divided into four rectangular sub spaces, for which the number of sinusoids is counted. Only if this number exceeds a threshold, there may be an intercept of a sufficient number of curves. Accordingly, this procedure is repeated recursively: The sub space is further divided, and so on (c.f. Figure 4.4). With an increasing recursion level, the resolution gets finer. When the desired resolution is reached, the recursion can be stopped and the remaing sub spaces yield the parameters of the patterns. An additional peak finding is not needed.

In principle, the (fast) Hough transform can be applied to the search for every kind of pattern. Accordingly. the points in real space are described an $N-1$ dimensional hyper plane in an N dimensional parameter space (for the case of two parameters of a straight line, this is the one-dimenional sinusoid in $r' - \vartheta$ space). For a complicated pattern described by a lot of parameters, two difficulties need to be considered. Firstly, the misalignment of the points in real space causes a large separation of the hyper planes in parameter space. The second issue is the computational effort of checking, wether a hyper plane is crossing an N dimensional rectangle. This effectively limits the application of the (fast) Hough transform to patterns with few parameters.

A helix has five parameters, but the projection onto the $x - y$ plane reduces its shape to a circle, which has only three parameters: The two-dimensional center point and the radius. Very often, one reduces the number of parameters even further, by mapping the circle

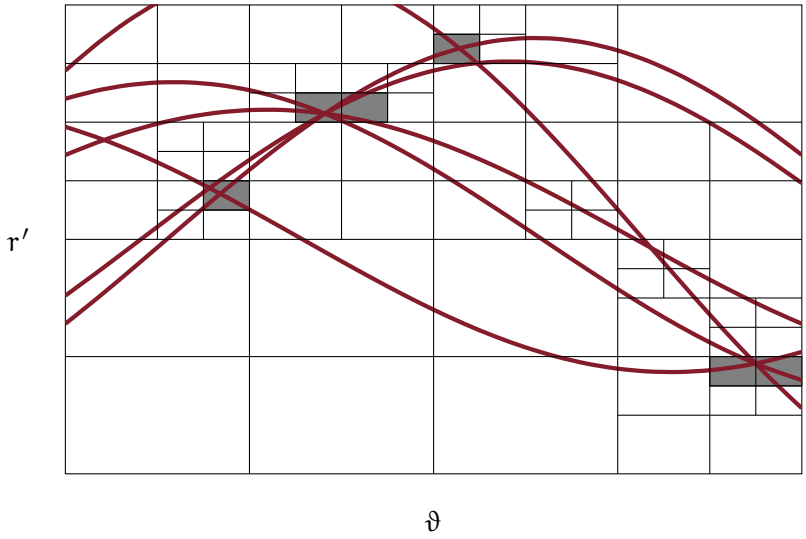

Figure 4.4: Principle of the fast Hough transform. By the employment a divide and conquer approach, the Hough space is devided into smaller sub spaces, for which the number of traversing sinusoids is checked. In this example, the threshold is set to three. This effectively zooms into the peak regions. The gray rectangles are the active sub spaces after the fourth iteration.

onto the "conformal plane", which is done by the transformation

$$\begin{aligned} x \to x' &= \frac{x - \tilde{x}}{\rho^2} \quad , \\ y \to y' &= \frac{y - \tilde{y}}{\rho^2} \quad , \text{with} \\ \rho^2 &= (x - \tilde{x})^2 + (y - \tilde{y})^2 \quad , \end{aligned} \tag{4.8}$$

where $(\tilde{x}, \tilde{y})$ is a reference coordinate, that has to be specified. This transformation preserves the angles, hence it is a conformal transformation [97]. It has the property, that a circle, which goes through the reference point, is transformed into a straight line in the conformal plane. Using the normal parameterization of the resulting straight line, the angle ϑ of (4.7) is exactly the angle ϑ of (4.6) and the parameter r' is related to the radius of the circle via $r' = 1/2R$. The circle

in Figure 4.2(b) is transformed into the straight line in Figure 4.3(a). Usually, a charged track is expected to originate from the primary vertex at the IP. Therefore, the IP is often used as the reference point.

4.3.2 Local Method: Cellular Automaton

A Cellular Automaton is a model for processes, that only interact locally, i.e. the evolution of a state depends only on its local surrounding. It is described by cells which attains one state of a defined set of states. Each pair of cells are either noughbors or not. The cells evolve in discrete time steps depending on its current state and the states of the neighboring cells [98].

Usually, a pair of hits form a cell. Cells sharing a hit are neighbors. The states are numbered, where the lowest state refers to the initial state, which can evolve into higher states. The evolution of the states can be expressed by the rule, that every cell with at least one neighbor on the inside (smaller radial coordinate in the detector reference frame), increments its state by one when fulfilling certain selection criteria. The Cellular Automaton converges, when the states no longer change [99, 100].

4.4 Track Fitting

After a track candidate is found, a fit provides the parameters of the track. Again, there are global and local methods [93]. A global approach is a least squares fit. The parameters of the track are obtained by a global fit. A local method is the well established Kalman-Filter [101]. It starts at the first hit of the track with a seed momentum estimated by the track finder. After it predicts the position of the next hit, the measured position is used for the correction of the track parameters. These steps are repeated, until every hit was used. The Kalman Filter is able to incorporate material effects, such as multiple scattering (c.f. Section 4.1.2).

4.5 A Note on Ghost Hits and Clusters

In order to measure a two-dimensional position, one employs either pixels (PXD) or one combines two one-dimensional measurements (SVD,CDC). Here, the direction of the two sensitive elements must

not be parallel, otherwise no 2D information can be obtained. In the SVD the n and p strips are perpendicular to each other, while the stereo wires of the CDC are skewed by the stereo angle with respect to the axial wires. Having a high occupancy leads to ambiguities when determining the 2D position: When N hits occur in one sensor, they cause in the worst case $2N$ firing strips. There are then N^2 possible strip-strip combinations, from which $N(N-1)$ do not correspond to the true hit. These fake hits are refered to as ghost hits. Figure 4.5 illustrates the creation of ghost hits.

Typically, a charged particle causes more than a single pixel or strip to fire. Theses connected groups of pixels or strips are called clusters. Thus, one hit is associated to one pixel-type cluster or two strip-like clusters.

4.6 *Artificial Neural Networks*

In order to achieve an optimal signal to background ratio, it is necessary to decide, wether a certain entity (i.e. a hit or a track candidate) is background or signal. A hit is characterized by several values (position, charge, cluster size, etc.). For n such characteristics, a hit is therefore represented by a point in an n dimensional space, in general $\mathbb{R}^n$. Signal and background can only be separated, if they have distinct probability density functions (PDFs) in this space.

If the exact PDFs were known, the assignment to either the signal or background class would be straight forward: Let $\mathbf{x} \in \mathbb{R}^n$ represent a hit and $f_s(\mathbf{x})$ and $f_b(\mathbf{x})$ be the PDFs for signal and backround respectively. According to the Neyman–Pearson lemma [102], the likelihood ratio

$$y(\mathbf{x}) = \frac{f_s(\mathbf{x})}{f_s(\mathbf{x}) + f_b(\mathbf{x})} \tag{4.9}$$

is the optimal estimator. It is limited to he interval $[0, 1]$ and signal hits have a likelihood ratio close to one, while background hits have a y close to zero. A cut on the likelihood ratio, i.e. rejecting all hits with y lower than a treshold, results in background suppression.

However, the exact PDFs are almost never known. Therefore, certain techniques for the approximation of the signal and background PDFs need to be applied. One possibility is to use Artificial Neural Networks (ANNs) [103].

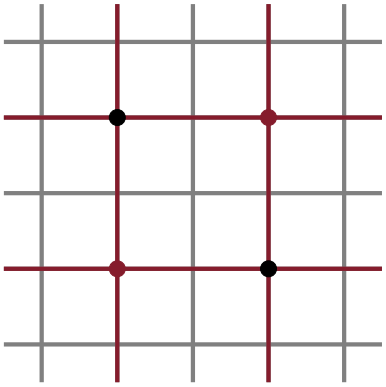

Figure 4.5: Ghost hits. The red dots are true hits, causing the red strips to fire (other strips are colored gray). Due to the ambiguity of the strip-strip assignments, the ghost hits are created (black dots).

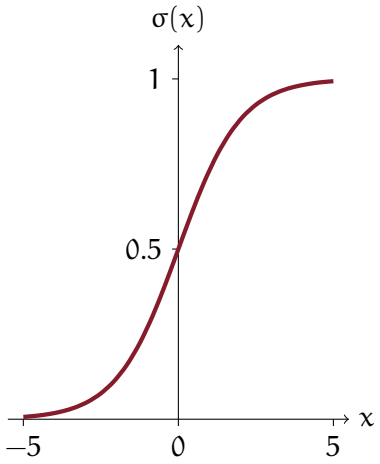

Figure 4.6: The sigmoid function $\sigma(x) = 1/(1+e^{-x})$. It maps the real numbers to the interval $(0,1)$. At $x = 0$ it shows linear behaviour, while for a large absolute value it approaches the value 0 ($x \ll 0$) or 1 ($x \gg 0$).

4.6.1 The Neuron

The basic building block of an ANN is the neuron (also called node). It receives an arbitrary number of inputs and maps them to one output. This is done in two steps. First the inputs are combined into one real number by the "synapse function", which is for example a simple sum of the inputs. This real number is then fed to an activation function. Often, the activation function is the sigmoid function $\sigma : \mathbb{R} \to (0,1)$ defined by

$$\sigma(x) = \frac{1}{1+e^{-x}} \quad . \tag{4.10}$$

For values close to zero it has a linear behavior, while for large positive values it approaches 1 and for large negative values it approaches 0. It is strictly monotonically increasing in $\mathbb{R}$. The sigmoid function is plotted in Figure 4.6.

A general ANN consists of several neurons, that are arbitrary connected, i.e. a neuron receives the outputs of many other neurons and gives its output to other neurons. Before a neuron receives the output of another neuron, this output is multiplied by a weight. Usually an ANN has input neurons, that receive the input to the whole network and also output neurons, that holds the output of the network. An ANN is then characterized by the connections between the neurons and the weights [103, 104].

4.6.2 *The Multi Layer Perceptron*

A special type of ANN is the Multi Layer Perceptron (MLP) [103, 104]. It is structured in layers, such that each neuron of a layer gets its input only from the neurons of the previous layer and passes its output only to the next layer. This gives the MLP a direction, in which information flows and it is sometimes refered to as a feed forward MLP. The layers, that are neither the input, nor the output layer, are called hidden layer. Every layer exept for the output layer contains a so-called "bias node". It always holds the value 1, which is then multiplied by a weight. The structure of an MLP is illustrated in Figure 4.7.

Training

An MLP with one output node can approximate the likelihood ratio, Equation (4.9). This can be achieved by a "supervised learning" method, which requires a set of training data, for its entries it is individually known, wether they are signal or background. Accordingly,each training hit is associated with a target, the desired output of the MLP. Background hits are asigned to 0, while signal hits have the target 1. The procedure of network training is the minimization of the error function

$$E(\boldsymbol{x_1}, \ldots, \boldsymbol{x_N}|\boldsymbol{w}) = \sum_{i=1}^{N} \frac{1}{2} \left(y_{MLP}(\boldsymbol{x_i}) - \hat{y}_i\right)^2 \tag{4.11}$$

$$\tag{4.12}$$

with respect to the weights $\boldsymbol{w}$, where $\hat{y}_i$ is the target of the i^{th} hit and N is the size of the training sample. One possibility to minimize the error function is to apply the method of "steepest" or "gradient

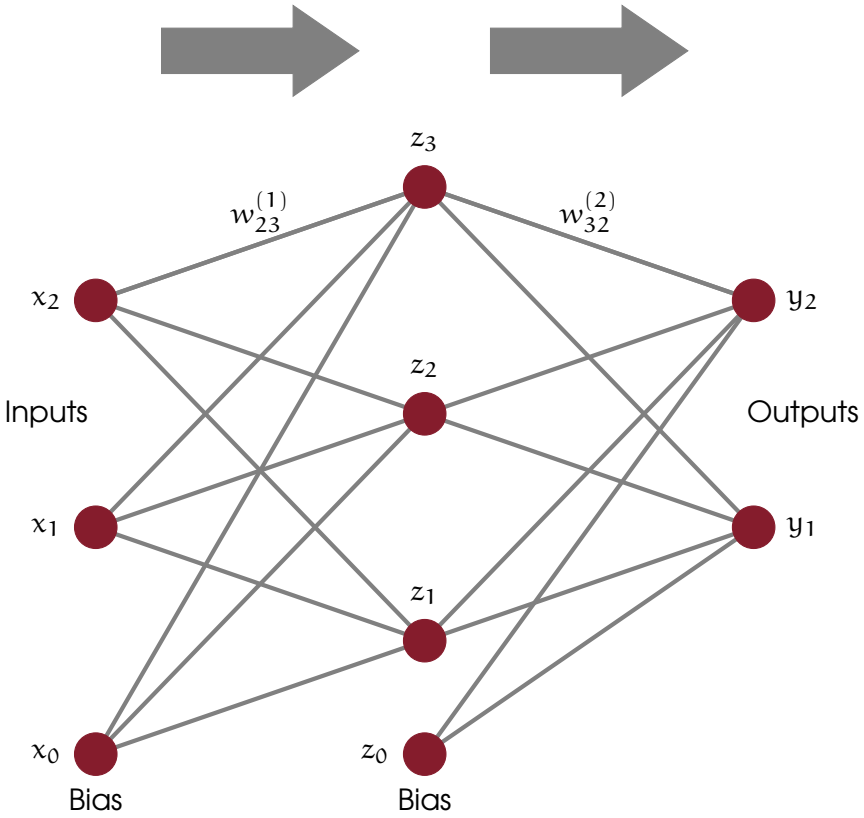

Figure 4.7: Structure of a Multi Layer Perceptron, according to [103]. It has two inputs and two outputs with an intermediate hidden layer. For clarity, only the connections between the input x_2 and the neuron z_3 and between z_3 and y_2 is labeled with the weight. The arrows indicate the direction of information flow.

descent": The network is initialized with random weights $\boldsymbol{w}$ being updated iteratively via

$$\boldsymbol{w}^{(\rho+1)} = \boldsymbol{w}^{(\rho)} - \eta \nabla_{\boldsymbol{w}} E \quad , \tag{4.13}$$

where ρ numbers the iteration. This method shifts the network in weight space in the direction of steepest descent. The positive number η is called learning rate [103, 104].

Overtraining

The training of a complex ANN can lead to "overtraining": Due to the limited size of the training sample, it is affected by statistical fluctuations, which can be learned by the network. This is of course not desired, because a different set of hits fluctuates diferently and the signal hits may not be recognized. Therefore, the available training hits are split into a training and a test sample. The error function (4.11) is then minimized for the training sample and the test sample is used as a check. A large difference between the error function of the test and the training sample indicates overtraining. Therefore, sufficient large training and test samples should be used, which leads to smaller statistical fluctuations.

A convenient way to construct, train, test, and apply MLPs is the TMVA toolkit [104] being integrated into the ROOT framework [86].

4.6.3 *Preprocessing*

Sometimes, the transformation of the input variables before feeding them to an ANN is advandatgeous. A very simple transformation is the normalization, whereby the variables are scaled and shifted, such that they lie between -1 and 1. This makes the inputs to be in the same order of magnitude, thus more comparable.

Decorrelation

Although the linear correlations among the components of an input vector can be learned by a network, they can be eliminated prior to feeding them to the network. This saves the "capacitance" of the network for learning the higher order correlations. The correlation is closely related to the covariance matrix, its diagonal elements are the variances of the components of the vector, while the correlation

of two different components is proportional to the off-diagonal elements.

The covaraince matrix Σ of N measurements of a vector $\mathbf{x} \in \mathbb{R}^n$ can be defined by

$$\Sigma = \frac{1}{N-1} \sum_{i=1}^{N} (\mathbf{x}_i - \overline{\mathbf{x}})(\mathbf{x}_i - \overline{\mathbf{x}})^T \quad , \tag{4.14}$$

where $\overline{\mathbf{x}}$ is the mean of $\mathbf{x}_i$ [103]. This matrix is by definition symmetric and positive semidefinite implying the existence of a diagonalization transformation

$$\Sigma \to \tilde{\Sigma} = S^T \Sigma S \quad , \tag{4.15}$$

with $\tilde{\Sigma}$ being diagonal with non-negative elements and S being symmetric. The matrix S is also used to define a matrix

$$\Sigma' = S\sqrt{\tilde{\Sigma}}S^T \quad , \tag{4.16}$$

with $\sqrt{\tilde{\Sigma}}$ being the diagonal matrix, its elements are the square root of the elements of $\tilde{\Sigma}$. It has the property $\Sigma'\Sigma' = \Sigma$. Transforming the vectors according to

$$\mathbf{x} \to \mathbf{x}' = (\Sigma')^{-1}\mathbf{x} \tag{4.17}$$

yields vectors $\mathbf{x}'$ with vanishing correlation among its components and the variances of the components are unity, i.e. this transformation decorrelates the input vectors [104].

Gaussianization

The decorrelation described above is only perfect for Gaussian distributed variables. Thus, the transformation of the input variables into Gaussian distributed variables is usefull. Only one of the signal or background classes can be transformed into a proper Gaussian distribution. Hence, it must be decided for one of them.

The transformation into a Gaussian distributed variable is done by applying the inverse error function with mean 0 and variance 1 to the cummulative distribution function to each component x_i of the

input vector $\mathbf{x}$. Denoting the PDF of x_i with f_i, the transformation prescription reads [104]

$$x_i \to x_i' = \sqrt{2} \cdot \mathrm{erf}^{-1}\left(2 \cdot \int_{-\infty}^{x_i} f_i(\xi)\,\mathrm{d}\xi - 1\right) \quad . \tag{4.18}$$

Depending on the choice of f_i being either the signal or the background PDF, one of these two event classes is Gaussian distributed with a mean of 0 and a variance of 1. In contrast to the n dimensional PDFs mentioned earlier, the one dimensional PDFs f_i are easy to obtain by a simple binning method or a spline fit.

4.6.4 Hopfield Networks

A Hopfield network is a more general ANN, in which every neuron is connected to each other neuron [105]. Hence, a direction of information flow cannot be assigned requiring the evaluation of the network state in an asynchronous manner. In a randomized order, the output of each neuron is individually computed, until the outputs of all neurons no longer changes.

4.7 Tracking at Belle II

The Belle II track reconstruction makes use of different kinds of track finding and track fitting techniques.

4.7.1 Track Finding

The VXD Track Finder (VXDTF) is based on a Cellular Automaton using the SVD data. In order to reduce the number of hit-hit combinations, the concept of sector maps is introduced. The sector maps are lookup tables dividing the sonsors in (overlapping) sectors. Only hits in compatible sectors are combined. After the track candidates are found, a Hopfield network finds the best subset of compatible tracks [99, 100, 106].

The CDC Legendre Track Finder (CDCLegendre) first maps the hits in the axial superlayers onto the conformal plane and then applies a Legendre Transformation, which in this context is very similar to the Hough Transform [107]. Afterwards, the hits in the stereo layers are used for the 3D reconstruction [108].

The CDC Local Track Finder (CDCLocal) is used in combination with the Legendre Track Finder. It is implemented as a Cellular Automaton [109, 110].

The above mentioned track finders are implemented as modules of BASF2 (c.f. Section 3.2.12). They are used for the online full reconstruction on the HLT as well as for the offline reconstruction [111].

The DATCON Tracking (c.f. Section 3.2.11) uses the conformal mapping followed by a fast Hough transform (c.f. Section 4.3.1), using the IP as the reference point. It uses only the information provided by the SVD and runs on an FPGA based platform, in order to create ROIs for the PXD online data reduction [112, 113].

4.7.2 Track Fitting

The fitting of the tracks in Belle II is handled by an upgrade of the GENFIT framework [114, 115]. For the online reconstruction a Kalman filter is used, while a Deterministic Annealing Filter (DAF) [116] is employed for the offline processing and physics analysis [111, 117]. The DAF is an advancement of the Kalman Filter, which is very robust against outliers and has a high efficiency in identifying hits not belonging to the track. For alignment purposes the tracks are fit with the General Broken Lines (GBL) Algorithm [111, 118]. The GBL Algorithm is the global equivalent to the Kalman Filter.

Chapter 5

SIX LAYER TRACKING

5.1 The Concept

The success of the data reduction by the ONSEN system depends on a high efficiency of the track finders on the DATCON and the HLT. Thus, charged particles creating an insufficient number of hits for tracking in the SVD and the CDC will be lost, although they might have created a sufficient number of hits in the whole VXD.

Typically, this is relevant for the particles with low transverse momenta. They will curl back towards the beam line before creating a sufficient amount of hits in the SVD. In order to address this issue, there will be a "Cluster Rescue" system installed on the DHC [119]. The low momentum particles will deposite a large amount of energy in the PXD sensors, resulting in a high drain current of the pixels (c.f. Section 4.1.1). This is a property discriminating the relevant physics hits from the background hits. The Cluster Rescue is implemented as a neural network, analyzing the PXD clusters. Upon the decision, that a cluster should be stored, although it may not be located inside a ROI, it sets a flag in the data. Accordingly, the ONSEN passes it to the Eventbuilder 2. The most important input variable to the network is the seedcharge of the cluster. It is the highest charge of a single pixel from the cluster.

However, Reference [5] reports, that this mechanism might not recover PXD hits from higher momentum pions ($\approx 200\,\mathrm{MeV/c}$) originating from a secondary vertex. K^0_S mesons are reconstructed via the decay into two charged pions. Having an average lifetime of $2.68\,\mathrm{cm/c}$, the K^0_S mesons travel a certain distance before decaying [6]. Thus, its doughter pions originate from a displaced vertex, c.f. Figure 5.2. Since K^0_S mesons play a major role in the Belle II physics program, a high reconstruction efficiency of these pions is important. In this work, an online track finding algorithm is developed and evaluated, in order to prevent the PXD hits of these pions to be lost. This algorithm uses hits in the whole VXD, i.e. it uses the hits from the PXD as well as hits in the SVD.

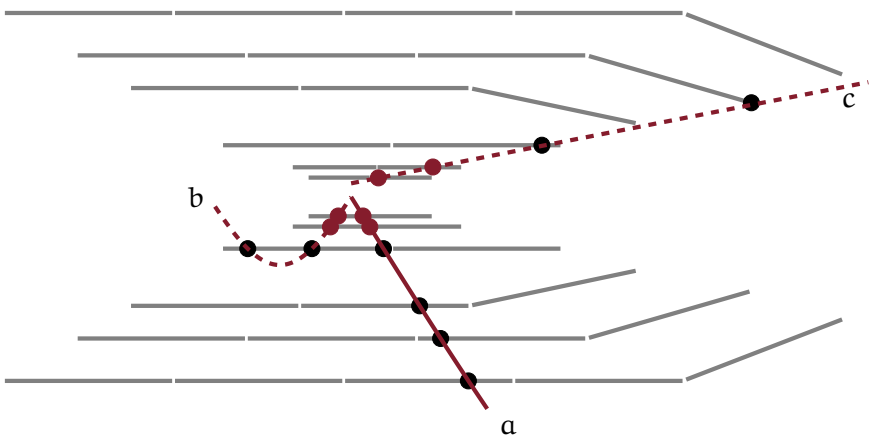

Figure 5.1: Tracks in the $x-z$ cross section of the VXD (scale 18 : 100). The black dots stand for hits in the SVD and the red dots are the PXD hits. In order to be trackable, a track needs to produce at least three hits. Thus, a track finder using only the SVD hits can only find track a. Track b has a very low momentum, so its PXD hits are probably found by the Cluster Rescue. Track c originates from a displaced vertex. Hence, it can leave the detector acceptance after the creation of some hits. Since it has a relatively large momentum, its PXD hits are very unlikely found by the Cluster Rescue. It would be found by a track finder, that uses all VXD hits.

In the next sections, the MC simulation procedure within the BASF2 framework is described and the additional gain from a six layer track finder is estimated. Afterwards, the algorithm of this track finder is described, which is evaluated in the subsequent section. The final section proposes the next steps towards an improved K^0_S detection.

5.2 Simulation

Monte Carlo simulations are required for the evaluation of a possible six layer track finder. The whole chain of simulation and data processing is done within BASF2. The physics events are generated using a BASF2 plugin of the event generator EvtGen [120]. The propagation of the particles through the detector is simulated with GEANT4 [121]. A further sequence of BASF2 modules provides the

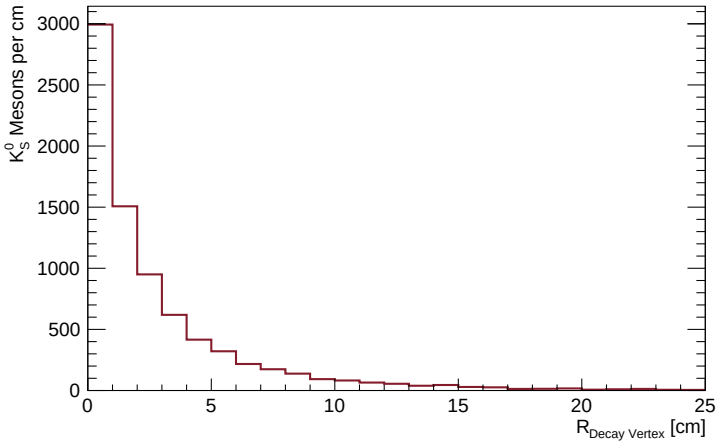

Figure 5.2: Distrubution of the decay vertices of K_S^0 mesons from a simulation of 10 000 $\Upsilon(4S)$ decays. Although many K_S^0 mesons decay outside the beam pipe ($R < 1.2\,\text{cm}$), and even the PXD volume ($R < 2.2\,\text{cm}$), most of them decay inside the SVD volume ($R < 14\,\text{cm}$).

relevant hit information. First the detectors response to the interaction with the particles is digitized. Afterwards, the output of the digitizer is used by the clusterizer searching for spatial clusters in the digits and computing some properties of the clusters. The positions of the clusters is now expressed in terms of the local coordinate system of the sensor. Furthermore, the clusters in the SVD are one-dimensional clusters representing the position of the fired strips. A spacepoint creator module, which is part of the VXD track finder, combines the SVD clusters on the p strips with the n clusters and transforms the resulting two-dimensional positions into the global Belle II coordinate system. The positions of the PXD clusters are also transformed into the global system. The resulting data is stored in ROOT files via a ROOT I/O module.

When necessary, the background contribution is included in the simulation. For the PXD and the VXD, the background from beam-gas scattering, Touschek effect, radiative Bhabha scattering, and from two photon QED processes is taken into account. For the CDC, the same background sources, except for the two photon QED contribution is included.

Table 5.1: Track categories sorted by the ability of the tracking systems to find them. The minimal number of hits required for being trackable is shown. The PXD hits, that are found by the Cluster Rescue mechanism are abbreviated as CR PXD.

	Number of Hits in			
Trackable by	PXD + SVD	CR PXD + SVD	SVD	CDC
CDCLegendre				$\geqslant 3$
CDCLocal				$\geqslant 3$
DATCON			$\geqslant 3$	
VXDTF Online			$\geqslant 3$	
VXDTF Offline		$\geqslant 3$		
6 Layer	$\geqslant 3$			
Only 6 Layer	$\geqslant 3$	< 3	< 3	< 3

5.3 Performance Estimation

A first estimation of a possible efficiency gain by the employment of an online six layer track finder can be done by simply counting the number of hits created by the particles in the detector. In order to reconstruct a track, at least three hits belonging to that track need to be available. Thus, every particle creating three or more hits can be regarded as trackable. The particles with less than three hits cannot be tracked.

For the DATCON as well as for the VXDTF the three hits need to be created in the SVD. The CDC track finders need the hits to be in the CDC. For the six layer tracking, the hits can be distributed over all six layers of the VXD. In the offline reconstruction, the VXDTF uses in addition to the SVD hits the hits in the PXD. Hence, a particle is VXDTF trackable if the sum of SVD hits and PXD hits found by the Cluster Rescue, is at least three. To be counted as "only six layer trackable", a particle needs to create at least three hits in the VXD, but less than three of them are allowed to be in the SVD. Furthermore, it must not be trackable by the CDC track finders. An overview of these conditions is given in Table 5.1.

Up to now, there is no BASF2 module emulating the Cluster Rescue. Thus, its response need to be approximated. When a cluster has a seed charge of more than 45 ADC counts, it is assumed to be found and if it is less, the cluster is regarded as not found [5].

Table 5.2: Pion tracks from a MC simulation with 10 000 $\Upsilon(4S)$ decays. The row denoted as "Trackable" contains all tracks being trackable by the existing tracking methods, whereas row "6 Layer" lists all tracks, that are exclusively trackable by an algorithm, which uses the whole VXD and thus representing an estimation of the additional gain by such an algorithm. Additionally to the plain numbers, the fraction is stated. The values not in braces are normalized to all tracks, while the embraced values are normalized to the trackable tracks. Only pions with a vertex inside the VXD volume are taken into account.

	Number of $\pi^{\pm}$ Tracks					
	All			Only from K_S^0		
All	41997	100 %		10711	100 %	
Trackable	37782	90.65 %	(100 %)	9794	91.44 %	(100 %)
6 Layer	330	0.85 %	(0.94 %)	66	0.62 %	(0.67 %)

A MC simulation of 10 000 events with $\Upsilon(4S)$ mesons decaying according to the known decay chains listed by the PDG [6] yields the numbers of $\pi^{\pm}$ tracks shown in Table 5.2. Since the Belle II detector will collect data at a center of mass energy adjusted to this resonance, this simulation represents the expected events at Belle II. Only tracks having its origin inside the VXD volume are counted, since the other pions are most likely products from secondary interactions with the detector material. As illustrated in Figure 5.2, most of the pions from K_S^0 decays originate inside this volume. However, only pions decaying inside the PXD will create hits in it. The transverse momentum distributions are shown in Figure 5.3.

More important than the reconstruction efficiency of charged pion tracks is the efficency of the reconstruction of K_S^0 mesons from these tracks. A K_S^0 meson counts as reconstructed, when both its doughter pions are found. This implies, that a K_S^0 is only reconstructed by the existing track finders, if both pions are found using the existing algorithms. In contrast to this, the gain of a six layer tracking is represented by the K_S^0 mesons, with at least one pion, that can be exclusively reconstructed by the six layer tracking. The other pion can also be reconstructed via the other track finders. The momentum spectrum of the K_S^0 mesons are shown in Figure 5.4. The numbers are listed in Table 5.3.

Table 5.3: Numbers of K_S^0 mesons from a simulation of 10 000 $\Upsilon(4S)$ decays. The fractions are normalized to all K_S^0 mesons and to the trackable ones (values in braces).

	Number of K_S^0 mesons		
All	6889	100 %	
Trackable	4622	67.09 %	(100 %)
6 Layer	57	0.83 %	(1.23 %)

However, these numbers will alter, once the efficiencies of the track finders are taken into account, as illustrated by the following example. Consider 100 tracks being trackable by the existing track finders and 1 track exclusively trackable by the six layer algorithm (1 % of the other trackable ones). Furthermore, assume independent efficiencies of 95 % and 50 % for the existing track finders and the six layer algorithm, repectively. Thus, 95 tracks are found by the existing track finders. The remaining 5 tracks are very likely still trackable by the six layer algorithm, resulting in 6 tracks not yet found, but trackable by the six layer track finder, from which 3 are found. Hence, $\approx 3\,\%$ more tracks can be recognized, compared to the already found tracks, resulting in an expected efficiency gain within the order of a few percent.

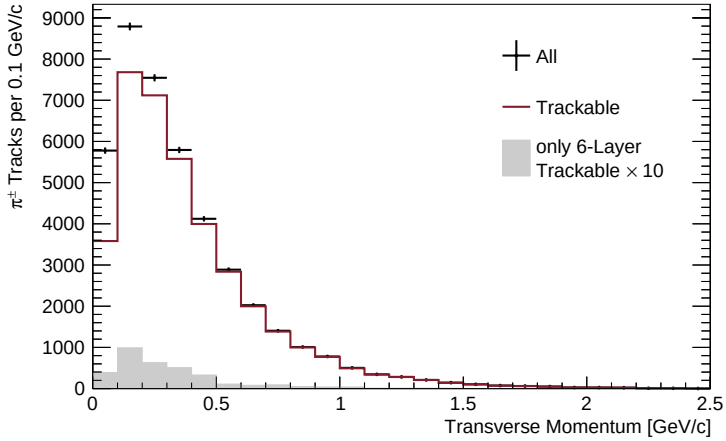

(a)

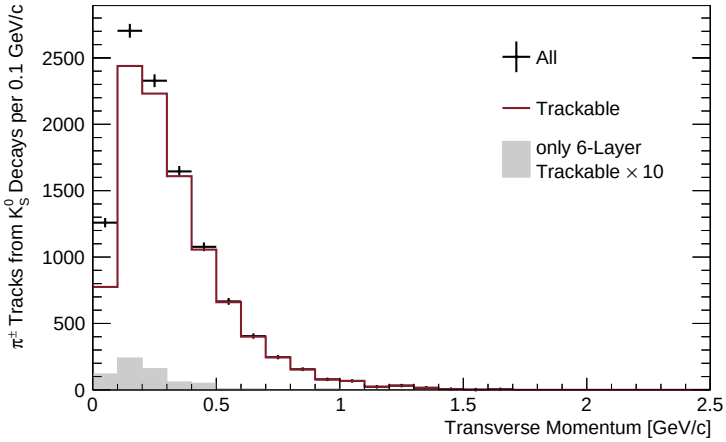

(b)

Figure 5.3: Transverse momentum of charged pions from a MC simulation of 10 000 $\Upsilon(4S)$ decays. Only tracks with its vertex inside the PXD volume are counted. The black markers represent all tracks, while the tracks trackable by the existing algorithms are described by the red line. The gray area is the tenfold amount of the tracks that are only six layer trackable. ***(a)*** All pions, and ***(b)*** only pions from K^0_S decays.

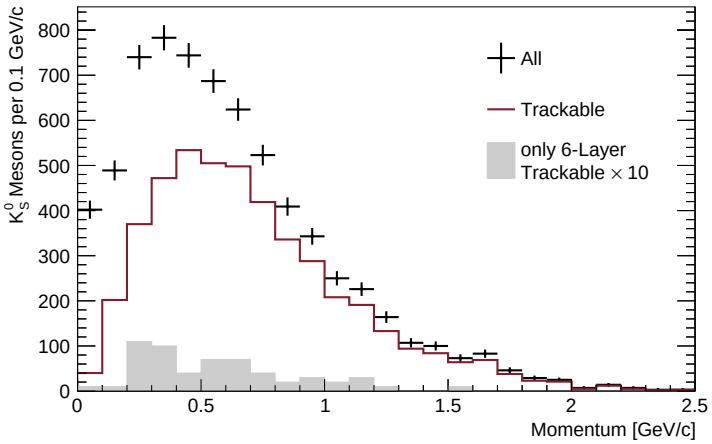

Figure 5.4: Momentum spectrum of K^0_S mesons from a MC simulation of 10 000 $\Upsilon(4S)$ decays. The black markers stand for all K^0_S mesons, while the red line represents the ones, that can be reconstructed by the existing track finders and the gray area is the tenfold magnified amount of K^0_S mesons, that can only be reconstructed, when additionally a six layer algorithm is used.

5.4 The Six Layer Algorithm

The raw PXD data is only available, until it reaches the ONSEN system. Thus, the six layer tracking system needs to be close to or even integrated into the ONSEN. This requires the algorithm to be able to run on an FPGA based platform. The DATCON demonstrates the successfull implementation of a fast Hough transform on FPGA hardware. Thus, the approach of a fast Hough transform is adopted by the six layer tracking. The background level is reduced by filters of the MLP type, that analizes the cluster properties together with the global coordinates. The Cluster Rescue shows, that this is possible on FPGAs.

The issue of the secondary vertex is treated by choosing the clusters itself as reference point for the conformal mapping. This constrains the track to pass through the cluster, which is reasonable. A drawback is, that the conformal mapping with the subsequent Hough transform has to be done for every hit, that serve as the reference point, but it offers a possibility to further reduce the background: When choosing the reference point, only clusters are included fitting to the reference point. For example, a hit, which is at the opposite side of the detector is very unlikely a part of the same track. This second stage of filtering is also done by an MLP. It is not necessary, that every hit is used as reference point. It is sufficient, to use only the hits of the third layer as reference point. A track, that reaches layer 3, creates sufficient hits, to be trackable, and the third layer is the SVD layer closest to the PXD. Choosing a PXD layer to provide the reference hits is not feasable due to its high occupancy.

A sketch of the algorithm is shown in Figure 5.5.

5.4.1 Hough Transform

The first step of the algorithm is a conformal mapping of the hits onto the $x' - y'$ plane with the hits of one layer serving as the reference point. Afterwards, a fast Hough transform is employed in order to identify the straight lines in the conformal plane, which are then circles in the real $x - y$ plane. When using a hit in one of the detector layers as the reference point, the Hough transform very often finds circles, that reflect the detector structure rather than a charged particle track, because the layers are arranged in an approximate circle and there are of course many hits in the same layer.

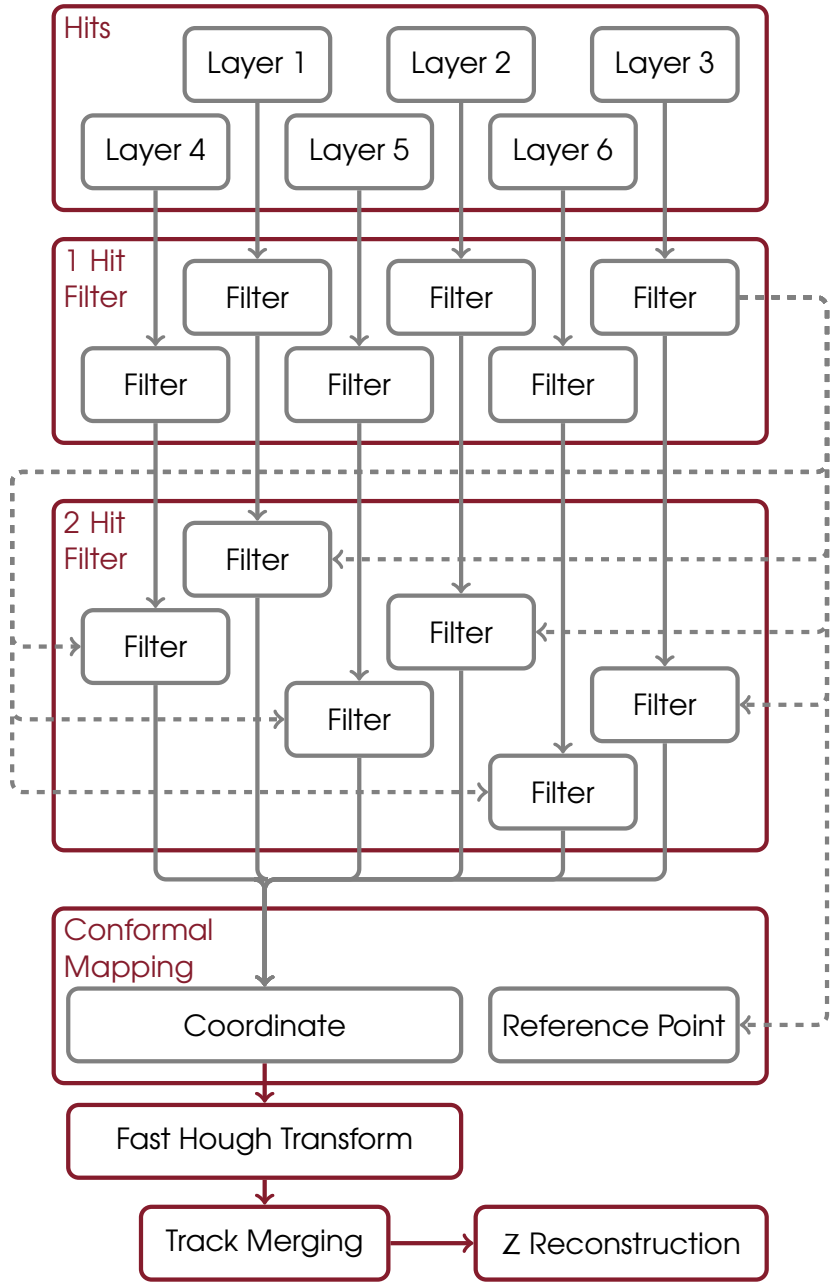

Figure 5.5: Data flow of the six layer algorithm. Gray arrows represent hits. The dashed ones are hits being used as reference point in the conformal mapping. The red arrows are track candidates.

This issue is tackled by a slight change of the fast Hough transform. The classical algorithm only checks, wether the number of hits exceeds a threshold. Here, this condition is replaced by the requirement of having a certain number of hits from different layers. This naturally preferes circles, that cross the layers and represent more likely relevant physics tracks, c.f. Figure 5.6. Furthermore, it is required, that at least one of the hits is located in the PXD. Tracks without a PXD hit would not serve the purpose of identifying important PXD hits.

Due to the relation between the transverse momentum p_t and the radius of the helix R

$$R = \frac{p_t}{q \cdot B} \quad , \tag{5.1}$$

where q is the absolute value of the charge of the particle ($q = e$ for carged pions and most other charged particles created in particle collisions) and B being the magnetic field along the z axis ($B = 1.5\,T$ at Belle II), the Hough transform can be limited to the range of $r' = (2R)^{-1}$. The simulation of 10 000 $\Upsilon(4S)$ events shows, that the transverse momentum of pions from K^0_S decays, which are only trackable by the six layer track finder, is in the range of $49\,MeV/c < p_t < 930\,MeV/c$, which corresponds to $10.8\,cm < R < 206.8\,cm$ and thus $2.4 \times 10^{-3}\,cm^{-1} < r' < 45.9 \times 10^{-3}\,cm^{-1}$.

After the iteration of the fast Hough transform, it is possible, that a track is found multiple times, especially, when its hits do not align on a perfect helix. The parameters of these multiple track candidates are very close to each other. Hence, they can be merged into one track candidate by combining the track candidates, that are close to each other in parameter space.

5.4.2 *Reconstruction of the Z Component*

The Hough transform delivers a track candidate consisting of a collection of hits and the parameters r' and ϑ. Using the relation $R = (2r')^{-1}$ together with the coordinates of the reference point $(\tilde{x}, \tilde{y}, \tilde{z})$ and the helix parameterization of Equation (4.6), the only yet undetermined parameter is h. The reconstruction in the z direction, i.e. the determination of h is now used to remove hits from the track candidate, which are not on the same helix as most of the hits. When not sufficient hits are left, the track candidate is considered as a fake track and discarded.

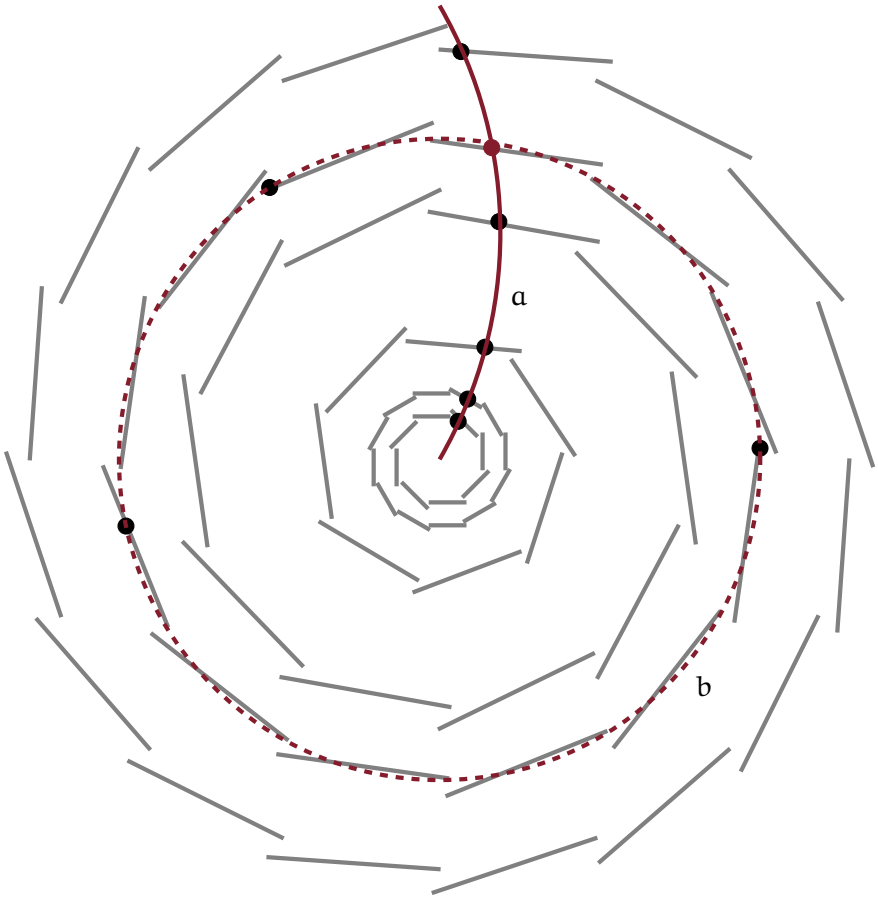

Figure 5.6: Track candidates in the VXD – $x-y$ cross section on a scale of $4:10$. The two inner layers are the PXD and the four outer layers are the SVD. The slanted parts of layer $4-6$ are not drawn. The dots represent hits, from which the red dot is used as the reference hit. When only the number of hits is counted during the Hough transform, two track candidates through the reference hit are found, but only the solid one is the true track. The dashed curve (b) is a fake track, which mirrors the detector structure. When the number of hits from different layers is counted in the Hough transform, the dashed fake track is not found, but the solid true track (a), which has the expected inside–outside orientation.

Due to the periodicity of the sine and cosine terms in the helix parameterization, there are many possible values for h. In fact, for a track candidate containing hits with distinct z coordinates, there are mathematically infinite possible solutions for h, but only one of them is true, as illustrated in Figure 5.7. This ambiguity is resolved in the following considerations.

In most cases, the true helix is the one with the largest pitch, because a particle moving along a helix with a smaller pitch would have passed the detector layers multiple times and thus created additional hits. The ansatz is the calculation of the largest possible h for every hit. Afterwards, the hits with a similar pitch are identified. When the number of hits with close h parameters exceeds a threshold, these hits stay related to the track candidate. The other hits are discarded. Accordingly, the mean value of the pitch is assigned to the track candidate.

A very low momentum curling track is only partly reconstructed, because the largest possible pitch is only for hits close to the reference point the true one. However, this is not a problem, because a curling track passes the layer, which is chosen to contain the reference hits, multiple times. Hence, these tracks will be found by the Hough transform more than once and with different reference points. During the z reconstruction, each hit is assigned to the true pitch in one of the track candidates and thus the different parts of the track are reconstructed as individual track candidates. It is sufficient, to merge these track parts in the offline track reconstruction. In the following, the reconstruction of the largest possible pitch is described

Having a hit at (x, y, z), it follows from Equation 4.6,

$$t + \vartheta = \arccos\left(\frac{\tilde{x} - x}{R} + \cos\vartheta\right) \quad \text{, and} \tag{5.2}$$

$$t + \vartheta = \arcsin\left(\frac{\tilde{y} - y}{R} + \sin\vartheta\right) \quad \text{, with} \tag{5.3}$$

$$h = \frac{z - \tilde{z}}{t} \quad , \tag{5.4}$$

which holds only for $t + \vartheta$ being in the intervals $[0, \pi]$ and $[-\pi/2, \pi/2]$, respectively, due to the output limits of the arccosine and arcsine functions. A larger interval yields the atan2 function. It takes two arguments (x, y) and $\mathrm{atan2}(y, x)$ returns the angle between

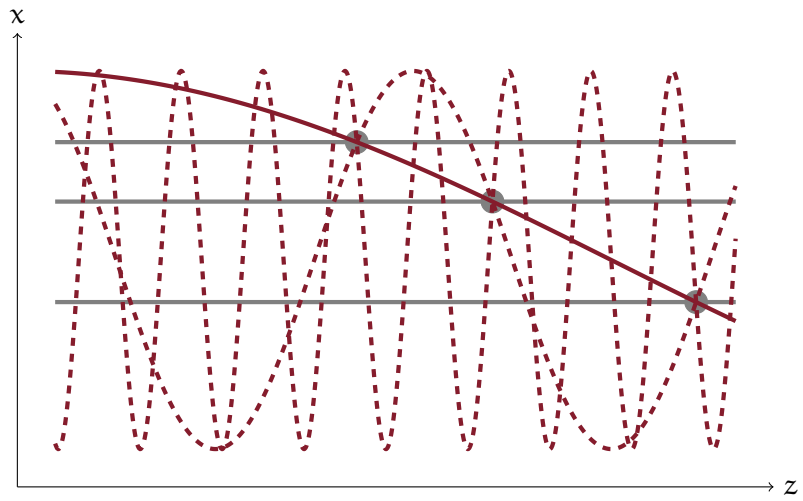

Figure 5.7: Projection of helices onto the $x-z$ plane. The gray dots mark the hits, that have to lie on a helix, its pitch assignment has infinite solutions. The solid line represents the true helix, whereas the dashed lines are other helices, that go through the hits. The fake helices have a smaller pitch than the true one and would have created additional hits, where they cross the detector layers (gray lines).

the x axis and the line from the origin to the point (x, y), which is in the interval $(-\pi, \pi]$. So Equations (5.2) and (5.3) can be combined to

$$t + \vartheta = \operatorname{atan2}\left(\frac{\tilde{y} - y}{R} + \sin\vartheta, \frac{\tilde{x} - x}{R} + \cos\vartheta\right) \quad . \tag{5.5}$$

The sum $t + \vartheta$ is now between $-\pi$ and π and t can be calculated by subtracting ϑ. Depending on the value of ϑ, t can be shifted out of the interval $(-\pi, \pi]$, that needs to be corrected for by adding or subtracting 2π. Accordingly, his t is the smallest possible t, which inserted into Eqation (5.4) yields the largest possible h.

5.4.3 *Background Reduction*

The minimization of the rate of fake tracks starts with the minimization of the amount of background. A simulation of 10 000 $\Upsilon(4S)$ decays yield the average hit numbers listed in Table 5.4.

Table 5.4: Number of hits per event in the VXD. They are averaged values of a simulation of 10 000 $\Upsilon(4S)$ decays. The column Signal represents all hits from particles involved in the $\Upsilon(4S)$ decay. Additionally, the fractions of the hits normalized to the total amount of hits are given.

Layer	Background	Signal	$\pi^{\pm}$	$\pi^{\pm}$ from K^0_S
1	6593	10.8	7.2	0.51
	99.84 %	0.16 %	0.11 %	0.0077 %
2	3512	11.2	7.3	0.63
	99.68 %	0.32 %	0.21 %	0.018 %
3	285	14.6	7.4	0.81
	95.11 %	4.89 %	2.46 %	0.27 %
4	94	15.3	7.9	1.02
	85.95 %	14.05 %	7.29 %	0.94 %
5	87	15.7	7.5	1.00
	84.63 %	15.37 %	7.39 %	0.97 %
6	87	16.6	7.9	1.06
	83.98 %	16.02 %	7.58 %	1.02 %

The reduction of background hits is done in two stages. At the first stage, the single hits are filtered by MLPs, one for each of the six layers. The network architecture sonsists of two hidden layers, the first one with $N + 1$ and the second one with N neurons, when N stands for the number of input varibles.

The MLPs for the SVD hits have 10 inputs: The position is described by the cylindrical coordinates z and R. Since an SVD hit is made from one n type cluster and one p type cluster, the hits are additionally described by the two charges of the clusters (cumulated charge of all strips), the two seed charges of the clusters (the charge of the strip with the highest charge), the two sizes of the clusters (number of strips that fired), and the two cluster times (time of the cration of the cluster).

The PXD clusters are also described by the coordinates z and R. Additionally, they are parameterized by the cluster charge, the seed charge, the cluster size, and the sizes in z and $r - \phi$ direction, which are fed to the MLPs for the PXD hits. Hence, the networks for the PXD hits have 7 inputs.

Table 5.5: Number of combinations of a hit with the reference hit per event in the VXD. They are averaged values from a simulation of 1000 $\Upsilon(4S)$ decays, after the single hit filters with a pion hit efficiency of 90 % are applied. The column Signal contains alls true hit-hit combinations of particles from the $\Upsilon(4S)$ decay. Additionally, the fractions of the according combinations to all combinations are shown.

Layer	Background	Signal	$\pi^{\pm}$	$\pi^{\pm}$ from K_S^0
1	57286.2	10.36	6.21	0.34
	99.98 %	0.02 %	0.01 %	0.001 %
2	28159.5	12.69	6.38	0.45
	99.95 %	0.05 %	0.02 %	0.002 %
3	416.054	22.3176	1.5174	0.2188
	94.91 %	5.09 %	0.35 %	0.05 %
4	111.794	13.344	7.7112	0.885
	89.34 %	10.66 %	6.16 %	0.71 %
5	77.2838	11.8662	7.2894	0.8236
	86.69 %	13.31 %	8.18 %	0.92 %
6	70.236	11.558	7.4376	0.8288
	85.87 %	14.13 %	9.09 %	1.01 %

All input variables are Gaussianized and decorrelated, before they are read by the MLPs. The networks are trained and tested with a sample of 5000 $\Upsilon(4S)$ events and the target to dicriminate between background hits and hits from charged pions. Due to the large amount of background hits in the PXD, their rate is scaled by a factor of 20.

The second stage filters are applied to the combination of a hit and the reference hit. After the application of the first stage filters with thresholds adjusted such that the $\pi^{\pm}$ hit efficiency is 90 %, which correpsonds to a background rejection of $\approx$ 95 % for the SVD hits and $\approx$ 60 % for the PXD hits, the numbers of combinations of a hit with a reference hit in the third layer are shown in Table 5.5.

Again, there is a dedicated MLP for hits of each layer. They have the same structure of two hidden layers with $N + 1$ and N nodes. The inputs are the output of the first filter for the hit as well as the reference hit. Additionally, it uses the difference of the z coordinates of the hit and the reference hit and the difference of the

ϕ coordinates. Furthermore, the cluster properties of the two hits are used. For the SVD hits, the charge, seed charge, and size of the n and p clusters is used. For the PXD hits, the charge, seed charge, the size, and the sizes in z and $r-\phi$ direction is used. This makes the MLP for a hit from the PXD and the reference hit (3^{rd} layer) to have 15 inputs and the MLPs for the combination of an SVD hit with the reference hit have 16 inputs. These MLPs are also trained with MC data of 5000 events. Again, the amount of background hits is scaled. Only hits are taken into account, that are accepted by the first filtering stage with the threshold adjusted, such that it has a signal efficiency of 90 %. Before they are read by the MLP, a Gaussianization and a decorrelation is performed.

Unfortunately, these filters rely on the accuracy of MC data, which is not in perfect agreement with true physics data. However, in the beginning of data taking including the PXD, the luminosity will be low, so that the ROIs can be dimensioned relatively large. They will contain a large amount of background data. Once this background data is available, it can be used in the training instead of the MC data, which will result in the overcoming of this drawback.

5.4.4 *Implementation*

In the final setup, the algorithm needs to be implemented on an FPGA platform. However, for development and evaluation it is much more convenient, to implement the algorithm as a C++ program, which is done in this work. Although it uses input created within BASF2, it is a standalone program independent from BASF2.

In this C++ program, the non-integer numbers are stored as floating point numbers, which is a commonly used format in C++. However, operations involving floating point numbers are very inefficient to realize on an FPGA. Nevertheless, the values of the variables used in this algorithm are limited to a certain range, which makes it possible to use fixed point numbers on the FPGA. Operations with fixed point numbers are almost identical to the corresponding operations with integers. Addition, subtraction, and multiplication of integers and fixed point numbers are very easily realized on an FPGA. Division, which is done during the conformal mapping and the z reconstruction, is more complicated, but can be iplemented as lookup tables. Whereas the division by 2, which is done in the iteration process of the fast Hough transform, is only a bit shift, which is very

easy to implement. The other functions, like sine, cosine, atan2, and the sigmoid function for the MLP, need to be described by lookup tables. The symmetry properties of them help to reduce the amount of rescources used in the FPGA.

The successfull implementation of the conformal mapping and the fast Hough transform on the DATCON and the implementation of the MLP of the Cluster Rescue on the DHC demonstrate the feasibility of these methods on FPGAs.

5.5 *Optimization*

The efficiency can be defined as the ratio of found true tracks to all true tracks. While this definition is important for physics analysis, the definition as the ratio of found true tracks to all trackable true tracks is used, to describe the quality of a track finder. Accordingly, the latter is used. Additionally, only pions originating inside the VXD volume are respected. A true track is considered as found, when at least three of its hits are associated to one track candidate. The other track candidates are fake tracks.

There are several parameters of the algorithm, that need to be tuned, in order to achieve a high performance, i.e. high efficiency of pion track reconstruction while keeping a low fake rate (fraction of fake tracks). The parameters are:

- the thresholds of the single hit filters. Lower thresholds increase the signal hit efficiency, while lowering the background rejection.
- the thresholds of the hit-hit combination filters. The effect is the same as of the single hit filter thresholds.
- the number of iterations during the Hough transfrom. A large number of iterations requires a track candidate to have well aligned hits, in order to be reconstructed. Thus, the tracking efficiency decreases. However, a low number of iterations leads to a higher fake rate and a (too) coarse resolution.
- the minimum number of hits, that needs to be exceeded in the Hough transform, to continue the iteration. Requiring more hits reduces the fake rate, while lowering the efficieny.

- the minimum number of hits associated to a track candidate in the z reconstruction. This number does not need to be the same as the threshold during the Hough transform.
- the allowed distance between different hits in h parameter space during the z reconstruction. Large values lead to a higher fake rate, but also to an increased efficiency, since the less well aligned tracks are recongnized.

In principle, an efficiency of 100 % can be achieved by accepting any combination of hits as a track candidate. Of course, this comes to the price of a huge fake rate. In practice, such a track finder is useless. Two parameter sets are determined, resulting in two possible setups of the track finder. The first setup is optimized for a high efficiency at a fake rate of $\approx$ 90%, while the second setup has a high efficiency at a fake rate of $\approx$ 50 %. The six layer tracking algorithm will only be used online, in order to rescue PXD hits outside the ROIs. Thus, the tolerable fake rate is only limited by the bandwidth. However, the ROIs created by the DATCON and the HLT will contain mostly background hits, especially since the DATCON tracking has a fake rate of $\approx$ 60 % [112]. Hence, the data rate created by the six layer tracking will be neglegibly small, even with a large fake rate.

The parameters as well as the efficiencies are shown in Table 5.6. The significant lower efficiency of the pion track reconstruction from K_S^0 decays compared to the efficiency for all pions is explained by the large amount of K_S^0 mesons decaying outside the PXD volume (c.f. Figure 5.2). They can not be reconstructed by the six layer algorithm requiring at least one PXD hit. The p_t dependence of the efficiencies is shown in Figure 5.8. The drop towards smaller transverse momenta is clearly visible. It is a typical behavior of track finders reflecting the multiple scattering at small momenta (c.f. Section 4.1.2).

Table 5.6: Parameters of the two working points of the six layer tracking algorithm. The thresholds of the filters are adjusted to result in the shown pion hit efficiencies. The Hough threshold represents the number of hits required to be found by the Hough transform additional to the reference hit. During the reconstruction of the z component of the track, the helix pitch h is calculated for each hit. The minimum number of hits refers to the required number of hits being close to each other in h space. The maximum allowed distance between two hits in h space is shown. Additionally, the efficiencies for pion track reconstruction and for the reconstruction of tracks of pions from a K^0_S decay are shown. Furthermore, the fake rate is listed. The efficiencies and the fake rates are obtained by the application of the algorithm to MC data simulating 10 000 $\Upsilon(4S)$ decays.

	Setup	
	1	2
Efficiencies First Filters	95 %	90 %
Efficiencies Second Filters	90 %	90 %
Hough Iterations	10	11
Hough Threshold	2	3
Minimum Number of Hits	3	4
Maximum Distance h	2 cm	1.5 cm
Efficiency	81.4 %	63.6 %
Efficiency K^0_S	56.7 %	33.3 %
Fake Rate	90.3 %	49.3 %

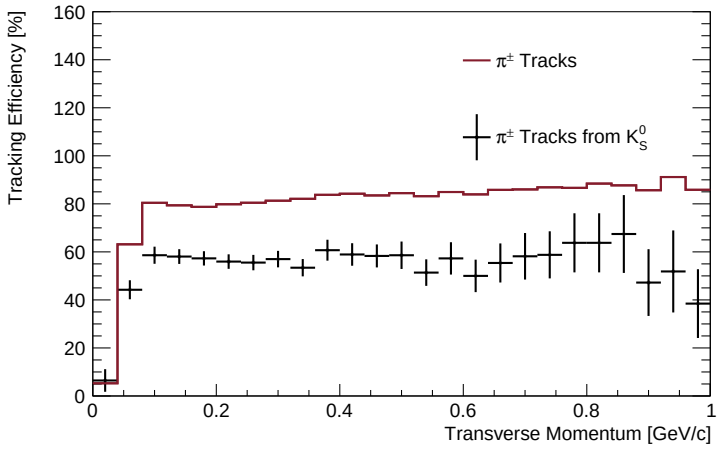

(a)

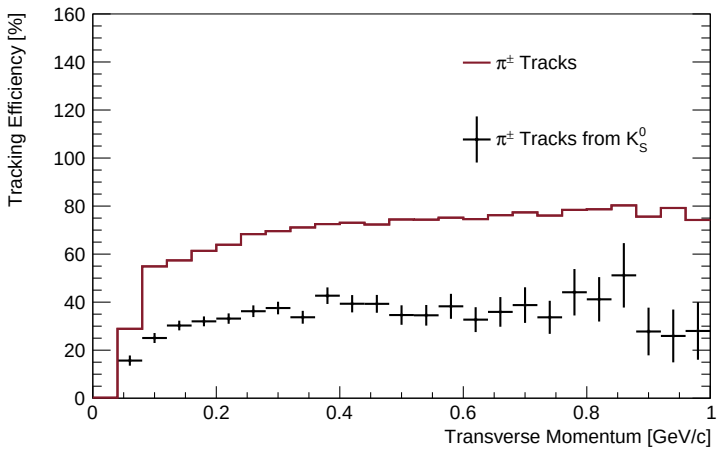

(b)

Figure 5.8: Efficiency of the six layer algorithm versus transverse momentum. ***(a)*** Setup with a fake rate of 90 % and ***(b)*** setup with a fake rate of 50 %.

5.6 Evaluation

In this section, the performance of the six layer tracking algorithm is compared to the existing track finders. Therfore, the MC data of 10 000 $\Upsilon(4S)$ decays is fed to the VXDTF as well as to the two CDC track finders. A BASF2 module emulating the DATCON is available, but lacks the required interface for the comparison with other track finders. Thus, the six layer tracking cannot be compared to the DATCON tracking. However, the performance of the DATCON is regared as inferior to the VXDTF. This is why only the VXDTF is used in the offline tracking and the comparison with the VXDTF should be sufficient. Again, the Cluster Rescue needs to be approximated by the threshold behavior described in Section 5.3.

A track is declared to be found, when the VXDTF or the CDC track finders recognize the track or the track has at least two PXD clusters found by the Cluster Rescue. Since the PXD has two layers, a track with only one rescued cluster has most liekly another PXD cluster, that has to be found. According to the definition in the previous section, the efficiency is normalized to all trackable tracks.

The performance of the six layer algorithm compared to the existing track finders is listed in Table 5.7. The numbers are in good agreement to the previous performance estimation. The gain of pion tracking efficiency by the employment of the six layer tracking depending on transverse momentum is shown in Figure 5.9. The efficiency gain is maximum at low p_t, where it reaches values of up to $\times 3$ the average efficiency gain.

The gain of K_S^0 reconstruction efficiency is plotted against momentum in Figure 5.10. A significant enhancement in a certain momentum region is not observable.

The requirement of two found pion tracks lowers the K_S^0 reconstruction efficiency of the existing track finders compared to the single pion efficiency. In contrast to this, an additional found K_S^0 requires only one pion solely found by the new algorithm, while the other pion can also be found by the other track finders. As a result, the efficiency gain for the K_S^0 reconstruction is larger compared to the efficiency gain for the single pions.

Table 5.7: Performance of the six layer algorithm in comparison with the existing track finders. The algorithms are applied to data from a simulation of 10 000 $\Upsilon(4S)$ decays. The number of found tracks as well as the efficiencies are shown. Furthermore, the gain of the employment of the six layer algorithm normalized to the tracks already found by the existing algorithms is shown. The six layer algorithm labeld 1 represents the setup with a fake rate of 90 %, whereas the label 2 stands for the setup with 50 %. A K_S^0 meson is regarded as reconstructed only by the six layer algorithm, if at least one doughter pion is exclusively found by the six layer tracking. The other pion is also allowed to be reconstructed by the existing tracking.

	$\pi^\pm$ tracks	$\pi^\pm$ tracks from K_S^0	K_S^0
Trackable	74939	9211	4147
Found	70746	8512	3572
6 Layer 1	60981	5219	
6 Layer 2	47667	3063	
Only 6 Layer 1	1693	212	177
Only 6 Layer 2	687	66	51
Efficiency Found	94.4 %	92.4 %	86.1 %
Efficiency 6 Layer 1	81.4 %	56.7 %	
Efficiency 6 Layer 2	63.6 %	33.3 %	
Gain by 6 Layer 1	2.4 %	2.5 %	5.0 %
Gain by 6 Layer 2	1.0 %	0.8 %	1.4 %

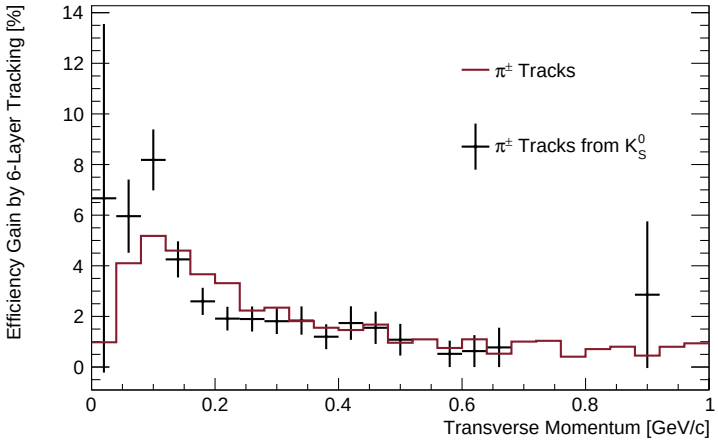

(a)

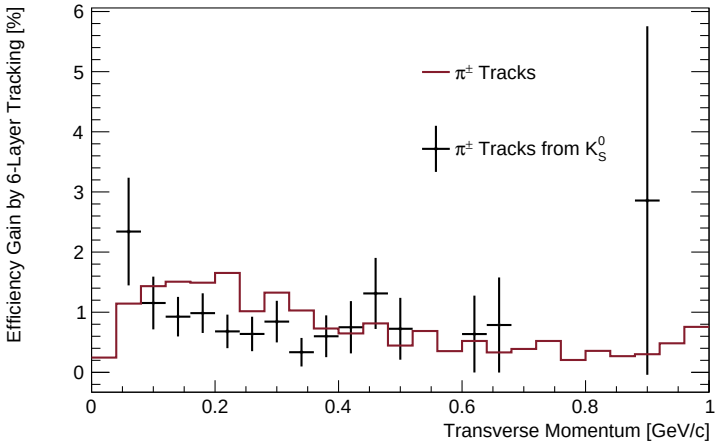

(b)

Figure 5.9: Pion reconstruction efficiency gain by the six layer algorithm versus transverse momentum obtained from a simulation of 10 000 $\Upsilon(4S)$ decays. ***(a)*** Setup with a fake rate of 90 % and ***(b)*** setup with 50 %.

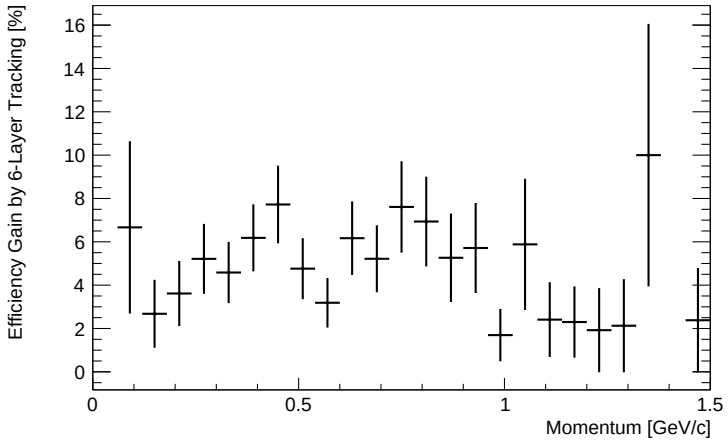

(a)

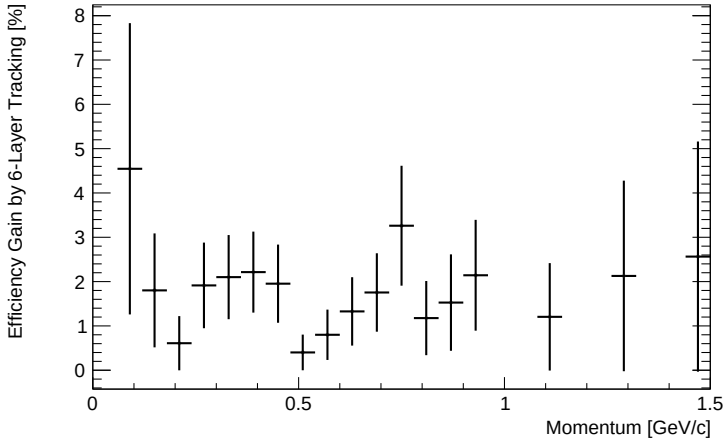

(b)

Figure 5.10: Gain of the reconstuction efficiency of K_S^0 mesons by the six layer algorithm versus momentum obtained from a simulation of 10 000 $\Upsilon(4S)$ decays. ***(a)*** Setup with a fake rate of 90 % and ***(b)*** setup 50 %.

5.6.1 Other Decays

The performance of the developed algorithm is also tested for dedicated decays:

1. $B^0 \to K^{0*}(\to K^0_S\pi^0)\gamma$. This penguin decay is sensitive to right-handed currents and therefore to physics beyond the SM, c.f. Section 2.2.1.

2. $B^0 \to \phi K^0_S$. This $b \to s\bar{s}s$ penguin decay is sensitive to the UT angle β. However, physics beyond the SM contributions allow the observed angle to differ from the angle obtained by the investigation of $B^0 \to J/\psi K^0_S$, c.f. Section 2.2.1.

For both decays, a MC sample of each 5000 events is generated and fed to the tracking algorithms. Tables 5.8 and 5.9 lists the efficiencies and the gain of the six layer algorithm. While keeping the same fake rate as for the general $\Upsilon(4S)$ decays (not shown in the tables), the efficiencies drop. This is probably caused by the higher momentum of the K^0_S mesons. They travel a longer distance before decay, increasing the probability to escape the PXD. Since the six layer algorithm requires a PXD hit, these tracks are not recognized by the algorithm. However, the efficiency gain of the K^0_S reconstruction is still $\gtrsim 1\,\%$.

5.6.2 Further Developments

The results reported in this work can only be understood as a first step towards an improved K^0_S detection at Belle II. The next steps would be a further optimization of the algorithm. For example, the filters could be trained with data from K^0_S doughter pion hits unrecognized by the existing track finders. This requires a larger amount of MC data, since only a fraction of hits are created such pions. Nontheless, this will improve the identification of the desired hits, resulting in an increased efficiency-fake rate ratio. An improvement concerning resources would be the adoption of the concept of sector maps used by the VXDTF (c.f. Section 4.7.1). With this method, only a fraction of hit-hit combinations would need to be evaluated by the second stage filter and thus saving resources.

Another important step would be the investigation, wether the offline track finders will be able to find the additional tracks. The physics analysis requires clean tracks with a good quality indicator

Table 5.8: Performance of the six layer algorithm for $B^0 \to K^{0*}(\to K^0_S\pi^0)\gamma$ obtained from a simulation of 5000 events. The meaning of the entries is identical to the entries in Table 5.7

	$\pi^\pm$ tracks	$\pi^\pm$ tracks from K^0_S	K^0_S
Trackable	24909	9988	3750
Found	23458	9342	3307
6 Layer 1	17856	5187	
6 Layer 2	13133	2857	
Only 6 Layer 1	495	166	111
Only 6 Layer 2	197	58	36
Efficiency Found	94.2 %	93.5 %	85.7 %
Efficiency 6 Layer 1	71.7 %	51.9 %	
Efficiency 6 Layer 2	52.7 %	28.6 %	
Gain by 6 Layer 1	2.1 %	1.8 %	3.4 %
Gain by 6 Layer 2	0.8 %	0.6 %	1.1 %

(e.g. χ^2) provided by the track fit. Usually, a cut on χ^2 is applied during the analysis. Thus, the six layer algorithm is only usefull, when the found track candidates result in a good fit.

Finally, the algorithm needs to be implemented on FPGAs. Therefore, the resource requirements need to be carried out (How many FPGAs are needed? Is it possible to integrate the algorithm into the ONSEN system? Can the Cluster Rescue be used as the first stage filter for the PXD hits? etc.).

Table 5.9: Performance of the six layer algorithm for $B^0 \to \phi K_S^0$ obtained from a simulation of 5000 events. The meaning of the entries is identical to the entries in Table 5.7.

	$\pi^\pm$ tracks	$\pi^\pm$ tracks from K_S^0	K_S^0
Trackable	24295	7541	2520
Found	22808	6982	2204
6 Layer 1	16571	3509	
6 Layer 2	12092	1785	
Only 6 Layer 1	487	140	78
Only 6 Layer 2	188	43	26
Efficiency Found	93.9 %	92.6 %	87.5 %
Efficiency 6 Layer 1	68.2 %	46.5 %	
Efficiency 6 Layer 2	49.8 %	23.7 %	
Gain by 6 Layer 1	2.1 %	2.0 %	3.5 %
Gain by 6 Layer 2	0.8 %	0.6 %	1.2 %

Chapter 6

CONCLUSION

In this work, an online track finding algorithm is designed and evaluated for the increase of the detection efficiency of K_S^0 mesons. Due to the requirement of integration into the readout path and data reduction system, the algorithm should be implemented on an FPGA based platform.

However, within the scope of this work, the algorithm is implemented as a C++ program for development, optimization, and evaluation. It is based on the fast Hough transform applied to the hits from all six layers of the vertex detectors mapped onto the conformal plane. The secondary vertices of the pions from K_S^0 decays do not permit the constraint to the primary vertex. Thus, the hits of the third layer are used as reference point of the conformal transformation.

The amount of fake tracks is reduced by a neural network filtering system organized in two stages. The first stage filters are applied to the hits. Using the coordinates together with the cluster information related to the hit, they discriminate between background hits and hits from charged pions. The second stage filters are applied to the combination of a hit and the reference hit before the conformal mapping takes place. They also use the coordinates as well as the cluster information from the hits.

Two parameter sets are determined, in order to run the algorithm at fake rates of 90 % and 50 %. For generic $\Upsilon(4S)$ decays, the resulting efficiencies for pion track reconstruction are 81.4 % and 63.6 %, respectively. Compared to the existing tracking systems, a gain of 5.0 % and 1.4 %, respectively, for the K_S^0 detection efficiency is observed. For dedicated decay channels of $B^0 \to K^{0*}(\to K_S^0\pi^0)\gamma$ and $B^0 \to \phi K_S^0$, the efficiency decreases. However, the resulting gain of K_S^0 detection efficiency is still in the order $\gtrsim 1\,\%$.

The next steps would be the investigation of the gain by the employment of the proposed six layer tracking for the offline analysis. Additionally, the algorithm needs to be implemented on an FPGA based platform. Therefore, the hardware requirements need to be evaluated.

Appendix A

PERFORMANCE OF THE MLPS

A.1 First Stage Filters – Single Hit Filter

On the following pages, the output distributions of the six MLPs of the first stage filters are shown (Figure A.1). The networks are trained with a sample of 5000 $\Upsilon(4S)$ decays from a simulation and the shown plots result from the application of the trained MLPs to data from a simulation of 10 000 $\Upsilon(4S)$ decays.

By placing a cut on this output, i.e. accepting only hits above a certain threshold, the amount of background hits is reduced, while increasing the signal to background ratio. Depending on the cut value, different $\pi^{\pm}$ hit efficiencies and background rejections are obtained. The $\pi^{\pm}$ hit efficiency is defined as the ratio of accepted pion hits to all pion hits. The background rejection is the probability, that a background hit is rejected, i.e. the ratio of rejected backround hits to all background hits. Figure A.2 shows the achievable background rejection plotted against the $\pi^{\pm}$ hit efficiency.

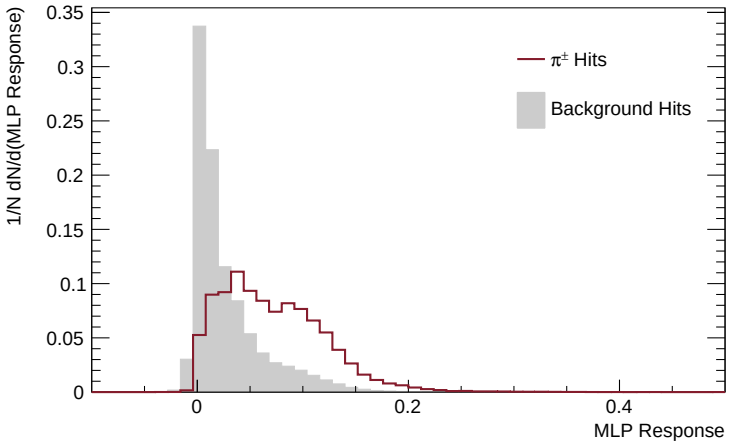

(a)

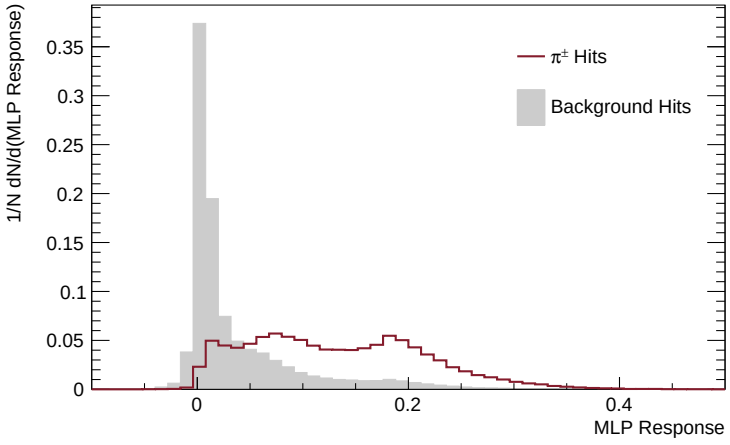

(b)

Figure A.1: Output distribution of the first stage filters for background (gray) and $\pi^{\pm}$ hits (red line). The values are obtained from data of a simulation of 10 000 $\Upsilon(4S)$ events fed to the networks. ***(a)*** Layer 1 and ***(b)*** layer 2.

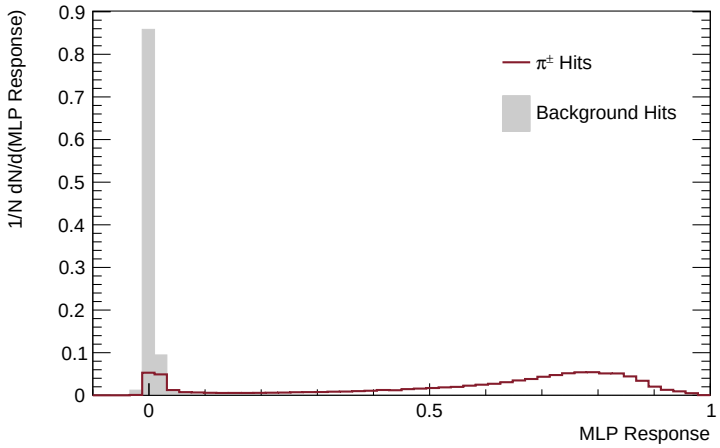

(c)

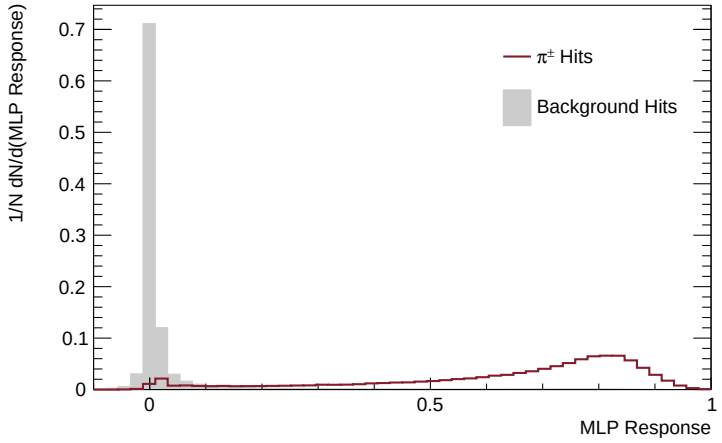

(d)

Figure A.1: Continued. ***(c)*** Layer 3 and ***(d)*** layer 4.

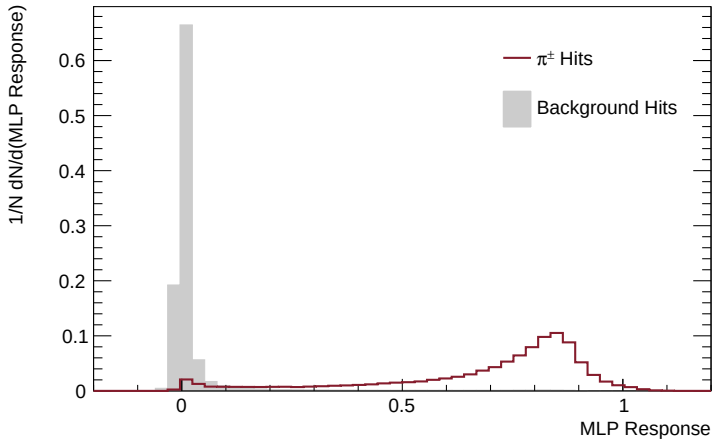

(e)

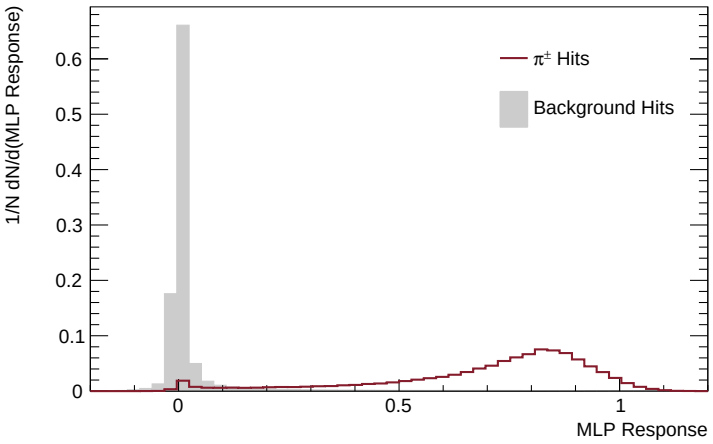

(f)

Figure A.1: Concluded. ***(e)*** Layer 5 and ***(f)*** layer 6.

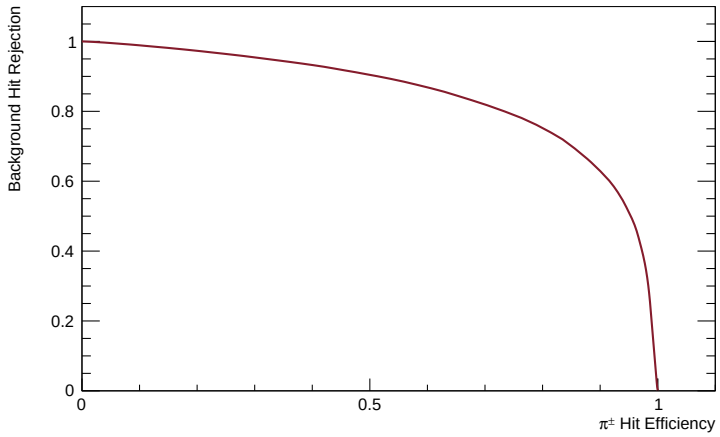

(a)

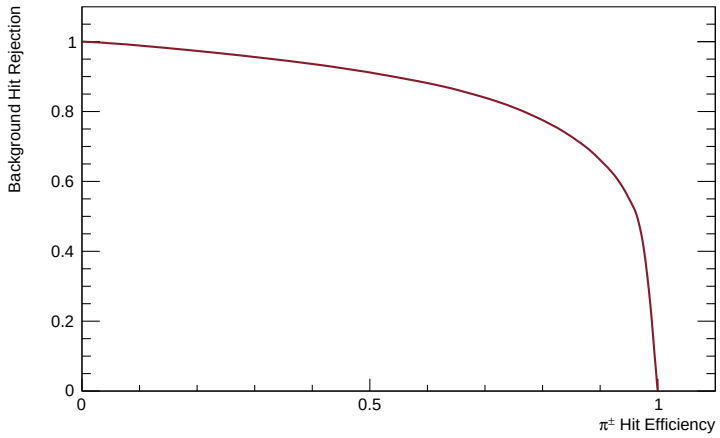

(b)

Figure A.2: Background rejection versus $\pi^{\pm}$ hit efficiency of the first stage filters. The values are obtained from data of a simulation of 10 000 $\Upsilon(4S)$ events fed to the networks. ***(a)*** Layer 1 and ***(b)*** layer 2.

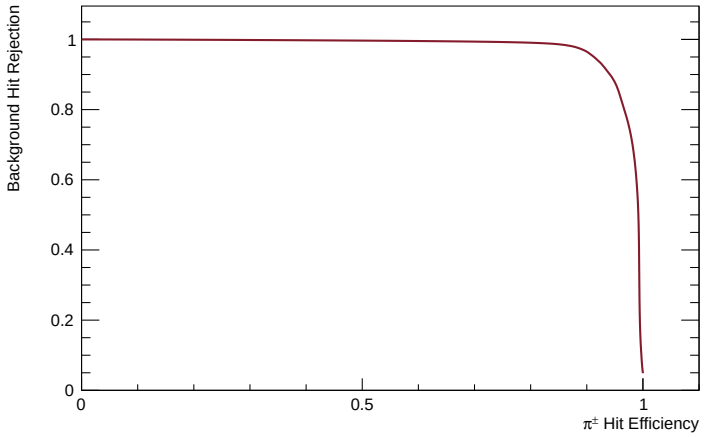

(c)

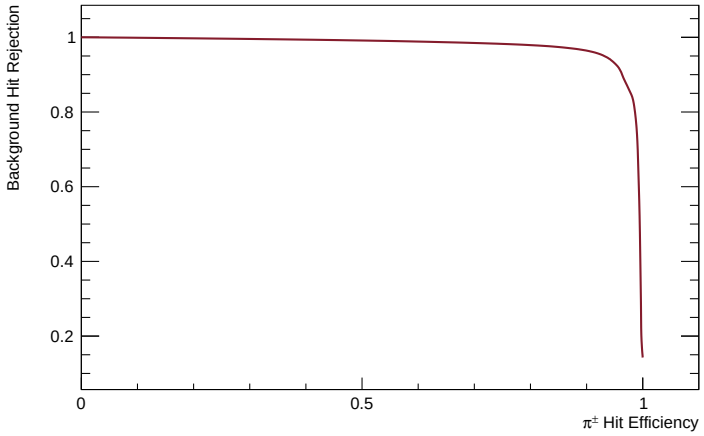

(d)

Figure A.2: Continued. ***(c)*** Layer 3 and ***(d)*** layer 4.

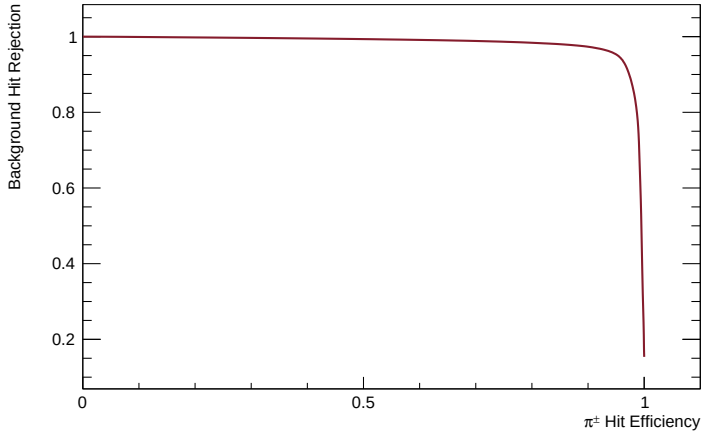

(e)

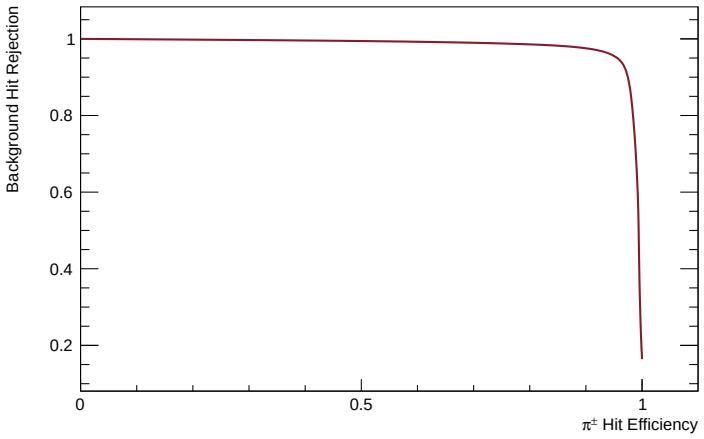

(f)

Figure A.2: Concluded. ***(e)*** Layer 5 and ***(f)*** layer 6.

A.2 Second Stage Filters – Double Hit Filter

On the following pages, the output distributions of the six MLPs of the second stage filters are shown (Figure A.3). The networks are trained with a sample of 5000 $\Upsilon(4S)$ decays from a simulation and the shown plots result from the application of the trained MLPs to data from another simulation of 5000 $\Upsilon(4S)$ decays.

By placing a cut on this output, i.e. accepting only hit-reference hit combinations above a certain threshold, the amount of background hits is reduced, while increasing the signal to background ratio. Depending on the cut value, different $\pi^{\pm}$ hit-reference hit efficiencies and background rejections are obtained. The $\pi^{\pm}$ hit-reference hit efficiency is defined as the ratio of accepted pion combinations to all pion combinations. The background rejection is the probability, that a background hit-reference hit combination is rejected, i.e. the ratio of rejected backround combinations to all background combinations. Figure A.4 shows the achievable background rejection plotted against the $\pi^{\pm}$ hit efficiency. The hits from layer 3 serve as reference hit.

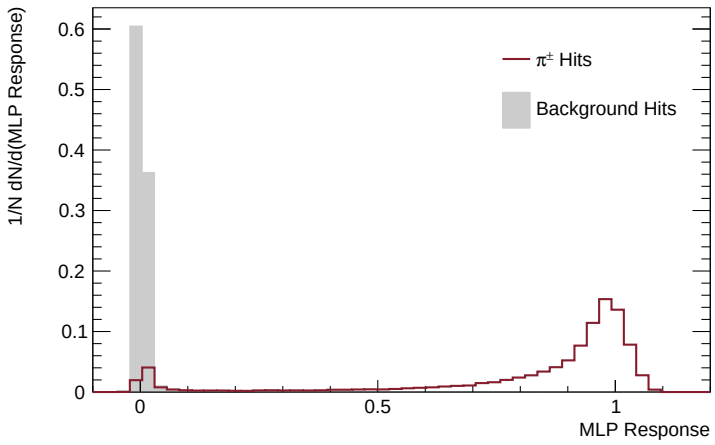

(a)

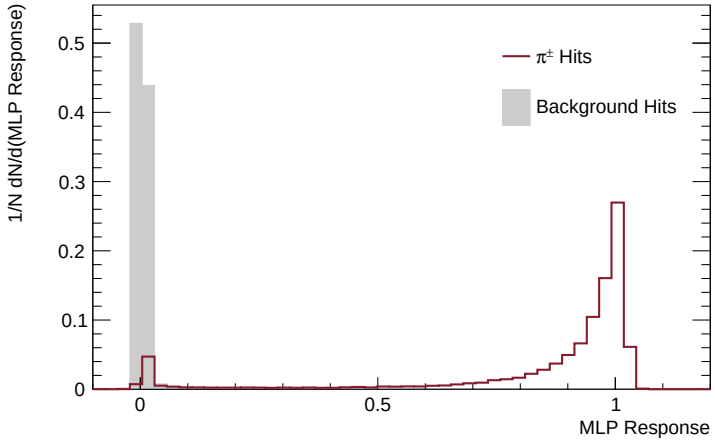

(b)

Figure A.3: Output distribution of the first stage filters for background (gray) and $\pi^{\pm}$ (red line) hit-reference hit combinations after the first stage filters have been applied with a $\pi^{\pm}$ hit efficiency of 90 %. The values are obtained from data of a simulation of 5000 $\Upsilon(4S)$ events fed to the networks. ***(a)*** Layer 1 and ***(b)*** layer 2.

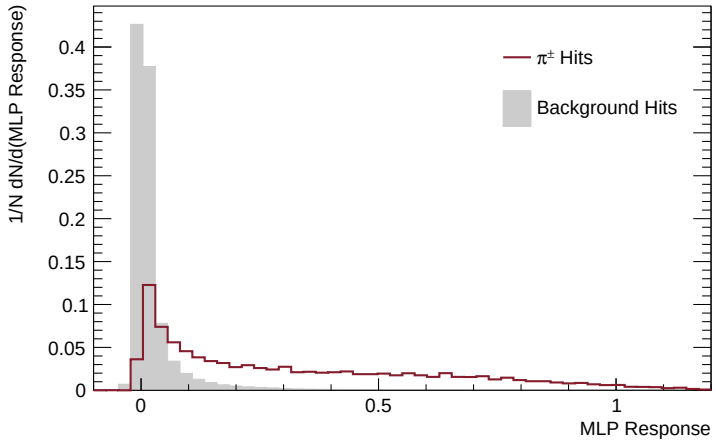

(c)

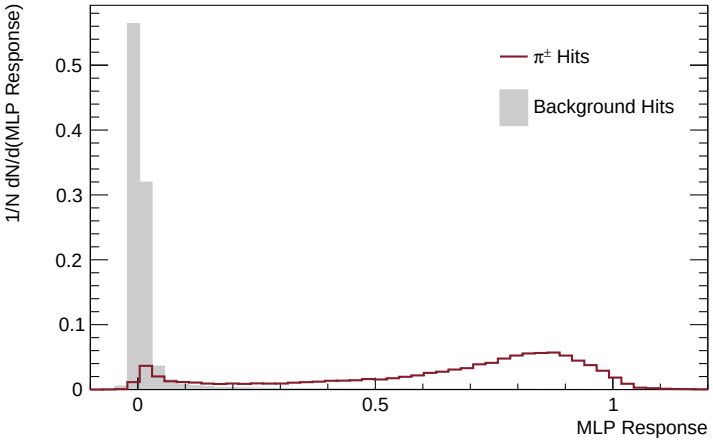

(d)

Figure A.3: Continued. ***(c)*** Layer 3 and ***(d)*** layer 4.

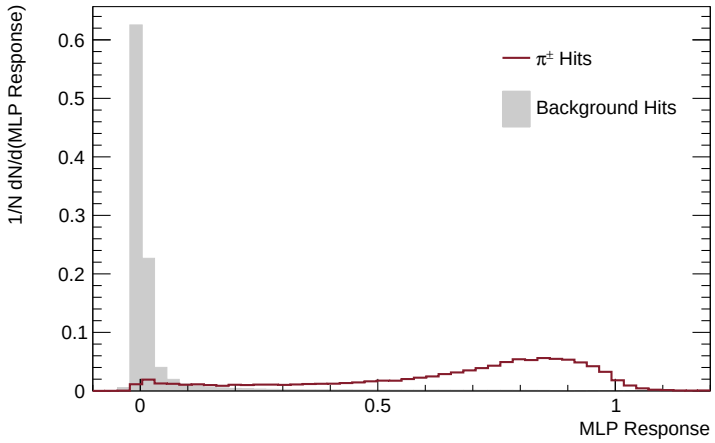

(e)

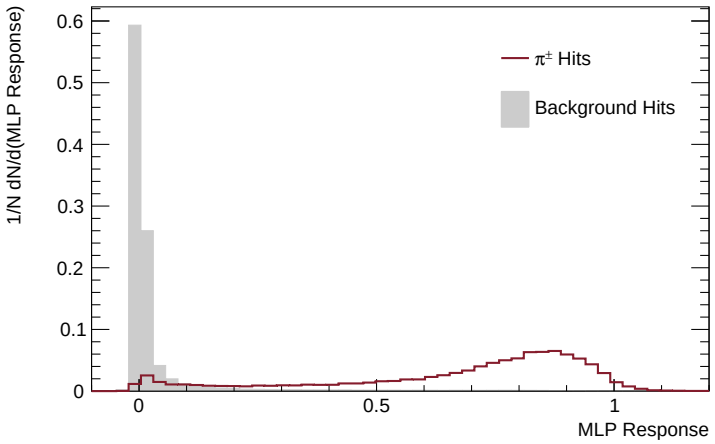

(f)

Figure A.3: Concluded. *(e)* Layer 5 and *(f)* layer 6.

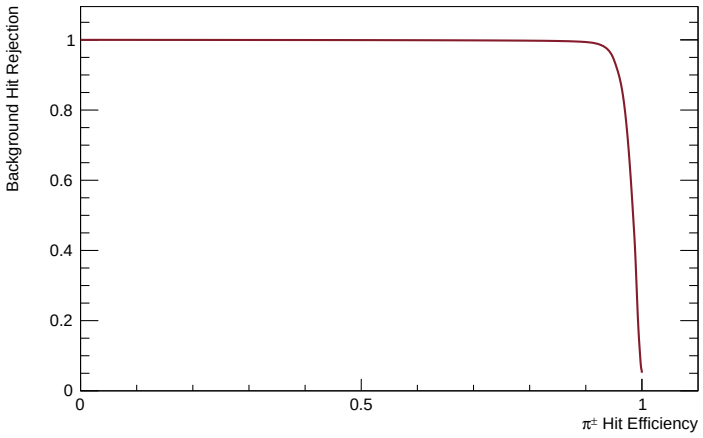

(a)

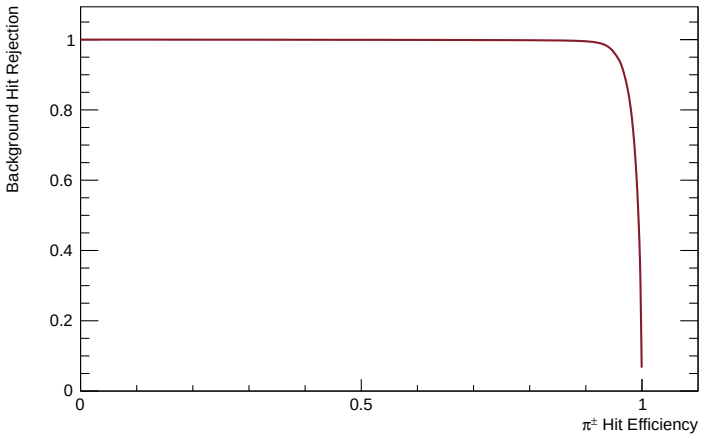

(b)

Figure A.4: Background rejection versus $\pi^{\pm}$ hit efficiency of the second stage filters. The values are obtained from data of a simulation of 5000 $\Upsilon(4S)$ events fed to the networks. ***(a)*** Layer 1 and ***(b)*** layer 2.

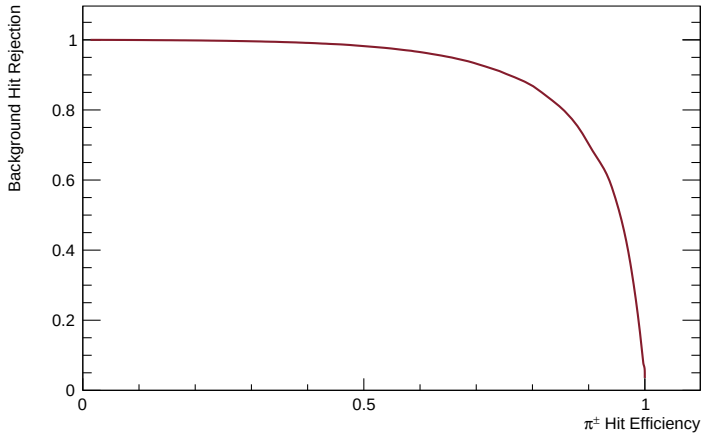

(c)

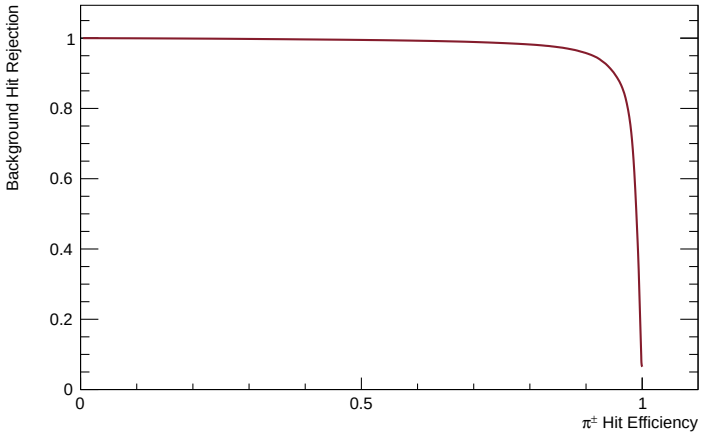

(d)

Figure A.4: Continued. ***(c)*** Layer 3 and ***(d)*** layer 4.

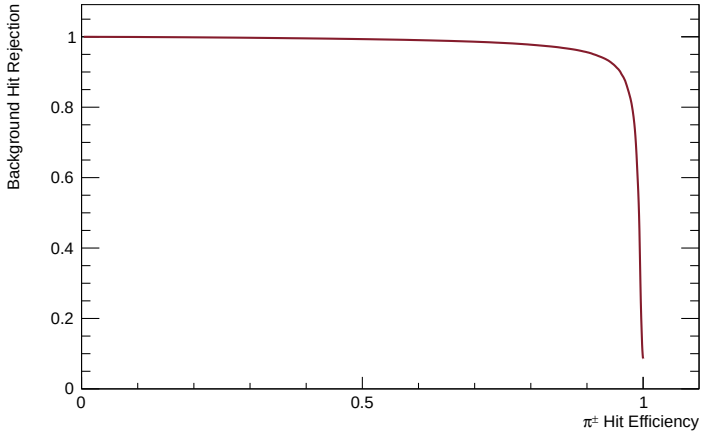

(e)

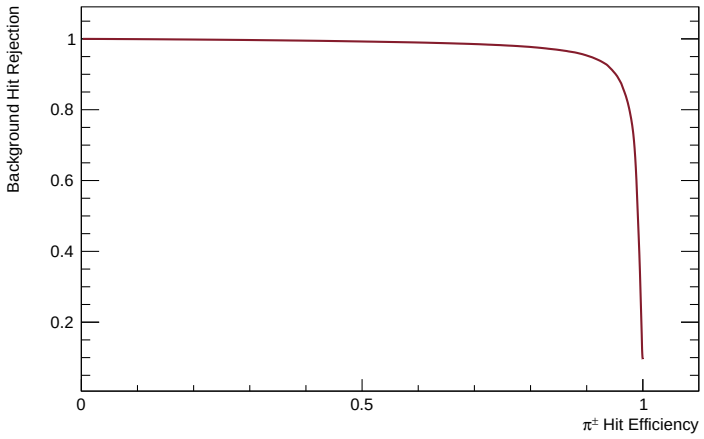

(f)

Figure A.4: Concluded. ***(e)*** Layer 5 and ***(f)*** layer 6.

BIBLIOGRAPHY

[1] A. D. Sakharov, Pisma Zh. Eksp. Teor. Fiz. **5**, 32 (1967), [Usp. Fiz. Nauk161,61(1991)].

[2] A. Abashian *et al.*, Nuclear Instruments and Methods in Physics Research Section A: Accelerators, Spectrometers, Detectors and Associated Equipment **479**, 117 (2002), detectors for Asymmetric B-factories.

[3] T. Abe *et al.*, "Belle II Technical Design Report," (2010), arXiv:1011.0352 .

[4] T. Geßler *et al.*, Nuclear Science, IEEE Transactions on **62**, 1149 (2015).

[5] D. Münchow, *Development of the Online Data Reduction System and Feasibility Studies of 6-Layer Tracking for the Belle II Pixel Detector*, Ph.D. thesis, JLU Giessen (2015).

[6] K. Olive *et al.* (Particle Data Group), Chinese Physics C **38**, 090001 (2014).

[7] J. H. Christenson *et al.*, Phys. Rev. Lett. **13**, 138 (1964).

[8] K. Abe *et al.* (Belle), Phys. Rev. **D66**, 032007 (2002), arXiv:hep-ex/0202027 [hep-ex] .

[9] A. Einstein, Annalen der Physik **354**, 769 (1916).

[10] U. Mosel, *Fields, Symmetries, and Quarks*, 2nd ed., Theoretical and Mathematical Physics (Springer-Verlag Berlin Heidelberg, 1999) originally published by McGraw Hill.

[11] W. Demtröder, *Experimentalphysik 4*, 3rd ed. (Springer-Verlag Berlin Heidelberg, 2010).

[12] D. Perkins, *Introduction to High Energy Physics*, Addison-Wesley student edition (Addison-Wesley Publishing Company, 1987).

[13] M. E. Peskin and D. V. Schroeder, *An Introduction To Quantum Field Theory (Frontiers in Physics)* (Westview Press, 1995).

[14] R. Aaij *et al.* (LHCb), (2015), arXiv:1507.03414 [hep-ex] .

[15] M. Kobayashi and T. Maskawa, Progress of Theoretical Physics **49**, 652 (1973), http://ptp.oxfordjournals.org/content/49/2/652.full.pdf+html .

[16] G. Aad *et al.*, Physics Letters B **716**, 1 (2012).

[17] S. Chatrchyan *et al.*, Physics Letters B **716**, 30 (2012).

[18] B. Aubert *et al.*, Nuclear Instruments and Methods in Physics Research Section A: Accelerators, Spectrometers, Detectors and Associated Equipment **479**, 1 (2002), detectors for Asymmetric B-factories.

[19] S. Hashimoto *et al.*, *Letter of intent for KEK Super* B *Factory*, Tech. Rep. (KEK, 2004).

[20] D. Besson and T. Skwarnicki, Ann. Rev. Nucl. Part. Sci. **43**, 333 (1993).

[21] Y. Grossman and M. P. Worah, Physics Letters B **395**, 241 (1997).

[22] D. Atwood, M. Gronau, and A. Soni, Phys. Rev. Lett. **79**, 185 (1997).

[23] B. Grinstein *et al.*, Phys. Rev. D **71**, 011504 (2005).

[24] I. Adachi *et al.* (Belle), in *Proceedings, 34th International Conference on High Energy Physics (ICHEP 2008)* (2008) arXiv:0809.3834 [hep-ex] .

[25] S. W. Lin *et al.* (Belle), Nature **452**, 332 (2008).

[26] A. Ali and A. S. Safir, Eur. Phys. J. **C25**, 583 (2002), arXiv:hep-ph/0205254 [hep-ph] .

[27] W. Altmannshofer *et al.*, Journal of High Energy Physics **2009**, 019 (2009).

[28] V. Khachatryan *et al.* (LHCb, CMS), Nature **522**, 68 (2015), arXiv:1411.4413 [hep-ex] .

[29] A. G. Akeroyd *et al.* (SuperKEKB Physics Working Group), (2004), arXiv:hep-ex/0406071 [hep-ex] .

[30] R. Antunes-Nobrega *et al.* (LHCb Collaboration), *LHCb reoptimized detector design and performance: Technical Design Report*, Technical Design Report LHCb (CERN, Geneva, 2003).

[31] L. Wolfenstein, Phys. Rev. Lett. **51**, 1945 (1983).

[32] J. Charles *et al.* (CKMfitter Group), Phys. Rev. D **91**, 073007 (2015).

[33] K. Abe *et al.* (Belle Collaboration), Phys. Rev. D **68**, 012001 (2003).

[34] K. Abe *et al.* (Belle), in *3rd Conference on Flavor Physics and CP Violation (FPCP 2004) Daegu, Korea, October 4-9, 2004* (2004) arXiv:hep-ex/0411049 [hep-ex] .

[35] L. Liu *et al.* (Hadron Spectrum), JHEP **07**, 126 (2012), arXiv:1204.5425 [hep-ph] .

[36] S. Fleming, I. Z. Rothstein, and A. K. Leibovich, Phys. Rev. **D64**, 036002 (2001), arXiv:hep-ph/0012062 [hep-ph] .

[37] E. Eichten, K. Gottfried, T. Kinoshita, K. D. Lane, and T. M. Yan, Phys. Rev. D **17**, 3090 (1978).

[38] T. Barnes, S. Godfrey, and E. S. Swanson, Phys. Rev. **D72**, 054026 (2005), arXiv:hep-ph/0505002 [hep-ph] .

[39] (2015), arXiv:1506.06018 [hep-ex] .

[40] R. Aaij *et al.* (LHCb Collaboration), Phys. Rev. Lett. **112**, 222002 (2014).

[41] M. Ablikim *et al.* (BESIII Collaboration), Phys. Rev. Lett. **111**, 242001 (2013).

[42] M. Ablikim *et al.* (BESIII Collaboration), Phys. Rev. Lett. **113**, 212002 (2014).

[43] K. Chilikin *et al.* (Belle Collaboration), Phys. Rev. D **90**, 112009 (2014).

[44] S.-K. Choi *et al.* (Belle Collaboration), Phys. Rev. Lett. **91**, 262001 (2003).

[45] S.-K. Choi *et al.* (Belle Collaboration), Phys. Rev. Lett. **100**, 142001 (2008).

[46] M. Ablikim *et al.* (BESIII Collaboration), Phys. Rev. Lett. **110**, 252001 (2013).

[47] Z. Q. Liu *et al.* (Belle Collaboration), Phys. Rev. Lett. **110**, 252002 (2013).

[48] L. Maiani *et al.*, Phys. Rev. D **89**, 114010 (2014).

[49] Q. Wang, C. Hanhart, and Q. Zhao, Phys. Rev. Lett. **111**, 132003 (2013).

[50] F. Close and S. Godfrey, Physics Letters B **574**, 210 (2003).

[51] S. Dubynskiy and M. Voloshin, Physics Letters B **666**, 344 (2008).

[52] E. S. Swanson, Phys. Rev. D **91**, 034009 (2015).

[53] T. Wei-Zhao *et al.*, Chin.Phys. **C37**, 083101 (2013), arXiv:1308.0960 [hep-ph] .

[54] A. Bondar *et al.* (Belle Collaboration), Phys. Rev. Lett. **108**, 122001 (2012).

[55] A. Bevan *et al.*, The European Physical Journal C **74**, 3026 (2014), 10.1140/epjc/s10052-014-3026-9.

[56] Nobelprize.org, "The nobel prize in physics 2008," `http://www.nobelprize.org/nobel_prizes/physics/laureates/2008/`.

[57] Y. Ushiroda *et al.* (Belle Collaboration), Phys. Rev. Lett. **94**, 231601 (2005).

[58] J.-T. Wei *et al.* (Belle Collaboration), Phys. Rev. Lett. **103**, 171801 (2009).

[59] "MachineParameters150410," (2013), available at http://www-superkekb.kek.jp/documents/MachineParameters150410.pdf, accessed 2015-07-08.

[60] "BelleIIsmall," (2011), available at http://belle2.kek.jp/images/BelleII3D.pdf, accessed 2015-06-23.

[61] "BelleII3D+2people," (2011), available at http://belle2.kek.jp/images/BelleII3D+2people.pdf, accessed 2015-06-23.

[62] C. Marinas, Nuclear Instruments and Methods in Physics Research Section A: Accelerators, Spectrometers, Detectors and Associated Equipment **731**, 31 (2013), {PIXEL} 2012.

[63] (2012), available at http://twiki.hll.mpg.de/bin/view/depfetinternal/webhome, accessed 2014-12-10.

[64] J. Schieck, Nuclear Instruments and Methods in Physics Research Section A: Accelerators, Spectrometers, Detectors and Associated Equipment **732**, 160 (2013), vienna Conference on Instrumentation 2013.

[65] P. Kodyš, Nuclear Instruments and Methods in Physics Research Section A: Accelerators, Spectrometers, Detectors and Associated Equipment **718**, 327 (2013), proceedings of the 12th Pisa Meeting on Advanced DetectorsLa Biodola, Isola d'Elba, Italy, May 20 – 26, 2012.

[66] J. Kemmer and G. Lutz, Nuclear Instruments and Methods in Physics Research Section A: Accelerators, Spectrometers, Detectors and Associated Equipment **253**, 365 (1987).

[67] O. Alonso *et al.*, Nuclear Science, IEEE Transactions on **60**, 1457 (2013).

[68] M. Friedl *et al.*, Nuclear Instruments and Methods in Physics Research Section A: Accelerators, Spectrometers, Detectors and Associated Equipment **732**, 83 (2013), vienna Conference on Instrumentation 2013.

[69] Y. Onuki, Nuclear Instruments and Methods in Physics Research Section A: Accelerators, Spectrometers, Detectors and

Associated Equipment **765**, 99 (2014), hSTD-9 2013 - Proceedings of the 9th International "Hiroshima" Symposium on Development and Application of Semiconductor Tracking DetectorsInternational Conference Center, Hiroshima, Japan, 2 - 5 September 2013.

[70] M. French *et al.*, Nuclear Instruments and Methods in Physics Research Section A: Accelerators, Spectrometers, Detectors and Associated Equipment **466**, 359 (2001), 4th Int. Symp. on Development and Application of Semiconductor Tracking Detectors.

[71] C. Irmler *et al.*, Nuclear Instruments and Methods in Physics Research Section A: Accelerators, Spectrometers, Detectors and Associated Equipment **732**, 109 (2013), vienna Conference on Instrumentation 2013.

[72] M. Friedl, "rev0_half_rendering," (2012), available at `http://gallery.hephy.at/v/electronics/mechanics/Renderings/rev0_half_rendering.png.html`, accessed 2015-08-04.

[73] K. Inami (Belle II PID group), Nuclear Instruments and Methods in Physics Research Section A: Accelerators, Spectrometers, Detectors and Associated Equipment **766**, 5 (2014), {RICH2013} Proceedings of the Eighth International Workshop on Ring Imaging Cherenkov Detectors Shonan, Kanagawa, Japan, December 2-6, 2013.

[74] S. Hirose *et al.*, Nuclear Instruments and Methods in Physics Research Section A: Accelerators, Spectrometers, Detectors and Associated Equipment **787**, 293 (2015), new Developments in Photodetection {NDIP14}.

[75] S. Nishida *et al.*, Nuclear Instruments and Methods in Physics Research Section A: Accelerators, Spectrometers, Detectors and Associated Equipment **766**, 28 (2014), {RICH2013} Proceedings of the Eighth International Workshop on Ring Imaging Cherenkov Detectors Shonan, Kanagawa, Japan, December 2-6, 2013.

[76] M. Tabata *et al.*, Nuclear Instruments and Methods in Physics Research Section A: Accelerators, Spectrometers, Detectors and Associated Equipment **766**, 212 (2014), {RICH2013} Proceedings of the Eighth International Workshop on Ring Imaging Cherenkov Detectors Shonan, Kanagawa, Japan, December 2-6, 2013.

[77] S. Nishida *et al.*, Nuclear Instruments and Methods in Physics Research Section A: Accelerators, Spectrometers, Detectors and Associated Equipment **787**, 59 (2015), new Developments in Photodetection {NDIP14}.

[78] Y. Makida *et al.*, *Advances in cryogenic engineering. Proceedings, Conference, Portland, USA, July 28-August 1, 1997. Pt. A, B*, Adv. Cryog. Eng. **43A**, 221 (1998).

[79] T. Aushev *et al.*, Nuclear Instruments and Methods in Physics Research Section A: Accelerators, Spectrometers, Detectors and Associated Equipment **789**, 134 (2015).

[80] Y. Suetsugu *et al.*, Journal of Vacuum Science Technology A **30**, 031602 (2012).

[81] C. Bernardini *et al.*, Phys. Rev. Lett. **10**, 407 (1963).

[82] S. Neuhaus *et al.*, *Proceedings, 16th International workshop on Advanced Computing and Analysis Techniques in physics (ACAT 14)*, J. Phys. Conf. Ser. **608**, 012052 (2015), arXiv:1410.1395 [physics.ins-det] .

[83] D. Münchow *et al.*, Journal of Instrumentation **9**, C08009 (2014).

[84] R. Itoh *et al.*, Nuclear Science, IEEE Transactions on **60**, 3720 (2013).

[85] A. Moll, Journal of Physics: Conference Series **331**, 032024 (2011).

[86] R. Brun and F. Rademakers, in *AIHENP'96 Workshop, Lausane*, Vol. 389 (1996) pp. 81–86, see also `http://root.cern.ch/`.

[87] R. Sternheimer, M. Berger, and S. Seltzer, Atomic Data and Nuclear Data Tables **30**, 261 (1984).

[88] H. Bethe, Annalen der Physik **397**, 325 (1930).

[89] H. Bichsel, Rev. Mod. Phys. **60**, 663 (1988).

[90] H. A. Bethe, Phys. Rev. **89**, 1256 (1953).

[91] V. L. Highland, Nuclear Instruments and Methods **129**, 497 (1975).

[92] G. R. Lynch and O. I. Dahl, Nucl. Instrum. Meth. **B58**, 6 (1991).

[93] R. Frühwirth and M. Regler, *Data Analysis Techniques for High-Energy Physics*, Cambridge Monographs on Particle Physics, Nuclear Physics and Cosmology (Cambridge University Press, 2000).

[94] P. V. C. Hough, in *Proceedings, 2nd International Conference on High-Energy Accelerators and Instrumentation, HEACC 1959*, Vol. C590914 (1959) pp. 554–558.

[95] R. O. Duda and P. E. Hart, Commun. ACM **15**, 11 (1972).

[96] H. Li, M. A. Lavin, and R. J. L. Master, Computer Vision, Graphics, and Image Processing **36**, 139 (1986).

[97] K. Königsberger, *Analysis 2*, Springer-Lehrbuch (Physica-Verlag, 2006).

[98] S. Wolfram, *Cellular Automata and Complexity: Collected Papers*, 1-2150-A; Louisiana Barrier Island (Addison-Wesley Publishing Company, 1994).

[99] J. Lettenbichler *et al.*, Journal of Physics: Conference Series **396**, 022030 (2012).

[100] R. Frühwirth *et al.*, Nuclear Instruments and Methods in Physics Research Section A: Accelerators, Spectrometers, Detectors and Associated Equipment **732**, 95 (2013), Vienna Conference on Instrumentation 2013.

[101] R. E. Kalman, Transactions of the ASME–Journal of Basic Engineering **82**, 35 (1960).

[102] J. Neyman and E. S. Pearson, Philosophical Transactions of the Royal Society of London A: Mathematical, Physical and Engineering Sciences **231**, 289 (1933).

[103] C. Bishop, *Pattern Recognition and Machine Learning*, Information Science and Statistics (Springer, 2006).

[104] A. Hoecker *et al.*, PoS **ACAT**, 040 (2007), arXiv:physics/0703039 .

[105] J. J. Hopfield, Proceedings of the National Academy of Sciences **79**, 2554 (1982).

[106] R. Frühwirth, Computer Physics Communications **78**, 23 (1993).

[107] T. Alexopoulos *et al.*, Nuclear Instruments and Methods in Physics Research Section A: Accelerators, Spectrometers, Detectors and Associated Equipment **592**, 456 (2008).

[108] B. Kronenbitter, *Measurement of the branching fraction of* $B^+ \to \tau^+ \nu_\tau$ *decays at the Belle experiment*, PHD Thesis, KIT (2014).

[109] O. Frost, *A Local Tracking Algorithm for the Central Drift Chamber of Belle II*, Diploma Thesis, KIT (2013).

[110] O. Lutz, *Search for* $B \to h^{(*)} \nu \overline{\nu}$ *decays at Belle and development of track finding for Belle II*, PHD Thesis, KIT (2012).

[111] T. Schlüter (Belle-II Software Group), *Proceedings, 23rd International Workshop on Vertex Detectors (Vertex 2014)*, PoS **Vertex2014**, 039 (2014), arXiv:1411.3485 [physics.ins-det] .

[112] M. Schnell, *Development of an FPGA-based Data Reduction System for the Belle II DEPFET Pixel Detector*, Ph.D. thesis, University Bonn (2015).

[113] M. Schnell (DEPFET), *Proceedings, 23rd International Workshop on Vertex Detectors (Vertex 2014)*, PoS **Vertex2014**, 016 (2015).

[114] C. Höppner *et al.*, Nuclear Instruments and Methods in Physics Research Section A: Accelerators, Spectrometers, Detectors and Associated Equipment **620**, 518 (2010).

[115] J. Rauch and T. Schlüter, *Proceedings, 16th International workshop on Advanced Computing and Analysis Techniques in physics (ACAT 14)*, J. Phys. Conf. Ser. **608**, 012042 (2015), arXiv:1410.3698 [physics.ins-det] .

[116] R. Frühwirth and A. Strandlie, Computer Physics Communications **120**, 197 (1999).

[117] M. Nadler and R. Frühwirth, Journal of Physics: Conference Series **396**, 022037 (2012).

[118] C. Kleinwort, Nuclear Instruments and Methods in Physics Research Section A: Accelerators, Spectrometers, Detectors and Associated Equipment **673**, 107 (2012).

[119] M. Heck, (2015), personal communication.

[120] D. J. Lange, *Proceedings, 7th International Conference on B physics at hadron machines (BEAUTY 2000)*, Nucl. Instrum. Meth. **A462**, 152 (2001).

[121] S. Agostinelli *et al.* (GEANT4), Nucl. Instrum. Meth. **A506**, 250 (2003).